HEAT TRANSFER AND FLOW CHARACTERISTICS OF SONIC NOZZLE

by

GANAPATHI REDDY MADAMADAKALA

B.E, Osmania University, 2008

A THESIS

Submitted in partial fulfillment of the requirements for the degree

MASTER OF SCIENCE

Department of Mechanical and Nuclear Engineering
College of Engineering

KANSAS STATE UNIVERSITY
Manhattan, Kansas

2013

Approved by:

Major Professor
Dr. Steven Eckels

Abstract

The current research presents the experimental investigation of heat transfer and flow characteristics of sonic multiphase flow in a converging-diverging nozzle. R134a and R123 are used in this study. Four different nozzle assemblies with two different throat sizes (2.43mm and 1.5 mm with 1° growth angle with the center line of the nozzle in the diverging section) and two different heater lengths (200mm and 125mm) were tested. Each test section was an assembly of aluminum nozzle sections. The experimental facility design allowed controlling three variables: throat velocity, inlet temperature, back pressure saturation temperature.

The analysis used to find the average heat transfer of the fluid to each nozzle section. This was achieved by measuring the nozzle wall temperature and fluid pressure in a steady state condition. Two methods for finding the average heat flux in sonic nozzle were included in the data analysis: infinite contact resistance and zero contact resistance between nozzle sections.

The input variables ranges were 25 °C and 30 °C for inlet temperature and back pressure saturation temperatures, 1100-60,000 kg/m ^{2} s for mass flux, and 1.4-700 kW/m^2 heat flux. The effect of the mass flux and heat flux on the average two-phase heat transfer coefficients was investigated. The flow quality, Mach number(M), and Nusselt number ratio (φ) were also calculated for each section of the nozzle.

As the fluid flowed through the nozzle, the pressure of the liquid dropped below the inlet saturation pressure of the liquid due to sonic expansion in the nozzle. This temperature drop was significantly lower in the case of R134a than R123. The results showed that the two-phase heat transfer coefficients were above of 30000 W/m^2 K in the first 75 mm of the nozzle, and they decreased along the nozzle. The Mach number profile appeared similar to the temperature profile, and the fluid was in the sonic region as long as temperature of the fluid dropped in the

nozzle. Nusselt number ratios were compared with the Mach numbers and showed that the Nusselt number ratio were increased in the sonic region. The results showed that the length of the sonic region was larger for R123 than for R134a, and the Mach numbers were higher for R123. The Nusselt ratios of R123 were low compared to the R134a cases, and the trend in the Nusselt ratios was notably different as well.

Table of Contents

List of Figures

List of Tables

Nomenclature

A_{cs} = Cross sectional area

A_s = Wet surface of the fluid in the nozzle

A_g = Area of the vapor phase

A_l = Area of the liquid phase

A_e = Area of cross section of the nozzle at the exit of the control volume

A =Area of the two-phase mixture

c = Speed of sound

c_l = Speed of sound in liquid phase

c_g = Speed of sound in vapor phase

D_{avg} = Average diameter of the nozzle section

G = Mass flux

g = Acceleration due to gravity

h = Heat transfer coefficient

h_c =Average heat transfer coefficients in solid model

h_I = Average heat transfer coefficients in insulated model

h_i = Enthalpy of the fluid entering the control volume

h_e = Enthalpy of the fluid leaving the control volume

h_{fg} = Latent heat of vaporization

h_f = Enthalpy of the liquid phase

k_l = Thermal conductivity of the liquid

M = Mach number

Nu_{tp} = Nusselt number in two-phase

Nu_l = Nusselt number in liquid

p_1 = Pressure in the converging section

p_2 = Pressure at the throat of the nozzle

Pr_l = Prandtl number of the liquid

q_c = Average heat flux in the solid model

q_I = Average heat flux in the insulated model

$\dot{q}$ = Heat flux

$\dot{Q}$ = Net rate of heat in the control volume

Re_l = Reynolds number of the liquid

T_W = Wall temperature

T_{fluid} = Fluid temperature

T_i = Fluid temperature entering the control volume

T_e = Fluid temperature leaving the control volume

u_g = Superficial velocity of the vapor phase

u_l = Superficial velocity of the liquid phase

v_1 =Velocity in the converging section

v_2 = Velocity at the throat

v_i = Velocity of the fluid entering the control volume

v_e = Velocity of the fluid leaving the control volume

$\dot{W}$ = Net rate of work in the control volume

x = Flow quality

z_1 = Height of the fluid in the converging section

z_2 = Height of the fluid at the throat

ρ_1 =Density in the converging section

Φ = Nusselt number ratio

ρ_g = Density of the vapor

ρ_l = density of the liquid

υ_l = Specific volume of the liquid phase

υ_g = Specific volume of the vapor phase

α =Void fraction

μ_l =Coefficient of the viscosity

Cp_l =Specific heat at constant pressure

ρ_2 = Density at the throat

$\dot{V}$ =Volumetric flow of the two-phase fluid

$\dot{V}_l$ =Volumetric flow of the liquid phase

$\dot{V}_g$ =Volumetric flow of the vapor phase

1 Introduction

1.1 Back ground

Cavitation is a well-known phenomenon that occurs in many internal flow devices, such as pumps, valves, heat exchangers, and propellers. In nearly every case, this phenomenon is undesirable, creating turbulence and energy loss, and more seriously, collapsing bubbles created by cavitation can cause severe damage to the internal surfaces of the device.

However, while the effects of cavitation are typically destructive, in certain cases, cavitation can be used to generate something useful. In the current research, cavitation is used to produce a multiphase region that generates an efficient cooling effect. This multiphase region is generated in a converging–diverging nozzle—a nozzle that initially constricts down to a minimum area (called the throat) and then expands. Fluid moving through a converging-diverging nozzle at sonic or supersonic velocities (which, for multi-phase flow, are actually not that high in velocity) actually accelerates through the diverging section of the nozzle. The large pressure drop induced by the acceleration causes cavitation to occur in the flow. This cavitation causes a useful cooling effect.

Since very few studies have analyzed the thermodynamic performance of sonic two-phase flow through such a nozzle, it is very important to further test this idea because it may be found that the effect is useful. This cooling effect, because of its mechanical simplicity (only requiring one component), if better understood, may have many potential applications in HVAC (i.e. heating, ventilating and air conditioning), electronic cooling or automobile industries.

The current document presents the results from an experimental investigation of the sonic multiphase region in the diverging section of nozzles with R134a and R123 as the working fluid. Studying the sonic region involves a number of phenomena such as bubble dynamics,

homogeneous nucleation, two-phase boiling, and flow patterns, but this document does not describe the flow patterns or bubble dynamics. Rather this document concentrates on two-phase boiling heat transfer phenomena in the sonic flow region of nozzles.

Flow boiling in two-phase flows is always a complex engineering problem; direct analytical study is very difficult. Thus such phenomenon is often studied by experimental investigation. Experimentally studying flow boiling involves measuring and correlating the relationship between different parameters such as nozzle geometry, fluid properties, heat flux, and mass flux etc. This research is on the forefront of experimental analysis for sonic multi-phase flow nozzles, very little other work directly related to this topic can be found in the literature. In the literature review section, however, some studies related to flow boiling and sonic flow models are discussed because they provide supporting information.

1.2 Significance of research

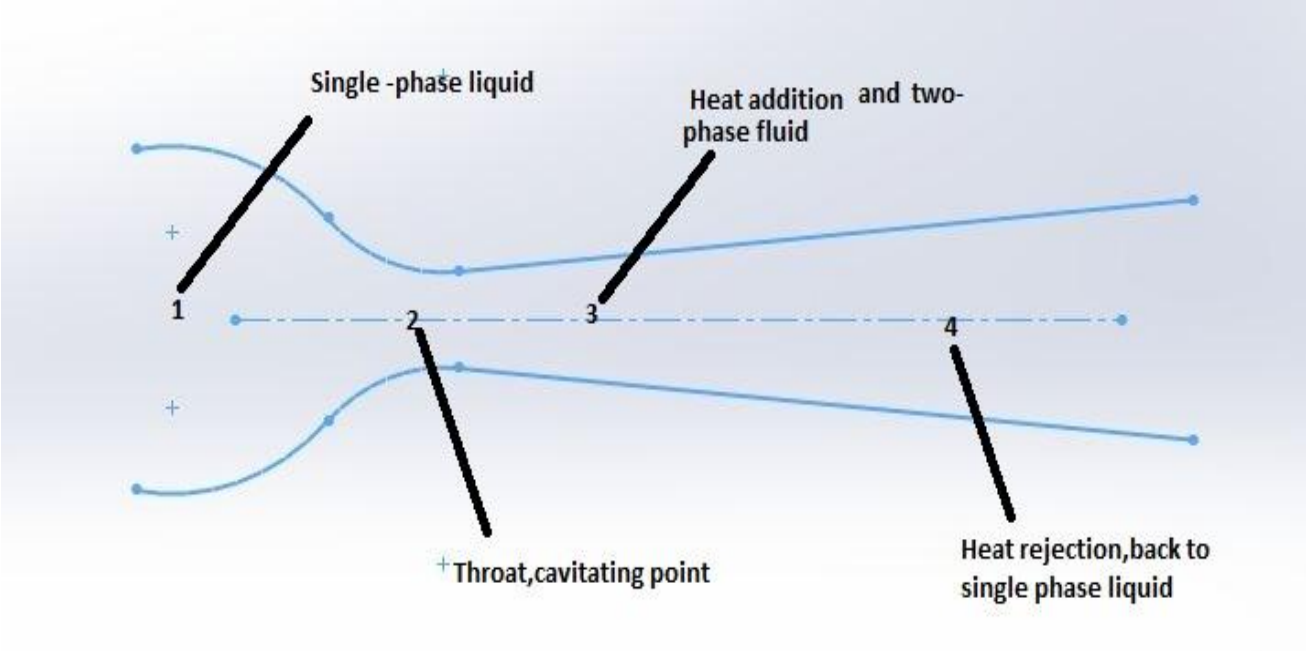

Figure 1.1 Two-phase flow process in the nozzle

Figure 1.1 shows a simple converging-diverging nozzle. Initially, the nozzle has a single phase subcooled liquid entering the upstream section. The flow accelerates towards the throat and the pressure drops due to increased kinetic energy. For certain conditions the pressure at the minimum area may be low enough to cause cavitation in the flow. Sonic flow conditions can be achieved in many situations causing the flow to continue to accelerate down the expanding section of the nozzle. The continued acceleration causes the pressure to decrease causing more liquid to flash into vapor-cooling mixture and causing a measureable decrease in both temperature and pressure. As the energy of the flow is used, the Mach number reduces and approaches one and a condensation shock may appear causing the fluid to return to a single phase liquid.

Consider a small element of fluid travelling through the nozzle. The behavior of the element in the ideal case can be explained by Bernoulli's equation as shown in Equation 1.1. Bernoulli's equation is only a good approximation from region 1 to 2 as shown in Figure **1.1**.

$$\frac{p_1}{\rho_1} + \frac{1}{2} v_1^2 + gZ_1 = \frac{p_2}{\rho_2} + \frac{1}{2} v_2^2 + gZ_2 \tag{1.1}$$

Initially, at 1, the element is in a liquid phase and possesses more pressure energy than kinetic energy. As the element passes the throat (2) of the nozzle, the pressure energy drops due to increasing kinetic energy. As the pressure drops, it falls below the saturation pressure of the liquid (similar to the effect of an expansion valve on a refrigeration cycle), forcing small bubbles to form in the element. As the flow passes through the throat, the sonic effect causes the saturation pressure to drop and increase the size of the vapor bubbles, extracting heat from the surrounding fluid (3). As the element moves further down the nozzle, the bubbles continue to grow and the temperature of the surrounding fluid continues to drop. Eventually, the sonic effect can no longer continue and the vapor shocks back to liquid giving off heat to the surrounding

liquid. Thus at the outlet of the nozzle, the element is a single phase liquid similar to the inlet conditions. This effect is similar to the function of the evaporator and the compressor in the refrigeration cycle. In the sonic region, there are very high heat transfer coefficients (significantly higher than single phase heat transfer) between the fluid and the nozzle wall. A full description of this phenomenon is largely lacking in the literature but is critical to mature this technology for use in advanced cooling applications. This study significantly contributes to the full characterization of the sonic multi-phase flow phenomena.

1.3 Objective

This research investigates the heat transfer and flow characteristics of sonic multiphase flow, thus providing an experimental database of two-phase heat transfer coefficients in the diverging section of a converging-diverging nozzle. The flow characteristics include the length of the sonic region and the acceleration characteristics of the flow. The objective also includes determining the effect of geometry, including inlet and fluid passage dimensions, and refrigerant choice (high and low pressures refrigerants) on the heat transfer rates and flow parameters.

1.4 Scope of work

This research mainly focused on experimental work and analysis of the results by calculation of an average two-phase heat transfer coefficient in the nozzle. Experimental work includes the testing of the different throat diameters 1.5 mm and 2.43 mm with 1° growth angle with the center line of the nozzle in the diverging section as shown in Figure 1.2.

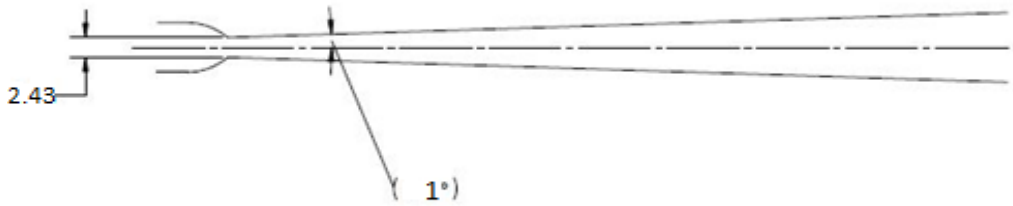

Figure 1.2 Dimensions of the nozzle

Heat transfer coefficients are determined from measured temperatures and heat flux. Heat flux between the fluid and nozzle is the most difficult to determine and is determined from the temperature distributions with a set of assumptions. There are two limiting assumptions that can identified for the nozzle. One is to assume no heat transfer (insulation) between the nozzle sections, in essence this model assume infinite contact resistance between the nozzle sections. The other possible assumption is to assume no contact resistance between the nozzle sections thus one can consider that the nozzle is a solid piece (solid model). The heat flux distribution (and there by heat transfer coefficients) for the solid model can be found by simulating the nozzle using the finite element method. Specifically, a 3D conduction model was implemented in Solid Works (2012).

Heat transfer coefficients can be found using both set of assumptions outlined above. These two assumptions provide bounds on the actual heat transfer coefficients in the current system, so the real heat transfer coefficients of the fluid fall somewhere in between the two models. However, it was found that calculating the heat transfer coefficients by both methods

gave similar results, thus either model yields a good approximation of the true heat transfer coefficient.

The scope of the thesis includes the comparison between the insulated model heat transfer coefficients and solid model heat transfer coefficients and using the differences to define uncertainties. This document also shows the calculation of the two-phase thermodynamic properties and sonic properties in the system and the effect of these properties on the heat transfer coefficients.

A test input matrix was developed for each nozzle and experiments were conducted based on the matrix. The control variables in the input matrix are inlet temperature, throat velocity, back pressure, saturation temperature, and heater power. All the experiments were performed under steady state conditions. The operating conditions are, adiabatic (unheated) and diabetic (heated) methods. Moreover, in all tests the nozzle was insulated from the environment.

Table 1.1 Input matrix

Velocity	20-50m/s
Heater power	80-1200 watts
Inlet temperature	25 and 30 C
Back pressure	Inlet saturation pressure
Inlet pressure	1000-2700 kPa

1.5 Document Organization

This document is divided in seven chapters and one appendix (data tables). The current chapter is the research introduction. The second chapter presents the literature review of sonic velocity and flow boiling. Chapter three presents the experimental facility's test section,

refrigerant and water loops, and instruments. Chapter 4 presents the data analysis, including determination of average heat flux and heat transfer coefficients for each section of the nozzle, and uncertainty analysis.

Chapter 5 and 6 presents the research results. Each chapter presents the results of four different test sections. Specifically Chapter 5 is the experimental results, which are directly measured from instruments. Chapter 6 presents flow parameters along the nozzle and its effect on heat transfer coefficients for R134a and R123. Chapter 7 presents the conclusions for the research and the appendix present data tables.

2 Literature review

2.1 Introduction

The focus of the current study is on sonic multiphase flow nozzles. In these devices, the refrigerant enters as a single phase sub-cooled liquid. Because of the geometry, the liquid expands to form a multiphase region due to the pressure drop; however, after condensation shocks, the refrigerant leaves the device as a single phase liquid. There are several phenomena relevant to the operation of this device. The likely mechanism for phase-change in these devices is homogeneous nucleation. The possible heat transfer mechanisms in sonic nozzles are convective boiling and nucleate boiling. Also, the way that the pressures in the flow change as the fluid moves through the nozzle are described by two-phase sonic flow phenomenon.

This chapter gives a review of the literature related to this research. There are very few studies on the two-phase heat transfer performance of a sonic two-phase nozzle. Substantially more research has been done in areas related to the phenomena occurring in sonic two-phase nozzles, such as homogeneous cavitation, flow boiling in tubes, and pressure waves in nozzles. However, this research typically was limited to specific applications.

The formation of nucleation sites in the bulk of a liquid is called homogeneous nucleation. Experimentally, nucleation sites can be generated within a superheated liquid in the range of the metastable temperature zone. To understand the metastable temperature zone, it is important to study the liquid-vapor phase change phenomena on P-V diagram of water. Consider a pure liquid which is depressurized at a constant temperature. As the pressure of the liquid drops below the saturation pressure, if a sufficient number of nucleation sites are generated in the liquid, then the liquid will become vapor, and the substance will tend to move in a horizontal isothermal line. If there are not a sufficient number of nucleation sites, then the liquid will

continuously drop in pressure and will reach a metastable state. The difference between the actual saturated liquid state and the theoretical metastable state is called the liquid tension. This is the most important property of two–phase flows. The fluid properties, like density and enthalpy, of the saturated liquid are nearly constant, but the density and enthalpy of the vapor differs by at least 2 to 5 times those of the liquid and always change with temperature. This peculiar behavior of the properties in two-phase flows provided some of the motivation for the research in sonic multi-phase flow nozzles.

The fundamental characteristics of the formation of vapor bubbles in the bulk of liquids has been investigated by many people in the past like Volmer and Weber (1926), Zedovich (1943), Frenkel (1955) and Skirpov (1974), Carey (1992). Brennen (1991) has done fantastic work reviewing the mechanisms and properties of bubble nucleation such as homogeneous and heterogeneous nucleation and also thermal effects on bubble growth in sonic nozzles. This homogeneous nucleation requires a sufficient pressure driving force for it to occur. There are many different ways to cause nucleation sites: contaminated gas bubbles in the crevice of solid particles, suspended particles in liquid and cosmic radiation. Each one will have different applications, but this research is trying to produce homogeneous nucleation by only inducing a sufficient pressure force by the geometry of the nozzle and does not use any of these methods as explained above. The following literature review is organized into two separate areas. Those are flow boiling and sonic flow.

2.2 Flow boiling

Flow boiling occurs when a liquid is flowing inside a heated tube by natural circulation or forced circulation and a phase change occurs. The major difference between these two flows (natural circulation and forced circulation) is that one flow is driven by density difference and

one is driven by pressure difference. Similarly these two mechanisms have different range of heat transfer coefficients and different flow patterns of the fluid. Flow boiling is complex due to the presence of the liquid and vapor. Specifically, two-phase flow patterns change with thermodynamic quality, mass flow rate and bulk mixture properties. In order to understand flow boiling in tubes, consider a vertical tube with uniform heat flux along the tube length. Initially, sub-cooled liquid enters the tube, and single-phase heat transfer occurs between the tube and fluid. The heat transfer coefficient varies due to change in the temperature and properties of the fluid in the direction of flow (it only happens if the flow is natural convection. For forced convection the heat transfer coefficients are not dependent on temperature difference or heat flux). Further down the tube, bubbles start to grow as the temperature of the liquid increases above its saturation temperature. This phenomenon is called "onset of nucleate boiling" (ONB). The bubbles form even in the sub-cooled liquid zone due to higher wall temperatures, but these bubbles will quickly condense as they move towards the subcooled liquid core of the tube. As more nucleation sites develop, the contribution of the single phase heat transfer contribution diminishes in the tube. When the surface (tube surface) is fully active for nucleation, more nucleation sites continue to develop until enough nuclei exist to reach fully developed nucleate boiling. At this point, the saturated boiling region is reached where the liquid is at the saturation temperature at the local pressure over the entire cross section of the tube. Evaporation occurs at the core of the tube when local temperature exceeds the saturation temperature. Initially vapor bubbles grow at the wall, and detach to form slugs. This leads to annular flow along the circular tube. In the annular region, the liquid film acts as a good thermal conductor to prevent the liquid from being superheated and to sustain nucleate boiling. In this region, the nucleate boiling effect decreases gradually as convective boiling becomes more important. Ultimately, at some critical

vapor quality complete evaporation of the liquid film occurs. The transition is known as dry-out region. The region between the dry-out point and the transition to dry saturated vapor is called the liquid deficient region. There are other interesting things to discuss such at different flow patterns in flow boiling, but the present research focuses on nucleate boiling and convective boiling. These two processes contribute to the overall heat transfer coefficients in two-phase flows.

A number of different papers have been published for assessing the performance of two-phase flow boiling. Some of them focused on the dimensions of the tubes or channels containing the fluid, the saturation temperatures, and the inlet wall temperatures of the secondary fluids while others focused on heat flux and mass fluxes. Among those who provided the experimental two-phase flow boiling models are Thome (2009), Cavallini (2007), Yu et al. (2002), Ozdemir et al. (2010) and Huo et al. (2003).

This review will only focus on experimental heat transfer coefficients of two-phase flow boiling in small channels. Three variables are significant as part of this research. These are the mass flux, the heat flux, and the quality. In the case of large sized tubes, the nucleate boiling heat transfer coefficient is strongly correlated to the heat flux and mass flux while vapor quality was not a major factor. In the present research, mass fluxes are very high in the range of 1500-50000 kg/m^2s, and thus some interesting phenomena are seen in the two-phase heat transfer coefficients.

Devine et al. (1993) investigated the heat transfer in a stainless steel converging- diverging nozzle. They simulated two different nozzles: one with small convergence and divergence angles, the other one with a greater angle of convergence and divergence. They developed a correlation to find the wall temperature by using the momentum and continuity equation and

energy conservation. They presented a 0.102 C wall temperature drop at the throat with a bubble diffusing coefficient of 17 cm^2/s for the lower angles and a 0.861 C wall temperature drop for a bubble diffusing coefficient of 22 cm^2 /s . Lower bubble diffusion causes the wall cooling to increase; conversely, increasing the bubble diffusion decreases the degree of wall cooling.

Yu et al. (2002) studied the two-phase pressure drop, boiling heat transfer coefficient and critical heat flux of water in a 2.98 mm ID and 0.91 m heated length tube. The operating conditions were mass fluxes in the range of 50-200 kg/m^2 s, inlet temperature at 80 °C, and heat fluxes up to 300 kW/ m^2. They used the Lockhart–Martinelli approach to correlate the two-phase pressure drop. Similarly, the Chen correlation was used to calculate the two-phase heat transfer coefficients in the water. They have presented 50,000 W/m^2 K as the highest heat transfer coefficients at the higher heat flux.

Qwhaib et al. (2003) studied the evaporation in circular micro channels of R134a in vertical tubes with internal diameters of 1.7mm, 1.224 mm heated uniformly over a length of 220 mm. Their operating conditions were heat fluxes over a range of 3-35 kW/m^2 and mass fluxes from 50-400 kg/m^2 s. They conducted experiments under two pressures: 8.26 bar and 6.46 bar. They have presented heat transfer coefficients up to 10 kW/m^2 K at high heat fluxes. They found heat transfer coefficients to be a strong function of pressure and heat flux and to be independent of mass flux and quality. They indicated that the contribution of forced convection heat transfer to overall heat transfer rate was small, and heat transfer was dominated by nucleate boiling.

Huo et al. (2003) studied the boiling heat transfer for R134a in small diameter tubes made from stainless steel and having internal diameters of 2.01 mm and 4.26 mm. The operating variables were heat fluxes in the range of 13-150 kW/m^2, mass fluxes from 50-100 kg/m^2 s, and pressure up to 12 bar. They conclude that nucleate boiling is dominant when the vapor quality is

less than 40% for 4.20 mm and 20% for 2.01 mm tubes. After this range of qualities, the heat transfer coefficients decrease with quality increase. Furthermore, this decrease occurs for the entire range (0 to 90 %) of quality.

Cavallini et al. (2007) studied the measurement of local heat transfer coefficients by experimental procedures inside the circular mini-channel of 0.96 mm ID for R134a. They measured the heat transfer coefficients not by imposing heat flux; instead, the flow boiling process was controlled by the inlet temperature of the secondary fluid (water). They have presented the temperature profile and heat flux profile along the circular channel. They have presented heat transfer coefficients around 20,000-45,000 W/m^2 K in the range of heat fluxes from 30 to 150 kW/m^2. They have conducted similar experiments by varying inlet temperature, mass flux, and vapor quality.

Ozdemir et al (2010) presented a flow boiling study for high mass fluxes in the range of 1000 to 7500 kg/m^2 s; they conducted experiments on a 250 μm tube with deionized water as the working fluid. They reported heat transfer coefficients from 10-60 kW/m^2 K for these mass fluxes. The heat transfer coefficients showed an increase with mass flux.

Ali et al (2011) studied flow boiling characteristics of R134a in a mini channel of internal diameter 1.70 mm and uniformly heated over a length of 220 mm. They conducted experiments for mass fluxes from 50 to 600 kg/m^2 s and saturation temperatures 27 °C and 32 °C. They reported that heat transfer coefficients increase with the imposed heat flux while mass flux and vapor quality does not have any effect on the heat transfer coefficients. They achieved heat transfer coefficients up to 19,000 W/m^2 K at a 156 kW/m^2 heat flux over a range of qualities from 0 to 0.5.

Copetti et al (2011) studied flow boiling heat transfer and pressure drop of R134a in a mini tube with 2.6 mm ID. They showed the results for variations of saturation temperature, mass flux, heat flux and vapor quality. The test variables were saturation temperatures of 12 °C and 22 °C, heat fluxes in the range of 10 to 100 kW/ m^2, and mass fluxes from 240-930 kg/m^2s. They concluded that the heat transfer coefficients have a significant influence of heat flux at low qualities. They presented heat transfer coefficients from 3000-16000 W/m^2 K in their experiments. The influence of mass velocities vanished at high qualities where the heat transfer coefficients also decreased. Additionally, they presented a predictive model for the heat transfer coefficients, and the measured heat transfer coefficients agreed well with the predictive models with an uncertainty of 35%.

2.3 Sonic velocity

Sonic velocity refers to the speed of sound through a substance. In this research, the speed of sound through two-phase (cavitating) fluid is of primary interest. Cavitating flows contain a mixture of incompressible areas (liquid phase) and highly compressible areas. This means that the overall speed of sound in these flows varies by the amount of void in the mixture. For example the speed of sound is 4.3 times faster in water than air. Brennen (1991) shows an expression for sonic velocity in two phase flows by considering the fact that the pressure is a function of density and its associated sonic speed, as shown in *Equation 2.1*

$$c = \left(\frac{\delta p}{\delta \rho} \right)^{\frac{1}{2}} \tag{2.1}$$

Where c is the speed of sound, p is the pressure and ρ is the density.

Brennen developed a two-phase flow homogeneous model by considering an infinitesimal volume of the mixture containing dispersed phase (vapor) and continuous phase (liquid). Equation 2.2 shows the Brennen's equation without considering surface tension effects and the mass exchange between the phases. The present thesis used Brennen's equation to calculate sonic velocity in two-phase flow.

$$c = \left(\frac{1}{\left(\rho_l(1-\alpha) + \rho_g \alpha\right)\left(\frac{1-\alpha}{\rho_l c_l^{\,2}} + \frac{\alpha}{\rho_v c_g^{\,2}}\right)} \right)^{0.5} \qquad 2.2$$

This subsection highlights some of the different sonic velocity models in two-phase flows. Mallock (1910) was the first person who investigated the speed of sound in two-phase flows. He assumed a homogeneous mixture of the same density and elasticity (E), and modeled the two phases as an incompressible liquid and an ideal gas. Wood (1941) extended Mallock efforts by considering the compressibility of the mixture. Wood calculated the speed of sound over a wide range of void fractions (< 0.9) and concluded speed of sound was very low (< 20 m/s) with a void fraction.

Tangren et al. (1949) developed a general thermo-hydrodynamic relation in a converging-diverging nozzle by using the continuity, momentum, and energy equations. They determined the magnitude of the velocity in a pressure pulse through a mixture of gas-water and compared this with the velocity of the flow. Experimental results were then compared with the equation they developed. They developed the speed of sound in mixture by deriving the equation of motion and equation of state.

Karplus (1958) did some experiments concerned with the relationship between the velocity of sound and the void fraction of a two-phase flow. The experimental goal was to measure the wavelength (λ) of the acoustic waves in a vertical test section. Knowing the wavelength and frequency, then allows the speed of sound to be calculated by $c=\lambda*f$. He found that the minimum velocity in a mixture of liquid and air at about 50% of the concentration was approximately 20 m/s.

Brown G.A et al (1964) analytically derived speed of sound in two-phase mixtures by considering the ratio of change in pressure to the change in density. They concluded that constant entropy lines in pressure-density diagram have continuous slope in both single phase and two-phase region with a discontinue slope at a phase interface. For saturated liquid, there is an extremely large change in the slope at phase boundary. The vapor phase has a similar change but only less significant than the liquid on a constant pressure line. A small change in pressure at either extremity of the constant pressure line cause a large change in density. But, since, the change in density in a saturated liquid is higher than the density change in a saturated vapor, sonic velocities are much lower near saturated liquid than near saturated vapor.

Martindale and Smith (1980) investigated sonic speeds in the annular flow regime. They collected data by measuring the time required for shockwaves to travel between two fixed points in a flowing stream. The results showed that, in contrast to the homogenous equilibrium model, the speed of sound in the regions where the gas was considered as a continuous phase was essentially that of the sonic velocity in the gas alone. Thus, the sonic velocity data supported the use of an analytical separated flow model.

2.4 Conclusion

The above mentioned studies show that the sonic multiphase flow phenomenon in converging –diverging nozzles has not yet been addressed. Also, for studies focused on determining the sonic velocity in two phase mixtures and showed that sonic velocity in two-phase mixtures is much lesser than the sonic velocity of the pure liquid.

3 Experimental Description

3.1 Introduction

Two-phase flow experiments were designed to explain some of the basic properties of single-phase and two-phase flow such as heat transfer and pressure drop in a test section. The experimental facility was designed and constructed to investigate cooling in the diverging section of a nozzle oriented horizontally. The nozzle assembly (which will be denoted as the test section) was located in a position where switching to a different test section is easy. This experimental facility was designed to withstand working pressures in the range of 3000kPa. Apart from the test section, a pump and heat exchangers were the major components in the refrigerant flow. Figure **3.1** shows the schematic diagram of the experimental facility. The pump and the nozzle assembly were connected in a closed loop with additional plumbing to allow for charging and discharging the refrigerant. Three heat exchangers in the refrigerant loop are necessary to maintain the constant inlet temperature of the nozzle. The nozzle assembly was electrically heated by cartridge heaters. The experimental facility consisted of the nozzle assembly, the refrigerant loop, back pressure loop and water loops. The following subsections will describe the details of the nozzle, refrigerant, and auxiliary loops (one back pressure and two water loops) along with their associated instruments.

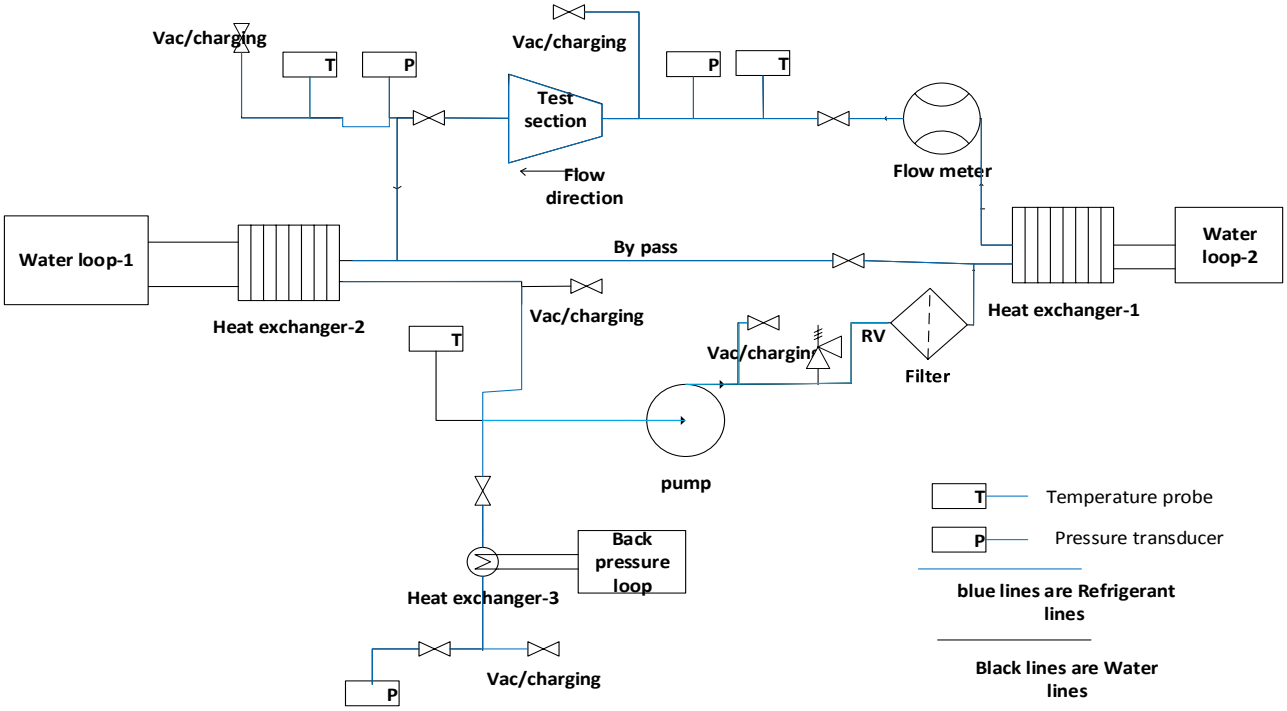

Figure 3.1 Schematic diagram of the refrigerant loop

3.2 Test section

Figure **3.2** shows the 3-D diagram of the test section. The test section consists of a converging-diverging nozzle made of aluminum alloy type 6061. Unlike a single piece nozzle, it is an assembly of many different sections of nozzle. Each section has different lengths as shown in Figure **3.3**. The internal passage of all test sections has a 1° diverging growth angle with respect to the center line of the nozzle. This test section was designed to withstand both high and low pressures as well as high temperatures. As the refrigerant circulates through the nozzle assembly past the minimum area point (the throat), the flow sees an expansion. As it flows down the expansion portion, a sonic flow region is created in which the flow accelerates lowering the pressure and temperature.

The test section has fixtures for the temperature sensors and pressure transducers. These temperature sensors measure the wall temperature; the saturation temperatures are determined from the pressure transducers. These nozzle sections have been designed in such a way that the static pressure and wall temperature of the entire fluid passage is measured. Each test section also has fixtures for the heater. These heaters are embedded only in the aluminum pieces; they do not have any contact with the fluid passage. The inner dimensions of the nozzle depend on the throat and the diverging sections of the nozzle.

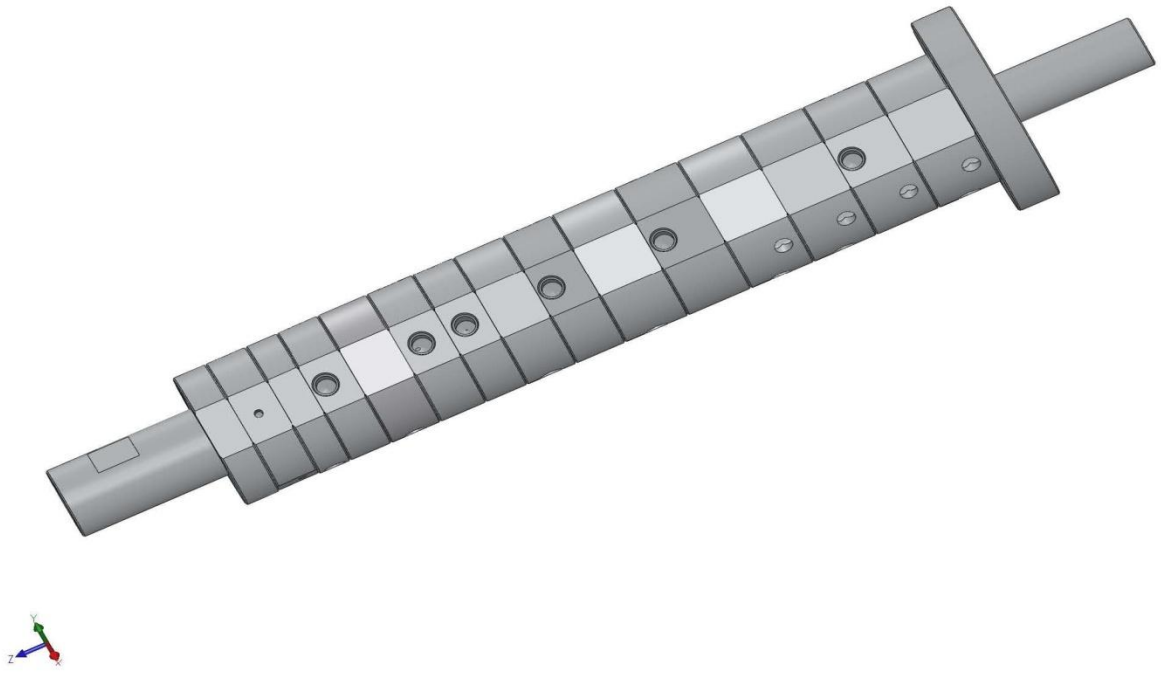

Figure 3.2 3-D view of the Test Section

3.2.1 Test section dimensions

This document shows results from experiments performed on four different test sections; these test sections have two different throats (1.5 mm and 2.43 mm), different heater lengths (200 mm, 125 mm) and different fluids (R134a, R123). Test Section-1 is a combination of throat 2.43mm, 200 mm heater length and R134a working fluid. Similarly, Test Section-2 is the combination of the 1.5 mm throat, a 200 mm heater and R134a working fluid. Test Section-3 is similar to the Test Section-2 but with the 125 mm heater. Similarly Test Section-4 is the combination of the 1.5 mm throat, a 200 mm heater and R123 working fluid.

The outer diameters of all of the test sections are 54 mm. The length of the nozzle depended on the number of nozzle sections assembled together. Figure **3.3** shows the housing diagram and its dimensions for Test Section-1. Table 3.1 shows the different test sections and their fluid passage dimensions. As shown in Table 3.1, Test Section-1 was made from the assembly of 13 sections starting from a 2.43 mm throat. Figure **3.4** gives the fluid passage dimensions by showing the cross section of the test section. The increase of these dimensions along the nozzle shows the 1° growth. Referring to Test Section-1 in Table 3.1, the beginning dimension of the second section is 2.43 mm, after the throat it is 2.43 mm, and the ending diameter of the second section is 2.7 mm (giving a 1° expansion). The other test sections are constructed similarly.

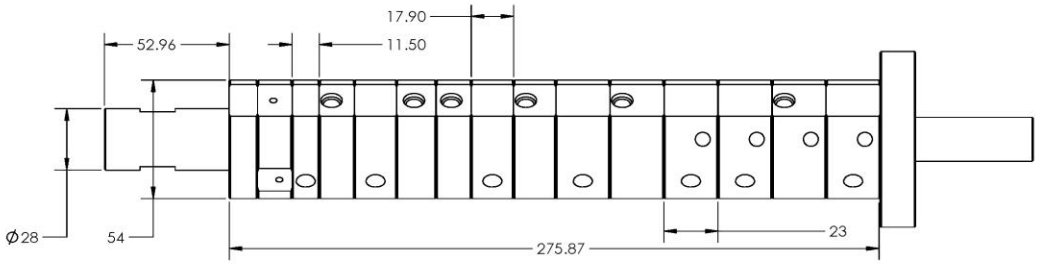

Figure 3.3 Test section housing

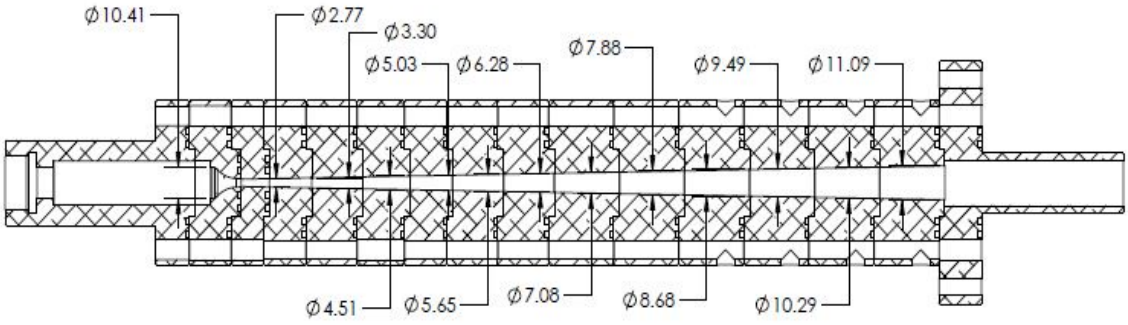

Figure 3.4 Test section inner dimensions

Table 3.1 Test section fluid passage dimensions

	Test Section-1			Test Section-2			Test Section-3			Test Section-4		
	Min. dia(mm	Max.dia (mm)	Length (mm)	Min. dia(mm)	Max.dia (mm)	Length (mm)	Min. dia(mm)	Max.dia (mm)	Length (mm)	Min. dia(mm)	Max.dia (mm)	Length (mm)
Throat	2.43	2.43	10.5	1.50	1.73	14.71	1.50	1.73	14.71	1.50	1.73	14.71
Div-1	2.43	2.77	10	1.73	2.08	10	1.73	2.08	10	1.73	2.08	10
Div-2	2.7	3.3	15	2.08	2.43	10	2.08	2.43	10	2.08	2.43	10
Div-3	3.3	3.92	18	2.43	2.77	10	2.43	2.77	10	2.43	2.77	10
Div-4	3.92	4.5	16.7	2.77	3.30	15	2.77	3.30	15	2.77	3.30	15
Div-5	4.5	5.03	15	3.30	3.92	18	3.30	3.92	18	3.30	3.92	18
Div-6	5.03	5.65	18	3.92	4.55	18	3.92	4.55	18	3.92	4.55	18
Div-7	5.65	6.28	18	4.51	5.03	15	4.51	5.03	15	4.51	5.03	15
Div-8	6.28	7.08	23	5.03	5.65	18	5.03	5.65	18	5.03	5.65	18
Div-9	7.08	7.88	23	5.65	6.28	18	5.65	6.28	18	5.65	6.28	18
Div-10	7.88	8.68	23	6.28	7.08	23	6.28	7.08	23	6.28	7.08	23
Div-11	8.68	9.48	23	7.08	7.88	23	7.08	7.88	23	7.08	7.88	23
Div-12	9.48	10.28	23	7.88	8.68	23	7.88	8.68	23	7.88	8.68	23
Div-13	10.28	11.08	23	8.68	9.48	23	8.68	9.48	23			
Div-14				9.48	10.29	23	9.48	10.29	23			
Div-15				10.29	11.09	23.00	10.29	11.09	23.00			

Installing the nozzle required arranging all the nozzle sections listed in Table 3.1. The assembled nozzle mounted between the inlet and outlet sections of the test facility. The nozzle assembly was held together by a tie rod, on both sides of the nozzle. The cartridge end of the heaters was installed into the heater fixture on the nozzle, and the other end connected to the variable auto transformer to control the voltage. The inlet and outlet of the nozzle connected to the rest of the system via Swagelok fittings.

3.2.2 Test section instruments and calibration

Figure **3.5** shows the instruments connected to the test section. The main instruments used are pressure transducers, temperature sensors, and a flow meter. All the fluid temperatures are measured from high quality K-type thermocouples. These temperature transducers are manufactured by Omega Engineering Inc. They are 15cm long, have 0.032mm sheath diameter, and are ungrounded. The temperature sensor model is KMQSS-032U-6. The pressure transducers used in the facility are from Viatran. The range of the all the pressure transducers is 0-1000kPa except the inlet pressure transducer of the Test Section, which has a range of 0- 3500 kPa. The flow meter used in this facility was a Micro Motion CMF-050 Elite.

A constant temperature bath was used to calibrate the temperature probes. Initially all the temperature probes were connected to the data acquisition system (DAQ) and the other end of the temperature probes was placed into the constant temperature bath. The temperature of the bath was set to different values, and the temperatures measured by the DAQ. A linear regression model between the set value and DAQ temperature value was constructed.

Calibrating the pressure transducers required a manifold that can accommodate 10-15 pressure transducers at a time for calibration. The pressure transducers were connected to the manifold and were read by the DAQ system. The present experimental facility operated from a vacuum to above atmosphere conditions.

The following procedure was used:

- Initially, the manifold was left open to the atmosphere, and the voltage from the pressure transducers was measured from the DAQ system.
- Then the manifold was connected to the vacuum gauge, and the other end of the vacuum gauge was connected to the vacuum pump.

- The voltage readings were then taken with the DAQ system when the pressure transducers reached steady state.
- Similarly, the manifold was then connected to a deadweight tester and the voltage values for pressures above atmospheric were taken from the DAQ.
- A linear regression model was then constructed between the pressure and voltage, and the scale factor and offset of the pressure readings were found. Finally, the scale factor and offsets were applied in DAQ system.

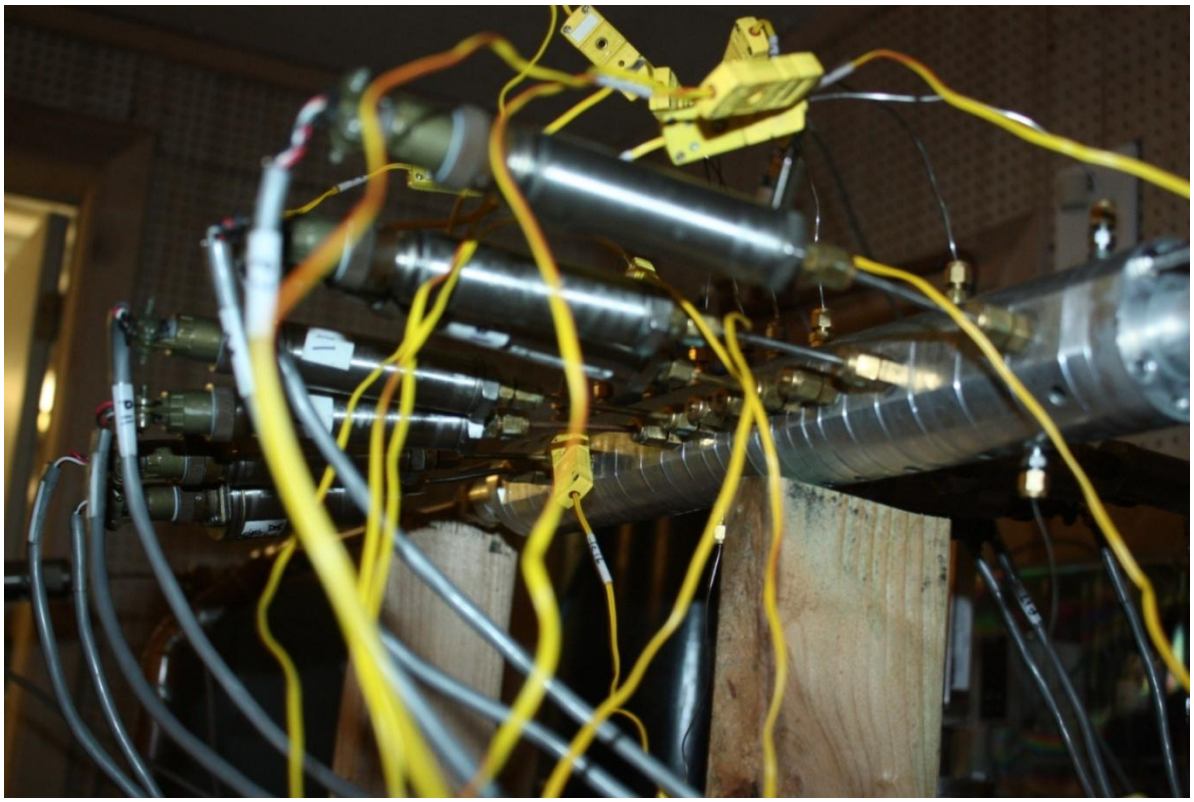

Figure 3.5 Pressure and temperature sensors assembled to the test section

3.2.3 Temperature and pressure measurements in the nozzle

Table 3.2 Temperature and pressure tap distance along the nozzle

	Test Section-1		
	T-distance(mm)	P-distance (mm)	section length(mm)
Throat	5.25	N/A	10.5
Div-1	15.5	11.5	10
Div-2	26	20.5	15
Div-3	42.5	35.5	18
Div-4	61.85	53.5	16.7
Div-5	75.7	70.2	15
Div-6	92.2	85.2	18
Div-7	110.2	103.2	18
Div-8	130.7	121.2	23
Div-9	153.7	144.2	23
Div-10	176.7	167.2	23
Div-11	199.7	190.2	23
Div-12	222.7	213.2	23
Div-13	245.7	236.2	23

Table 3.2 shows the temperature and pressure tap distances of Test Section-1. These distances represent the distance of the instrument from the throat. This test section contain 13 diverging sections, each section has a tap for temperature and pressure transducer. For example, the section div-1 contains the pressure tap at a distance of 11.5 mm from the throat and the temperature tap at 15.5mm from the throat. The other sections are listed similarly. The temperature and pressure taps were fitted with Swagelok fittings. The unused pressure taps were

sealed by plugs. The unused temperature taps did not need sealing because they do not go all the way into the nozzle passage. In fact, the temperature tap holes stop 1 mm from the nozzle surface.

3.3 Refrigerant loop

Figure **3.1** shows the refrigerant loop. The outlet of the test section was on the low pressure side of the test circuit. Heat Exchanger-2 was immediately following the test section and was a 102.4 kW (29 tons) brazed plate heat exchanger manufactured by Alfa-Laval. The water loop-1 ran through the other side of Heat Exchanger-2. The refrigerant pump was located downstream from the heat exchanger. This refrigerant pump was a positive displacement pump from Hydra-Cell with a capacity of 7.8 GPM (i.e. gallons per minute) and a maximum discharge pressure of 7000 kPa. The pump discharge was connected to a Sporlan filter. Heat Exchanger-1 is located after the filter, on the high pressure side of the test section (inlet side). Its purpose was to maintain the liquid refrigerant inlet temperature at a constant set point. Directly after the heat exchanger, there was a coriolis flow meter manufactured by Micro Motion (model ELITE CMF050). This flow meter measured the mass flow and density of the fluid. Finally, immediately after the flow meter, the sub-cooled refrigerant entered the test section (nozzle assembly).

3.4 Auxiliary loops

This experimental facility had three auxiliary loops, two were the water loops and the third one was the back pressure loop. The two water loops in the current facility, as shown in Figure **3.1**, each consisted of a heat exchanger, a pump, a filter and a heater coil. Figure **3.6** shows a schematic for one of them. The two water loops have the same design; One is on the low pressure side of the test section, the other one is on the high pressure side of the test section.

The function of the water loop is to maintain a constant refrigerant inlet temperature. A Shertech ½ hp centrifugal pump is used to circulate the water inside the each water loop, and a 0.5 ton Alpha- Laval plate heat exchanger is located on the downstream side of the pump. The heat exchanger was cooled with industrial water. The immersion heater used in this loop was modulated by a temperature controller to maintain water at a constant set point.

Figure **3.7** shows the backpressure loop. Water is the working fluid. The equipment in the circuit is similar to the water loop, as shown in Figure **3.6**, with the exception that the coil heat exchanger in the back pressure loop is located at the highest point of the experimental facility. The purpose of the loop is to set a known pressure in the refrigerant loop by maintaining a saturation pressure at the highest point in the test section. This also maintains a static pressure on the inlet of pump.

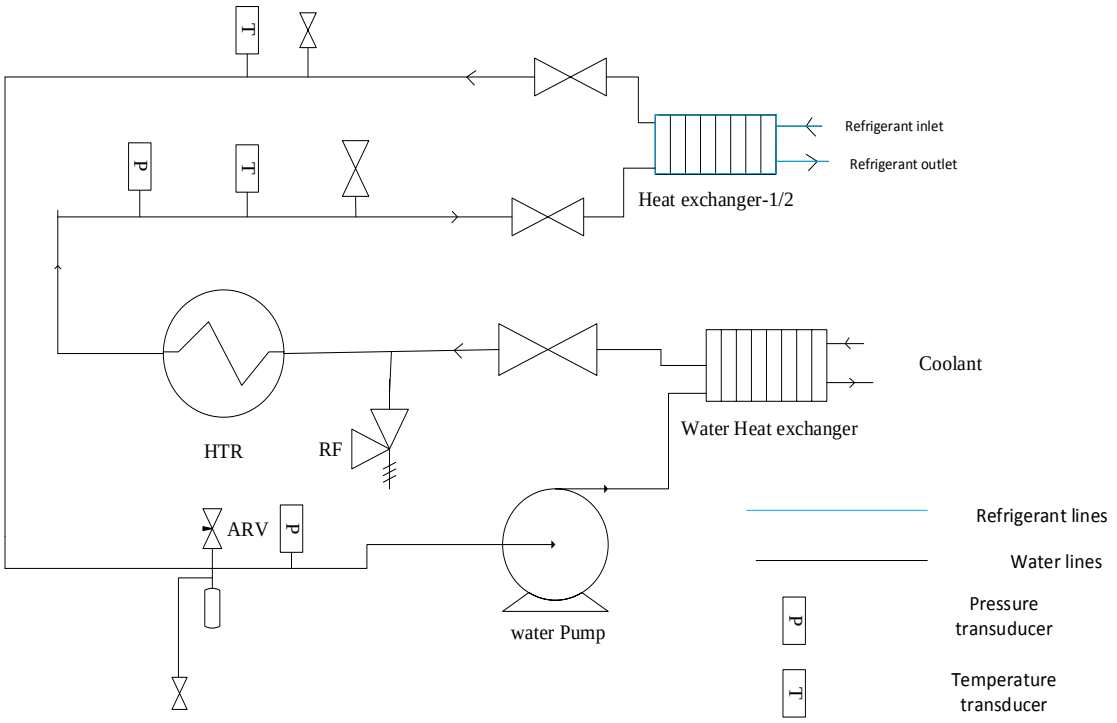

Figure 3.6 Water loop

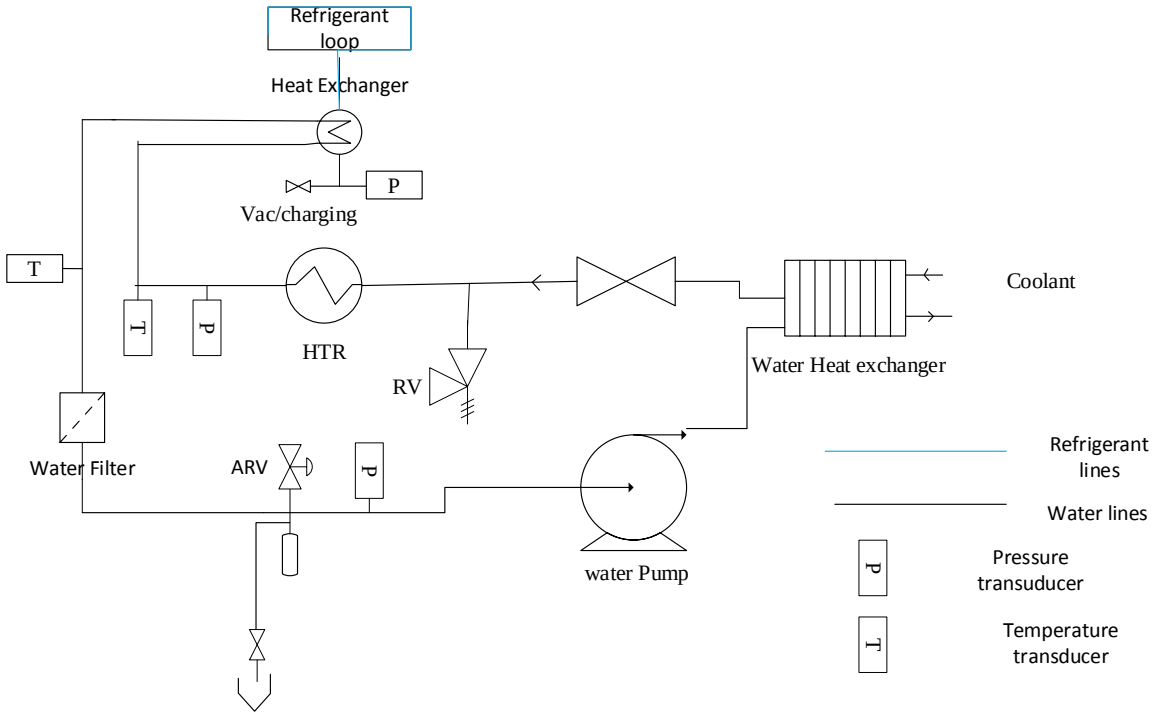

Figure 3.7 Back pressure circuit

3.5 Experimental description and operating conditions

This section describes the procedure that was followed when brining the system into operation. Initially the test section was insulated from the environment and isolated from the test circuit. Then the test circuit and the test section were vacuumed separately with an external vacuum pump. The test section and the test circuit without the test section were then filled with dry nitrogen gas to carry out a leak test. A vacuum was reestablished after the leak test was completed. The inlet and outlet valves to the test section were then opened. The refrigerant was first added to the test circuit in the vapor form with the test section isolated. This procedure was followed each time the test section was filled to prevent non-condensable gases from entering the test circuit.

The back pressure and water loop circulation was started by switching on the corresponding pumps. Once the inlet temperature of the test section reached the set value, the main refrigerant pump was started. Measurements were taken as soon as the system reached steady state. As indicated by uniform temperature and pressure of the refrigerant in the nozzle

This facility operated under two conditions: adiabatic (unheated) and diabatic (heated). The controlling variables in the facility were the throat velocity, inlet temperature, and back pressure saturation temperature, but all the experiments were performed only by changing the throat velocity. The inlet temperature and back pressure saturation temperatures were set as a constant. Throat velocity can be controlled from the pump variable frequency drive (VFD), and similarly inlet temperature and back pressure temperatures were controlled by the two separate temperature controllers. The voltage given to the test section heater was set based on the average wall temperature of the heated portion of the nozzle. The voltage was adjusted through a variable

auto transformer until the average wall temperature reached to the desired wall temperature of the heated portion of the nozzle.

3.6 Data acquisition

The data acquisition system (DAQ) was an Agilent 44970 A. The DAQ connects to a PC via a GPIB interface cable. This DAQ unit was controlled by a program written in Lab VIEW 8.5 from National Instruments. The Lab VIEW program recorded the data from all the instruments for every 5 second intervals in comma separated values (csv) format when prompted by the user.

3.7 Conclusion

This chapter presented the details of the test facility, test section and its fluid passage dimensions. It also presented the facility's equipment, operating conditions and instruments. The test section was a converging-diverging nozzle which was an assembly of diverging nozzle sections. All nozzle sections had a one degree growth angle with the center line of the nozzle sections. Four different test sections were presented in this thesis. These test sections have 2.43mm and 1.5mm throats. R123 and R134a were the working fluids. The test section was designed to measure the temperature and pressure of the entire fluid passage of the nozzle.

The experimental facility had one refrigerant loop, two water loops and one back pressure loop. The function of water loop and back pressure loops was to maintain the inlet temperature and back pressure saturation temperature of the fluid to set value.

4 Data Analysis

4.1Introduction

Nozzle performance can be evaluated by finding the heat transfer coefficients of the fluid in each section of the nozzle. The heat transfer coefficients reported in this research are the average heat transfer coefficients for each nozzle section. The heat transfer coefficients was calculated over a range of heat fluxes, nozzle wall temperatures and fluid saturation conditions. The data analysis equations will show that the experimentally determined heat transfer coefficients are very dependent on the heat flux calculated at the wet surface of the nozzle. The actual heat flux on the wet surface of the nozzle was difficult to determine, but two outer limits was determined by taking certain assumptions. The first assumption was that no heat was conducted between the sections of the nozzle. If this was the case, then all heater power originating in any one section arrived at the wet surface of that section. This is denoted as the insulated model (infinite contact resistance between sections). The other possible assumption was to assume no contact resistance between the nozzle sections; thus allowing conduction in the nozzle. This model was denoted the solid model. These two models provided two methods of calculating the heat flux. The true value of the heat flux will fall somewhere between the results calculated from these two models since the actual system will have some but not infinite contact resistance between the sections. Although the end goal of the analysis was to calculate the heat transfer coefficient, the steps necessary to calculate the heat flux, quality, void fraction, and Mach number are also shown in this chapter. Furthermore, this chapter includes an uncertainty analysis for the average heat transfers coefficients from each section using the propagation of error method.

4.2Two-Phase Heat Transfer Coefficients

The heat transfer coefficient (h) between the nozzle wall and a passing fluid is defined from Newton's Law of cooling as

$$h = \frac{\ddot{q}}{T_w - T_{fluid}} \tag{4.1}$$

Where $\ddot{q}$ is the heat flux, T_w is the temperature of the wall, and T_{fluid} is the fluid temperature. The fluid temperature can be considered to be the saturation temperature because as it passes through the nozzle and it is a two-phase fluid. The heat flux is the amount of heat flowing between the wall and the fluid on a per area basis. For the heated case, assuming that the nozzle is well insulated, the heat flux can be written as

$$\ddot{q} = \frac{W}{A_s} \tag{4.2}$$

where W is the heater power and A_s is the wet surface area of the nozzle.

The two-phase heat transfer coefficients were calculated from Equation 4.1. The first step in finding the heat transfer coefficient was measuring the wall temperature (T_W). This was accomplished by temperature sensors directly placed on the nozzle. As explained in the experimental description, each section of the nozzle had a temperature probe that was inserted to within 1 mm of the nozzle surface. The hole size and temperature probe size were closely matched. Similarly, there was a provision for measuring the pressure of the liquid in each section. This pressure was then converted to a saturation temperature using property relationships from REFPROP software. The third parameter to determine was heat flux, which was the most difficult parameter to find. The challenges associated with measuring this parameter have led to the development of two different methods that provide limits on the true value of the heat flux.

4.2.1 Insulated model

As explained in the introduction chapter, for the insulated model infinite contact resistance was assumed between the nozzle sections, thus the sections were insulated. The wall temperatures and pressure measurements in a section were considered uniform along the section, and steady state conditions were assumed. Heat supplied to the nozzle was calculated as a function of watts per millimeter. So the length of the heater was important in calculating the amount of heat per each section of the nozzle. The length of the heater in the experiments varied from 125 mm to 200 mm, and the typical length of test section (nozzle assembly) was 270 mm.

The heater with a length of less than 270 mm did not go all way through the nozzle. Due to this fact, the nozzle consisted of a heated zone and a non-heated zone. Since heat supplied to the nozzle was calculated in terms of watts per millimeter, the heat received by each section depended on its length and was assumed to be uniform in that section. If there was no heat going to a nozzle section, the heat flux was assumed to be zero. The heat flux (q_I) of each section was calculated from the heater power for that section divided by its internal surface area (wetted area). Figure **4.1** shows an example of the heat flux (q_I) along the nozzle for R134a with a 2.43mm throat, 200 mm heater length at 50 m/s. The heat transfer coefficients were then calculated from the heat flux divided by $\Delta T = T_{wall} - T_{sat}$. While each section received approximately the same amount of heat, the heat flux decreased exponentially because the surface area increased along the length of the nozzle.

Figure **4.2** shows the heat transfer coefficient (h_I) of the R134a, for the same case. Initially the heat transfer coefficients sharply decreased along the nozzle until 100 mm from the throat. Beyond this the heat transfer coefficients leveled off at about 20000 $kW/m^2 K$. The initial

region of the nozzle has high heat transfer coefficients due to the two-phase flow presence in the nozzle.

The insulated boundary assumption made for the nozzle sections makes the calculation of heat flux very simple. This method is an initial approximation of what the heats transfer coefficients of the sonic nozzle will look like. However, this model breaks down when there is significant conduction between the aluminum sections of the nozzle.

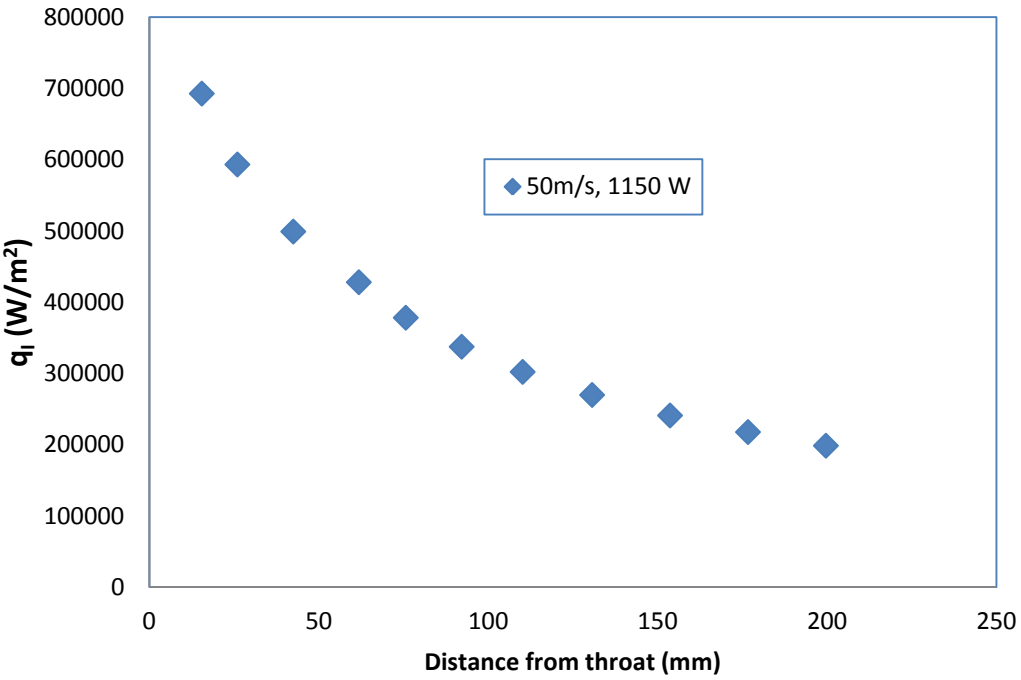

Figure 4.1 Heat flux along the nozzle at 50 m/s for the Test Section -1

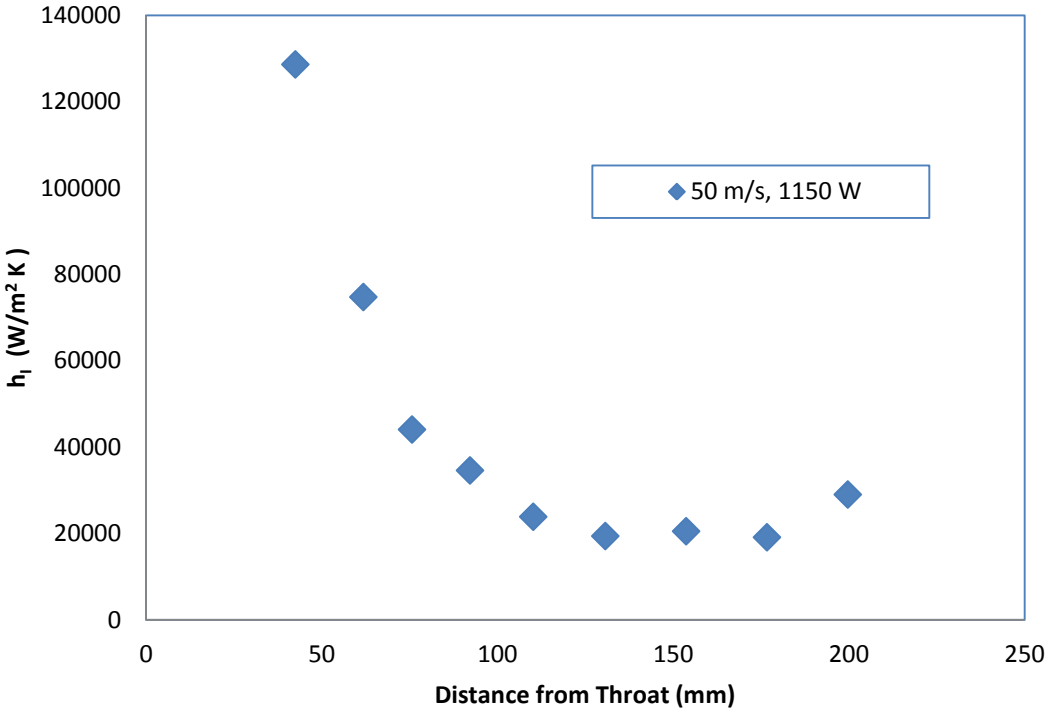

Figure 4.2 Heat transfer coefficients along the nozzle at 50 m/s for the Test Section -1

4.2.2 Solid model

As explained in the introduction, another possible assumption for determining the heat flux for each section is to consider conduction between the sections of the nozzle. That is, the nozzle is one continuous device. This assumption makes the previous method of calculating heat flux invalid since some of the heat from the heater in each section may migrate to the next section instead of directly into the fluid. Determining the heat flux at the nozzle surface thus becomes far more complicated. One method for solving this problem is the use of finite element method (FEM) solving the 3D condition equation numerically by considering the nozzle to consist of small pieces, called elements. This was the method chosen for this research. The simulations were carried out using the commercial software package Solid Works Simulation

Professional 2012. This software was used to create a 3D conduction model for the aluminum nozzle to find the wall temperature and heat flux profiles.

The normal procedure followed in FEM analysis is preprocessing, meshing and post processing. Preprocessing consists of creating the 3-D model, assigning the physical properties to the model, and applying the boundary conditions. Meshing consists of generating a solid fine mesh encompassing the part geometry containing tetrahedron elements. Post processing is actually solving governing differential equations numerically. In this case the results for the simulation were used to calculate the temperature and heat flux plots for the entire nozzle.

The first and most important aspect to solving this problem is applying the boundary conditions to the nozzle surfaces. Once the boundary conditions are set, heat flux values can be found for each element. Using the simulated heat flux, the heat transfer coefficients between the wall and the fluid can be calculated as before by using the equation 4.1.

4.2.2.1 Boundary conditions

Four boundary conditions were set to accurately model the conduction problem occurring in the model. These conditions were the wall temperature, the internal heat generation, the heat flux at the outer surface, and the convection boundary at the nozzle throat. This section describes each of these boundary conditions in detail.

1) Wall temperature:

As described before, the wall temperatures of each nozzle section was directly measured during the experiments. In the previous model, these temperatures were considered to be constant for the entire section. However, this cannot be assumed for the conduction model since conduction between the nozzle sections would allow the wall temperatures on either side of a section boundary to be continuous. In order to apply wall temperatures to a continuous piece of

nozzle, a continuous function of temperature along the nozzle is required so that the sudden change of temperature between the sections can be avoided. In order to do this, the wall temperatures along the nozzle were fit to a cubic spline function. However, to implement that in the simulation, the spline was evaluated at a series of discrete points (every 2.5 mm), and inputted it into the model as a series of set temperatures.

The following steps were used to find the temperatures using the cubic spline function for every 2.5 mm of the nozzle.

a) Assume the temperature distribution is a cubic spline in the form T=CS(x).

b) The spline coefficients are calculated using the measured wall data.

c) Temperatures are calculated from the spline function for every 2.5 mm along the nozzle axis as shown in Figure **4**.**3**.

d) The temperatures are then applied as boundary conditions in the Solid Works 3D conduction model at the wet surface of the nozzle.

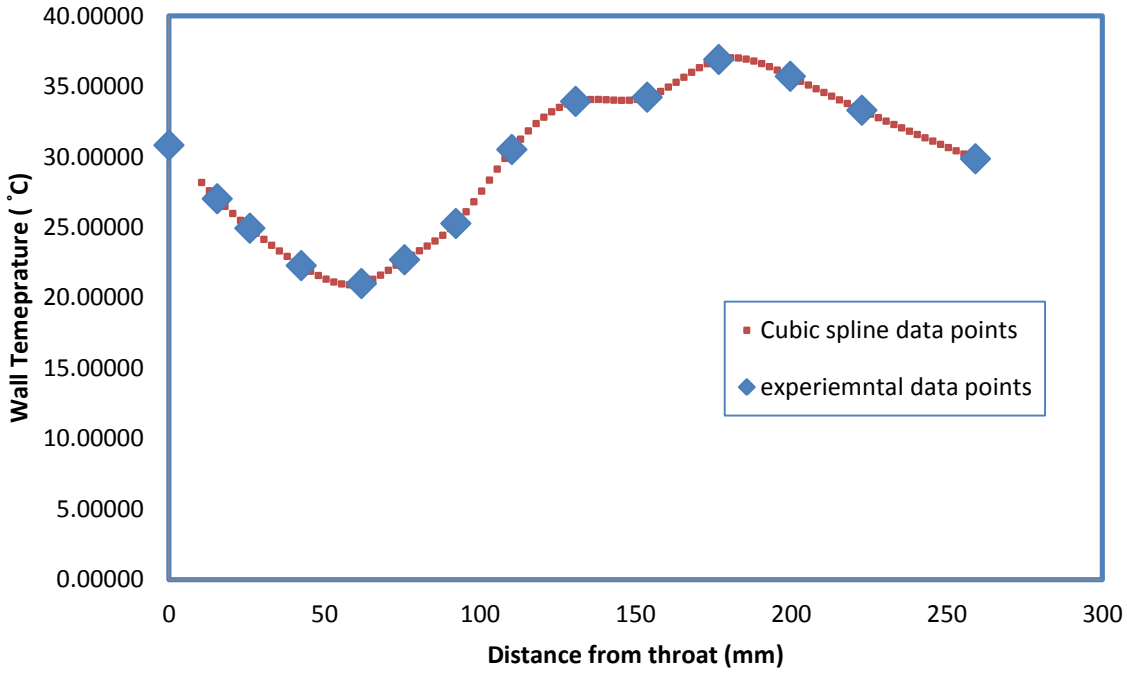

Figure 4.3 Cubic spline data points for the Test Section-1 at 50 m/s

2) Internal heat generation (W):

As described before, heat was added to the nozzle through the heaters during the test. The amount of heat added through heaters was determined based on the average wall temperature of the nozzle. Hence, internal heat generation is considered as one of the boundary condition. Figure **4.4** shows which surfaces received the heat generation boundary condition for Test Section-1. In this case, the heater length was 200 mm and the amount of heat added was 1150 Watts.

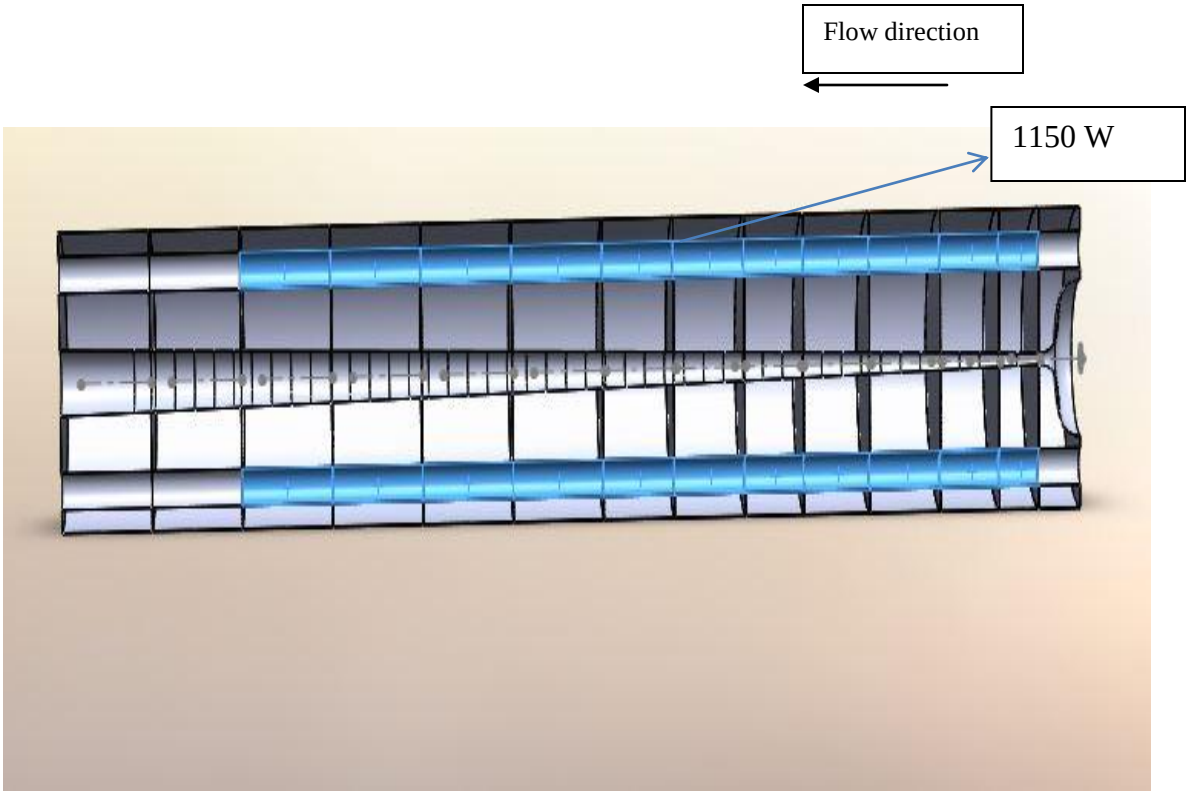

Figure 4.4 Heat addition by 200 mm heater (Test Section-1)

3) Heat flux at the outer surface:

As explained in previous chapter, the nozzle was insulated during the test. This was incorporated in the boundary conditions of the model by making the heat flux applied to the outer surface of the nozzle equals to zero.

4) Convection boundary at the converging section

In the actual nozzle, the heaters were attached in such a way that there are no heaters in the section of the nozzle containing the nozzle throat. Hence, excluding axial conduction, the total heat from the heater will only go into the diverging portion of the nozzle. However, some heat may be conducted into the converging section because of the temperature gradient in the throat section. This heat transfer may raise the temperature and heat flux at the wall in the converging section. While the wall temperature of the converging section of the nozzle was not instrumented, this temperature gradient can be accounted for by setting a convection boundary

condition on this surface. Because of the high mass flow rates in the nozzle, the temperature of the fluid for the convection boundary condition can be taken as the inlet fluid temperature. Because it is known that the fluid is single phase until after the throat, the heat transfer coefficient was taken to be 5000 W/m^2 K. Previous flow boiling studies show that the single-phase heat transfer coefficients are around 5000 W/m^2K. Hence this value applied as the convection boundary condition.

4.2.2.2 Meshing

The mesh discretizes the solid nozzle into small elements as shown in Figure 4.5. The types of elements used for the 3D solid model were tetrahedral solid elements. Tetrahedral solid elements can be either first order (draft quality) or second order (high quality). First order tetrahedral elements have four nodes, straight edges, and flat faces. Second order tetrahedral elements have ten nodes and are more accurate in modeling the problem. Each tetrahedral element had three degrees of freedom for each node, whether 4 or 10 nodes per element. First order tetrahedral elements were used to generate the mesh for this problem. Once the meshing was finished, the model was run, and the temperature plot and heat flux plot were generated as shown in Figure 4.6 and Figure 4.7.

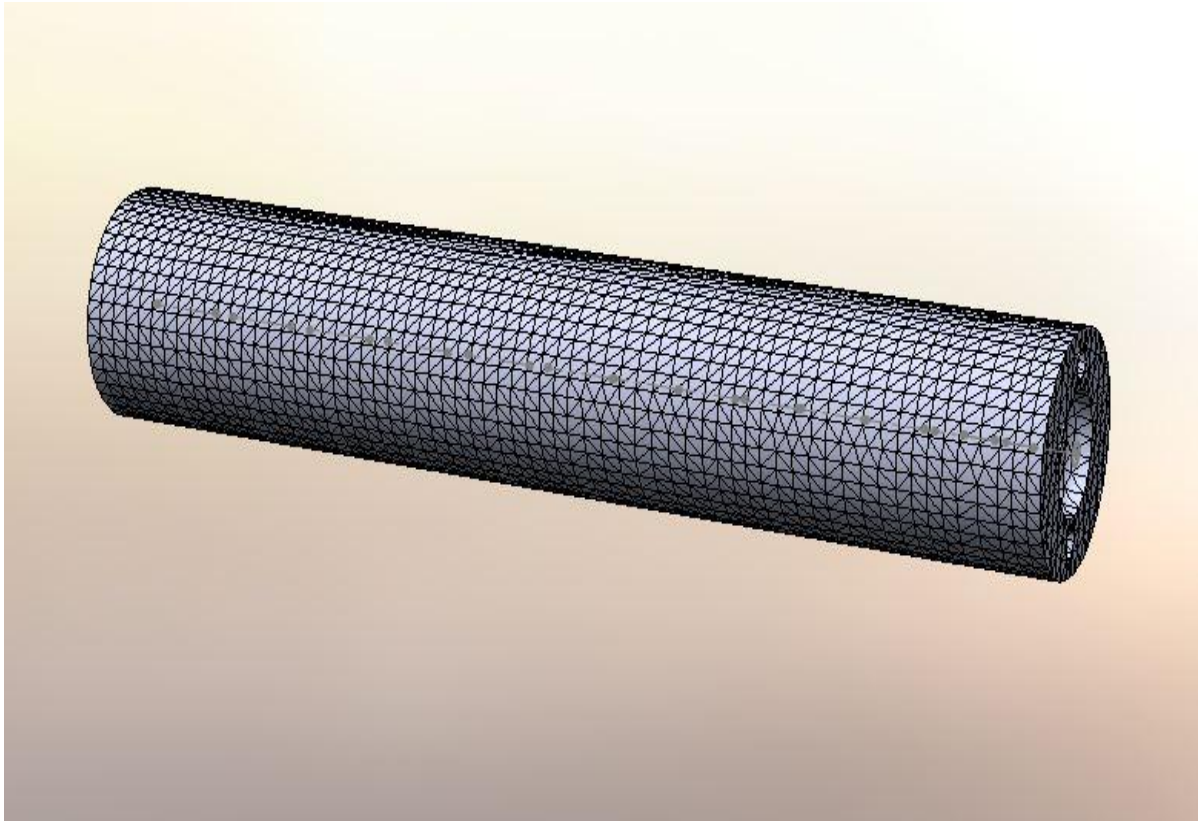

Figure 4.5 Meshing of the nozzle

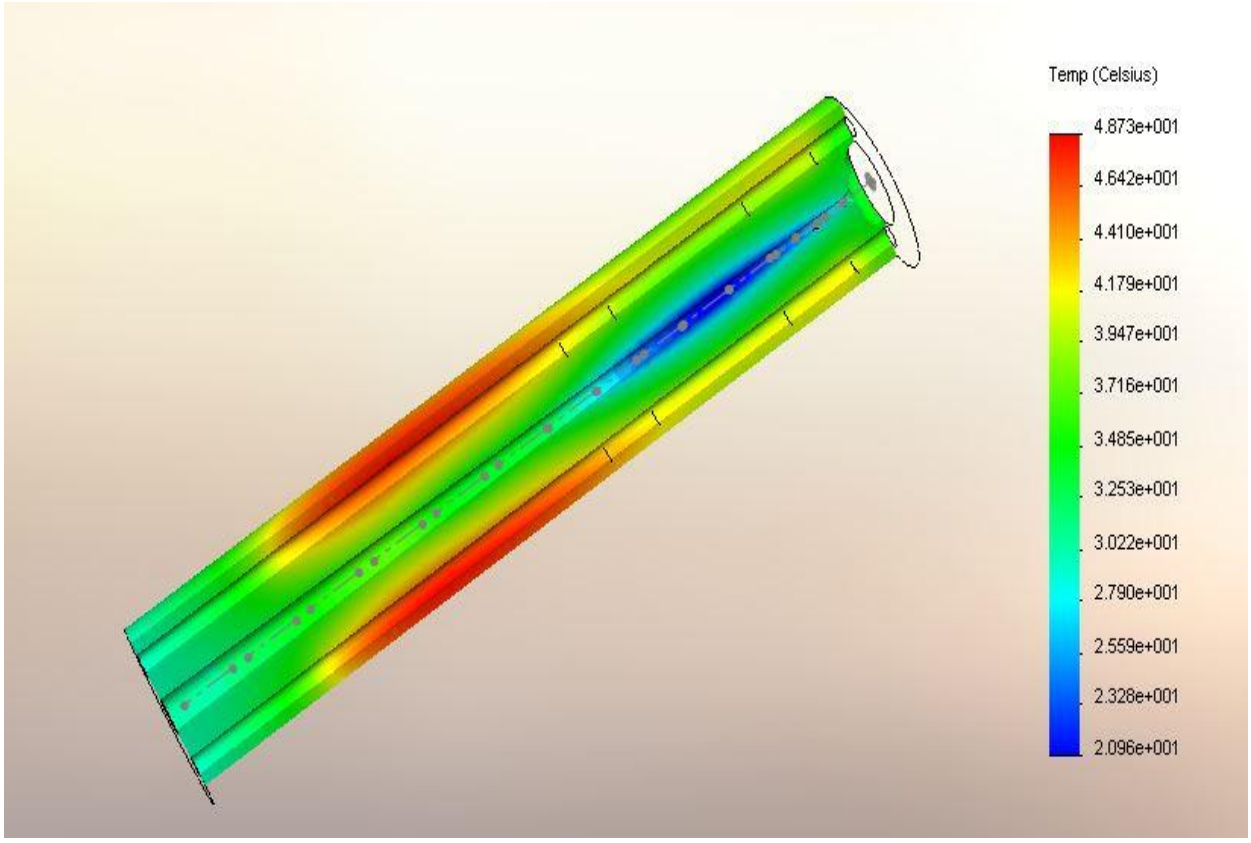

Figure 4.6 Temperature plot from Solid works 3D conduction

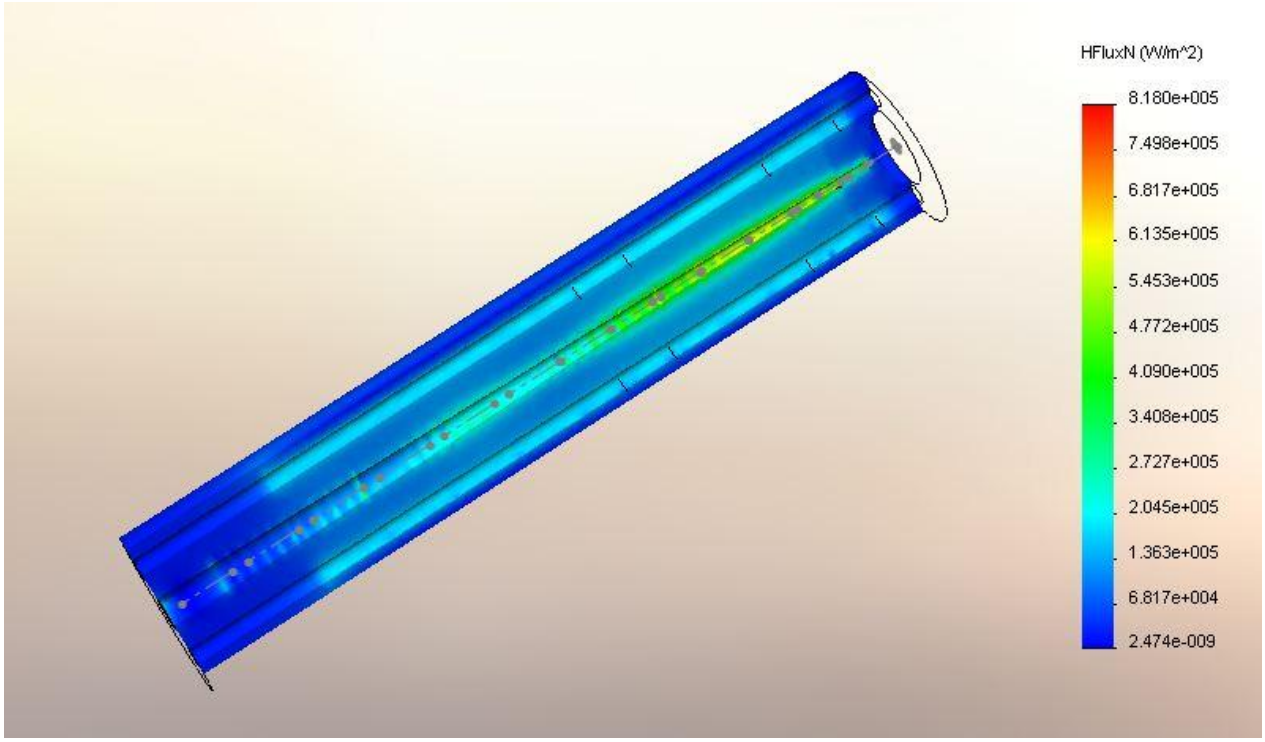

Figure 4.7 Heat flux from solid works 3D conduction

4.2.2.3 Heat transfer coefficient

The simulation outputs included the heat flux values at each element on the wet surface of the nozzle, as shown in Figure 4.7**.** Using these results, the average heat flux values were calculated for each section of the nozzle, as shown in Figure 4.8. The averaging of the heat fluxes was done by taking the arithmetic mean of the heat flux at every node on the nozzle surface boundary. Once the average heat flux values were known, the heat transfer coefficients were calculated using *Equation 4.1*. For example, in the case of Test Section-1, solid model heat transfer coefficients at 50 m/s velocity are shown in Figure 4.9.

Figure 4.10 shows the comparison between the insulated and solid (conductive) heat fluxes for Test Section-1 at 50 m/sec velocity. They both agree well in the middle region of the nozzle 42 mm to 150 mm, but not quite as well at the entry portion of the nozzle. This is because of high conduction due to large temperature change at the entry section (throat) of the nozzle.

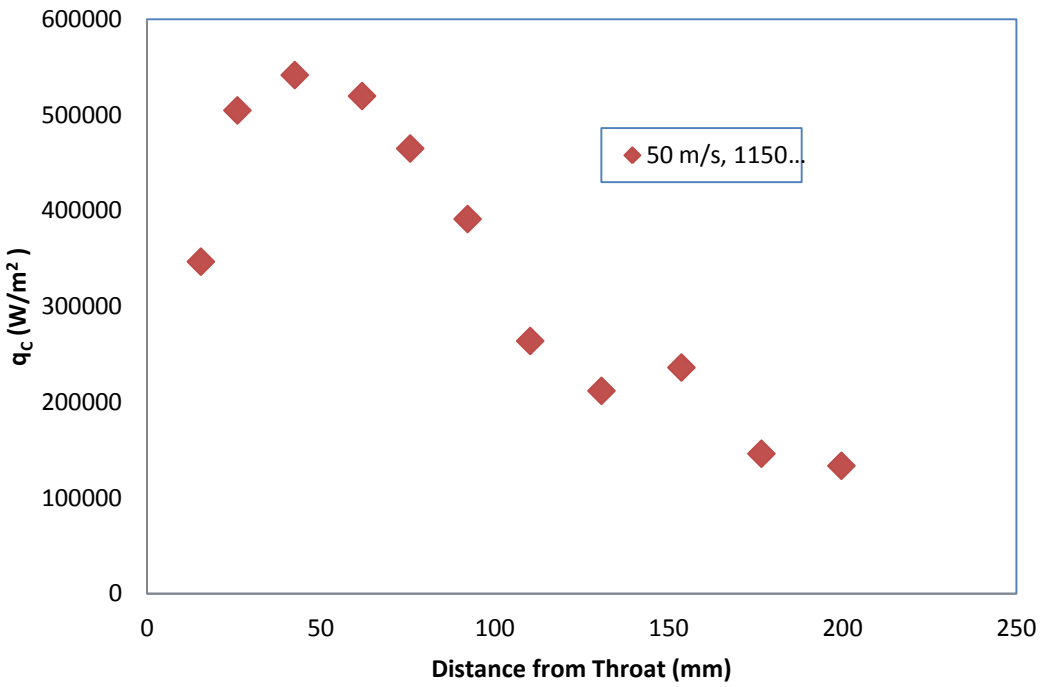

Figure 4.8 Average heat flux of Test Section-1

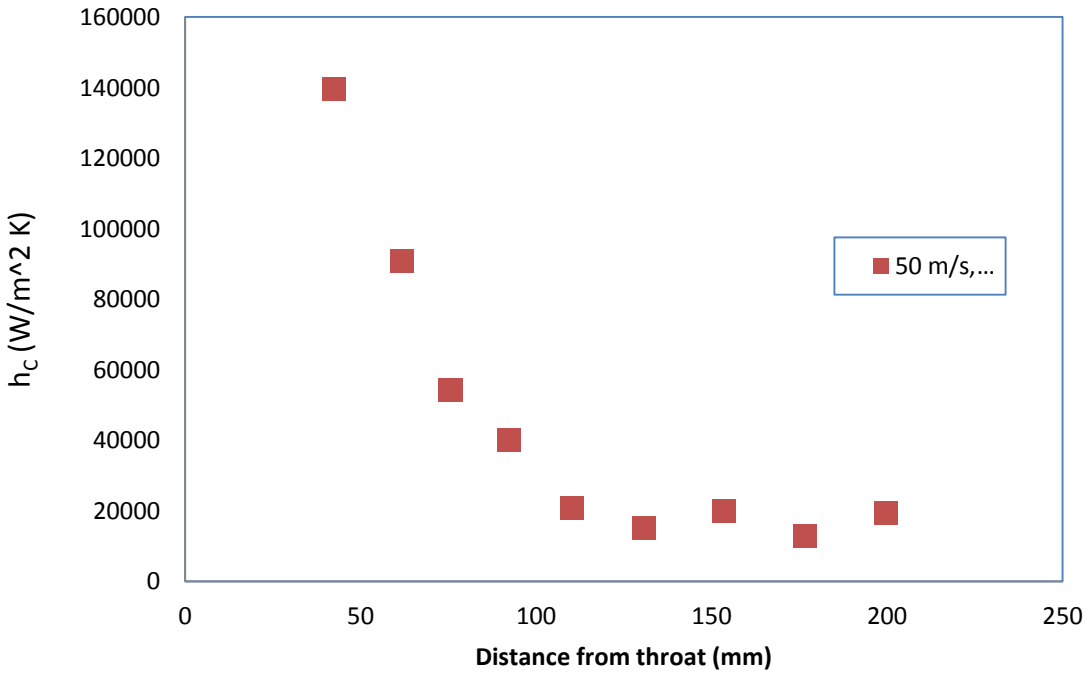

Figure 4.9 Average heat transfer coefficients of Test Section-1

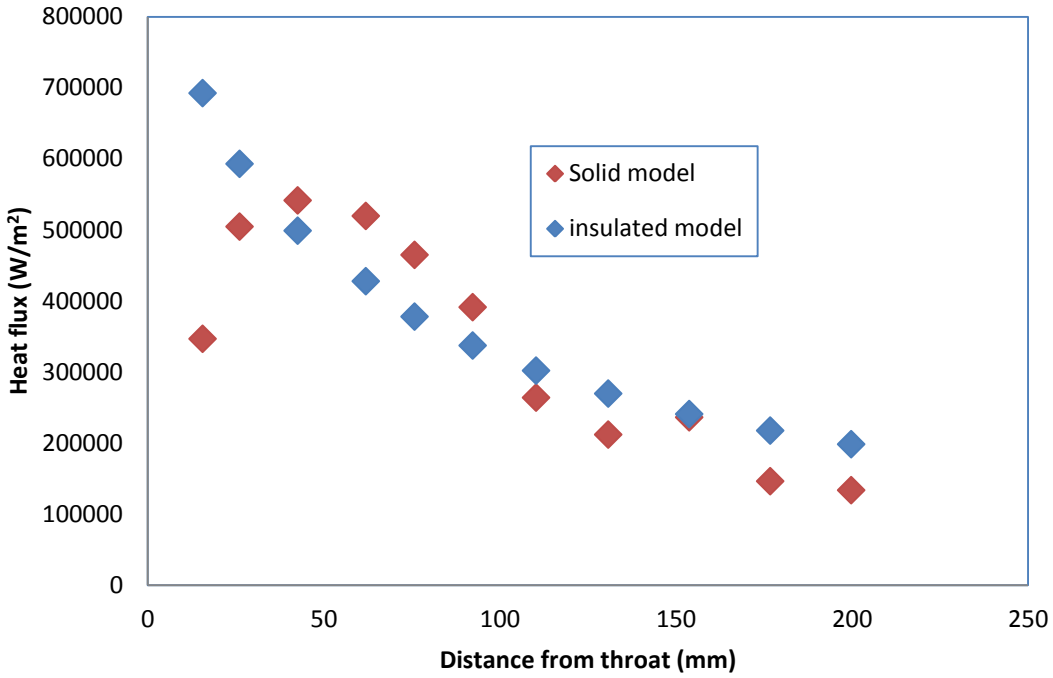

Figure 4.10 Comparison between the insulated and solid model heat flux

4.3Flow Parameters

Various flow parameters were calculated for each of the experimental data points to better understand the relationship between the fluid flow and the heat transfer coefficients. This section shows how these different parameters were calculated from the measured values.

4.3.1 Mass flux

The mass flux was calculated for each section of the nozzle based on the flow area of the cross section of each section of the nozzle. Mass flux was calculated from the equation

$$G = \frac{\dot{m}}{A_{cs}} \tag{4.3}$$

where $\dot{m}$ is the mass flow rate and A_{cs} is the cross sectional area of the associated nozzle section defined by

$$A_{cs} = \frac{\pi}{4} D_{avg}^2$$

where D_{avg} is the average diameter of the nozzle section. the average diameter is also account for the axial position of the nozzle.

4.3.2 Quality

Flow quality along the inside of the nozzle can be found from the energy balance by considering a control volume that consists of the interior of the nozzle from the throat to the nozzle section of interest. The flow quality derived from the energy balance is as follows.

$$\frac{dE_{Cv}}{dt} = \dot{Q}_{Cv} - \dot{W}_{Cv} + \dot{m}(h_i + \frac{v_i^2}{2} + gZ_i) - \dot{m}(h_e + \frac{v_e^2}{2} + gZ_e) \tag{4.4}$$

where $\frac{dE_{cv}}{dt}$ is the rate of change of the energy in the control volume, $\dot{Q}_{cv}$ is the net rate of heat transfer into the control volume, $\dot{W}_{cv}$ is the net rate of work done on the control volume, $\dot{m}$ is the mass flow rate through the nozzle, h_i, v_i, and Z_i refer to the enthalpy, velocity, and height of the fluid entering the control volume and h_e, v_e, and Z_e refer to the enthalpy, velocity, and height of the fluid leaving the control volume. The acceleration of gravity is denoted as g. As explained before, the measurements were taken at steady state and there is no potential height difference along the nozzle. Thus $\frac{dE_{cv}}{dt} = 0$, and the potential energy terms cancel. The equation then becomes

$$\dot{m}(h_e + \frac{v_e^2}{2}) = \dot{Q}_{Cv} + \dot{m}(h_i + \frac{v_i^2}{2}) \tag{4.5}$$

Assume that the fluid is saturated at the throat , so the inlet enthalpy can be directly evaluated from the property tables using the throat temperature. However, the fluid through the diverging section of the nozzle is a two-phase mixture. Thus the expression for the exiting enthalpy is

$$h_e = h_f(T_e) + x h_{fg}(T_e)$$

where x is the flow quality, $h_{fg}(T_e)$ is the latent heat of vaporization evaluated at the exit temperature, and $h_f(T_e)$ is the enthalpy of the saturated liquid evaluated at the exit temperature. Then the equation becomes

$$\dot{m}(h_f(T_e) + x h_{fg}(T_e) + \frac{v_e^2}{2}) = Q_{cv} + \dot{m}(h_f(T_i) + \frac{v_i^2}{2}) \tag{4.6}$$

This expression can be solved for quality to give

$$x = \frac{\dot{Q} + \dot{m}[(\frac{v_i^2}{2} - \frac{v_e^2}{2}) + (h_f(T_i) - h_f(T_e))]}{\dot{m} h_{fg}(T_e)} \tag{4.7}$$

The only other quantity that must be evaluated to use Equation 4.7 to get the quality is the exit velocity of the fluid. This velocity (v_e) was calculated using the homogeneous flow model. According to the homogenous flow model (no slip ratio between liquid and vapor), the volumetric flow rate of the two-phase mixture inside the nozzle equals the sum of the volumetric flow rates of the individual phases. Thus

$$\dot{V} = \dot{V}_g + \dot{V}_l \tag{4.8}$$

where $\dot{V}$ is the volumetric flow rate of the mixture and $\dot{V}_g$ and $\dot{V}_l$ are the volumetric flow rates of the vapor and liquid respectively.

Equation 4.8 can be wrtitten as

$$\dot{V} = \dot{m} x \upsilon_g + \dot{m}(1-x)\upsilon_l$$

where υ_g and υ_l are the specific volumes of the vapor and liquid in the nozzle.

The volumetric flow rate of the mixture in the diverging section of the nozzle is

$$\dot{V} = A_c v_e$$

where A_c is the cross sectional area of the nozzle at the exit of the control volume. Then the velocity of the mixture (the two-phase velocity) can be calculated from the equation below:

$$v_e = G(x\upsilon_g + (1-x)\upsilon_l) \tag{4.9}$$

The quality can then be determined by substituting Equation 4.9 into Equation 4.7. Since both sides of the equation will depend on quality, the final value must be determined through iteration.

4.3.3 Void fraction

Void fraction is used to calculate the Mach number in the diverging section of the nozzle. Void fraction is the ratio of the areas of the vapor to the area of the entire fluid and can be written as

$$\alpha = \frac{A_g}{A}$$

where α is the void fraction, A_g is the area occupied by the vapor, and A is the total area of the mixture. From the homogeneous flow model, the superficial velocity of the vapor phase (v_g) is equal to the superficial velocity of the liquid phase (v_l). These terms can be written as

$$v_g = \frac{\dot{V}_g}{A_g} = \frac{\dot{V}_g}{A\alpha} = \frac{\dot{m}x}{\rho_g A\alpha}$$

and

$$v_l = \frac{\dot{V}_l}{A_l} = \frac{\dot{V}_g}{A(1-\alpha)} = \frac{\dot{m}(1-x)}{\rho_g A(1-\alpha)}$$

where ρ_l and ρ_g are the densities of the liquid and gas phase of the mixture. The void faction of the mixture is calculated by equating the above two superficial velocities. This yields for homogenous flow

$$\alpha = \frac{1}{1+\left(\frac{1-x}{x}\right)\frac{\rho_g}{\rho_l}} \qquad 4.10$$

Sonic velocities in two-phase flows are used to calculate the Mach numbers in the diverging section of the nozzle. The Mach number, defined as the two-phase velocity in the nozzle section divided by the sonic velocity in the section, were calculated for each section of the nozzle. The expression for Mach number is

$$M = \frac{v_e}{c} \qquad 4.11$$

Where v_e is the velocity of the fluid at the nozzle section of interest calculated from Equation 4.9 and c is the two-phase speed of sound showed by Brennen (1995).

4.4 Nusselt number ratio (Φ)

Nusselt number ratio (Φ) is defined as the ratio of two-phase Nusselt number to single phase liquid Nusselt number (based on the *Dittus-Boelter (1930)* correlation). This ratio is basically the ratio of two-phase heat transfer coefficients to the single-phase heat transfer coefficients in the nozzle. This ratio helps to decide if the nucleate boiling, convection or wall dry out occurs. Nucleate boiling and convection gives the ratio higher one, while dry out is below one. The two-phase Nusselt number is calculated in each section of the nozzle from the average heat transfer coefficient from the solid model.

$$Nu_{tp} = \frac{h_C\ D_{avg}}{k}$$

where D_{avg} is the average diameter of each nozzle section, h_c is the average heat transfer coefficient, and k is the thermal conductivity of the fluid.

The Nusselt number from the Dittus-Boelter (1930) correlation is given by

$$Nu_l = 0.023 \mathrm{Re}_l^{0.8} \mathrm{Pr}^{0.4}$$

where Re_l and Pr_l are the Reynolds number and Prandtl number of the liquid.

Reynolds number and Prandtl number are calculated from the following formulas:

$$\mathrm{Re}_l = \frac{GD_{avg}}{\mu_l}$$

$$\mathrm{Pr}_l = \frac{\mu_l Cp_l}{K_l}$$

The Nusselt number ratio is therefore

$$\Phi = \frac{Nu_{tp}}{Nu_l}$$

4.5 Uncertainty analysis

An uncertainty analysis was performed on the average refrigerant heat transfer coefficients using the Kline-McClintock (1953) second-order law. To determine the uncertainty in the average heat transfer coefficients, the uncertainty of the input variables in Equation 4.1 must be determined. Measured input variables are saturation temperature, wall temperature and heat flux. Uncertainty estimates for each of these parameters must be made before the uncertainty estimate for the heat transfer coefficients can be calculated.

4.5.1 Temperature uncertainty

Thermocouples were used to measure the wall temperature in the nozzle. The sources of uncertainty in the thermocouples are the calibration error and data acquisition error. The data acquisition system had a voltage measurement uncertainty of ±(0.008% range+ 0.001% reading). For a reading of 50mVA and a range of 500mVA, overall uncertainty is calculated as ±0.071 ^{o}C

from Equation- 4.12 , which is less than manufacturer uncertainty. So the reasonable estimation of the uncertainty in thermocouples is ±0.15 °C of the operating value.

$$u_P \text{ or } u_T = [(\alpha_x u_{xi})^2 + (\alpha_y u_{yi})^2 + (a_1 u_x)^2]^{1/2} \quad 4.12$$

where u_p overall uncertainty in pressure, u_T overall uncertainty in temperature, α_x and α_y are sensitivity coefficients, u_{xi} and u_{yi} are the data acquisition errors, a_1 is the slope of the linear equation between the sensor and voltage, u_x is the uncertainty in x.

4.5.2 Saturation temperature uncertainty

The sources of uncertainty in the pressure transducers are the DAQ error and the curve fit errors. The pressure transducers have ± 0.015% full scale uncertainty. The pressure transducer gives an output signal of 0-5VDC. The data acquisition system reads the voltage with an uncertainty of ±(0.003% reading+ 0.0035% range). The reading is 5VDC, and the range is 10VDC. Curve fit equation can be found from p=f (V). Overall error was calculated as ±0.261kPa from the *Equation 4.12* .

Manufacturer's uncertainty is 0.05% for the range 0-1000 kPa, which is ± 0.5 kPa. Since the uncertainty is higher than the calculated value, for more careful calculations, uncertainty in the saturation temperature assumed as +/- 0.15 °C.

4.5.3 Heat flux uncertainty

Two methods for calculating heat flux are considered in this research: the insulated model and the solid model. Insulated flux is calculated directly from the experimental values; solid model heat flux is from finite element modeling. Thus one method of estimating the uncertainty of the heat flux is looking at the difference between these two values, because these are two

limiting conditions in finding the heat flux. The percentage of uncertainty in heat flux can be calculated from Equation 4.13

$$u_q = \left| \frac{(q_I - q_C)}{\left(\frac{q_I + q_C}{2} \right)} \right| * q_C \tag{4.13}$$

where u_q is the uncertainty in the heat flux, q_I is the heat flux calculated from the insulated model and q_c is the heat flux calculated from the solid model. Uncertainties were calculated separately for each nozzle section. The percentage of uncertainties in heat flux were approximately 5-25% in the sonic region (M>1) and approximately 20-45 % in the subsonic region (M<1) of the nozzle. These uncertainties were calculated separately for each data point of data run.

4.5.4 Overall uncertainty in heat transfer coefficients

Overall uncertainty in average heat transfer coefficients are calculated from Equation 4.14 is based on the input variables as discussed in previous section. The percentage of uncertainties in the heat transfer coefficients were approximately 5-27 % in the sonic multiphase region (M>1) of the nozzle, approximately 20-45% in the subsonic multiphase region (M<1) of the nozzle, and approximately 70 % in the single-phase region of the nozzle.

$$u_h = \left(\left(\frac{\partial h}{\partial q} u_q \right)^2 + \left(\frac{\partial h}{\partial T_W} u_{T_w} \right)^2 + \left(\frac{\partial h}{\partial T_s} u_{T_s} \right)^2 \right)^{1/2} \tag{4.14}$$

here u_h is the uncertainty in heat transfer coefficients, u_q is the uncertainty of the heat flux, u_{Tw} is the uncertainty in wall temperature, and u_{Ts} is the uncertainty in the saturation temperature.

4.6 Conclusion

This chapter presented the methods and equations used in determining the average heat flux and heat transfer coefficients in each section of the nozzle. This chapter also presented methods to find the flow quality, mass flux, sonic velocity and Nusselt number ratio.

Two methods were used in determining the heat flux : insulated method and solid method. In the insulated method, heat flux is calculated based on the input heat given to each section of the nozzle. In solid model, heat flux is calculated from finite element method using solid works professional version-2012. Later the two methods were compared. These two methods represent the limits in determining the heat fluxes and heat transfer coefficients, actual values lies between the two methods. Finally, the propagation of error method was used to determine the uncertainty in heat transfer coefficients, heat flux and temperature.

5 Cooling in Sonic Nozzles

5.1 Introduction

This chapter presents the temperature and pressure profiles for all four test sections. Please refer to the experimental description (Chapter-3) for details about the test sections, working fluids, and nozzle dimensions.

A nozzle assembly starts with a converging section which restricts down to the throat, the minimum cross section area. After the throat, the cross sectional area increases forming the diverging section. Testing is done under steady state conditions indicated by uniform temperature and pressure in the nozzle and the nozzle is insulated from the environment. For each test, inlet pressures vary from 700 kPa to 2500 kPa which results in throat velocities from 20 m/s to 50 m/s. Pressure and velocities roughly related through the Bernoulli equation of ideal flow for the converging section of the nozzle, thus the higher pressures correspond to higher throat velocities. Even though pressure and velocity are linked, velocity is used as the primary designation throughout the chapter. The velocity mentioned above is at the throat of the nozzle. For each nozzle, data was collected according to the test section input table. A set of adiabatic tests and a set of heated tests are presented. The heater power that was used varied with velocity and power was set based on a desired average wall temperature for each run.

5.2Temperature and pressure drop

Figure 5.1 and 5.2 show the wall temperature and pressure of Test Section-1 at a throat velocity of 50 m/s for both the heated and unheated cases. The working fluid is R134a. The x-axis represents the distance (mm) along the nozzle, and zero indicates the throat. Each data point indicated in the plots is measured directly from the temperature sensors and pressure transducers

placed on the nozzle. The inlet temperature and pressure of R134a is 30 °C and 2370 kPa giving a throat velocity of 50 m/s without heater power. It can be observed that the measured fluid pressure drops below the saturation pressure due to the sonic expansion in the diverging portion of the nozzle. In the diverging section the measured temperature also drops to 14 °C, indicating that the fluid is a mixture of vapor and liquid. The pressure of the fluid drops to 450 kPa in the diverging portion of the nozzle then rises back to 770 kPa, which is equal to the inlet saturation pressure.

Figure 5.1 and 5.2 indicate that the fluid stays in the two-phase region from about 15 mm to 200 mm and then condenses back to liquid phase. This condensation of the vapor bubbles happens due to back pressure from the other end of the nozzle. If the flow is sonic, it indicates a condensation shock is occurring in the nozzle. For heat addition, the wall temperatures are higher as expected only falling to 21 °C and then rising above the initial temperature. This is because the low pressure vapor absorbs the energy from the heated wall of the nozzle.

Figures 5.3 to Figure 5.10 show the temperature and pressure profiles for all data points taken in all of the test sections. The data for pressure and temperature show similar trends. For example, single phase liquid starts at the inlet of the nozzle, and all runs show temperatures below the saturation temperature indicating two phase fluid downstream from the throat. The wall temperatures and saturation pressures also decreased, dropping below the saturation zone due to expansion, and then rising to the original inlet temperature and inlet saturation pressure. The general observation from these plots is that increasing the velocity of the fluid causes more cooling (as indicated by lower wall temperatures) to occur inside the nozzle.

R134a is the working fluid for all test sections, except Test Section-4. The working fluid for Test Section-4 is R123. The major observation between the two different working fluids is

the amount of temperature drop. The test section with R134a has more temperature drop than the test section with R123 for the same throat size (1.5 mm).

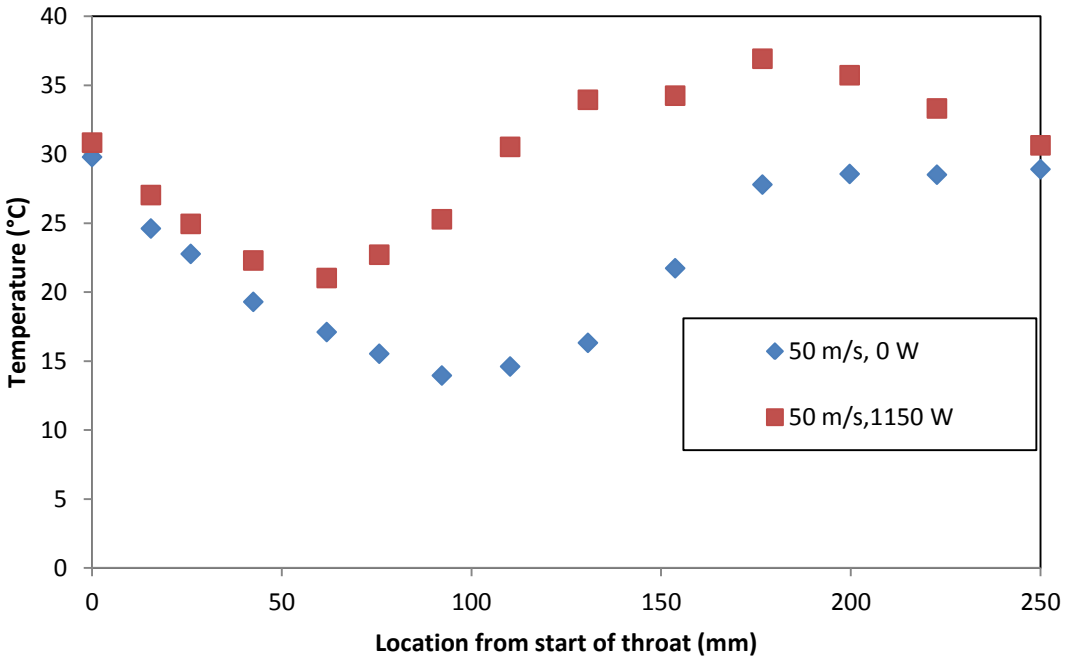

Figure 5.1 Temperature profile of Test Section-1 at 50 m/s

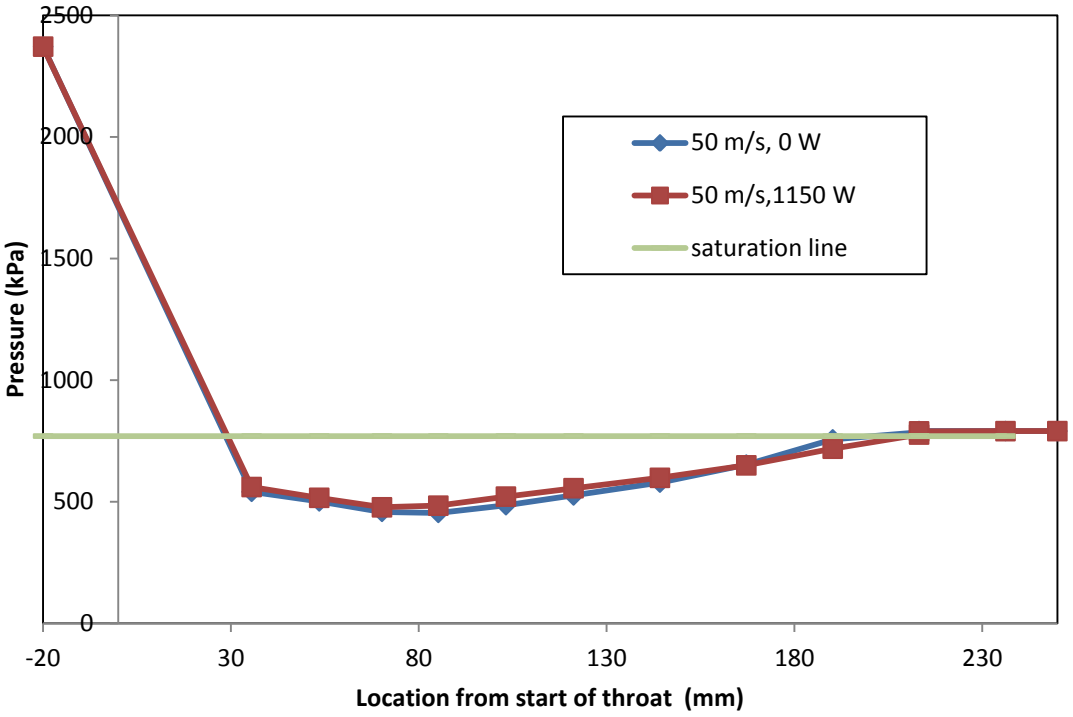

Figure 5.2 Pressure profile of Test Section-1 at 50 m/s

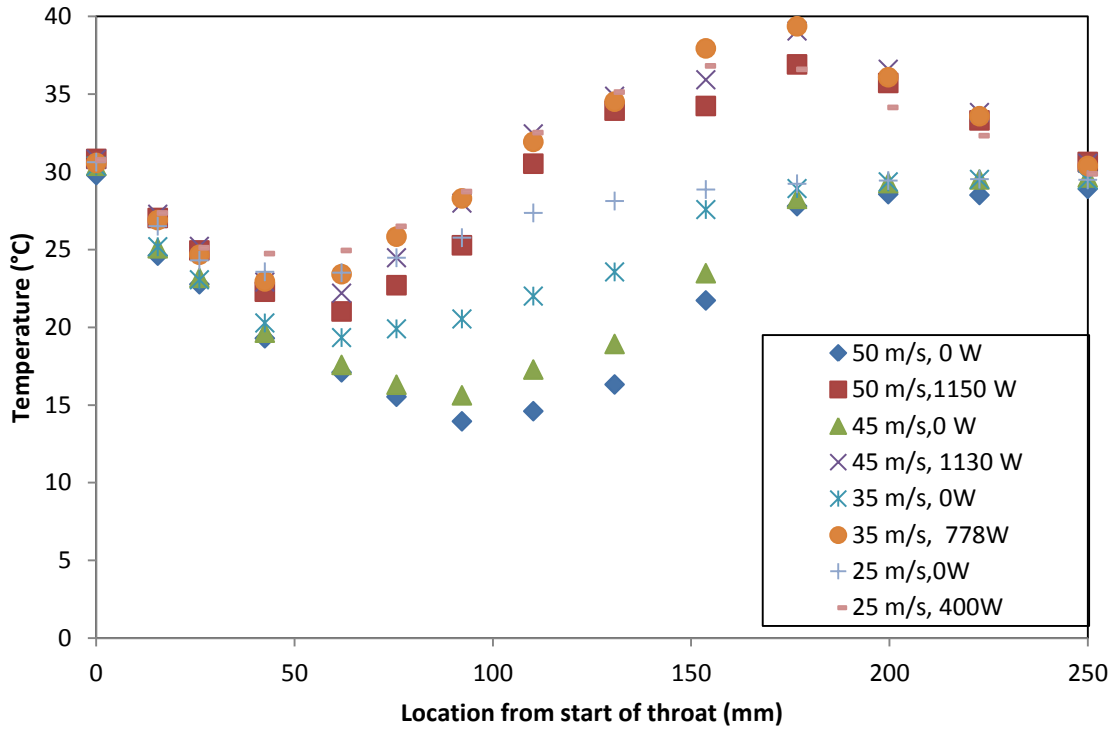

Figure 5.3 Temperature profile of Test Section-1

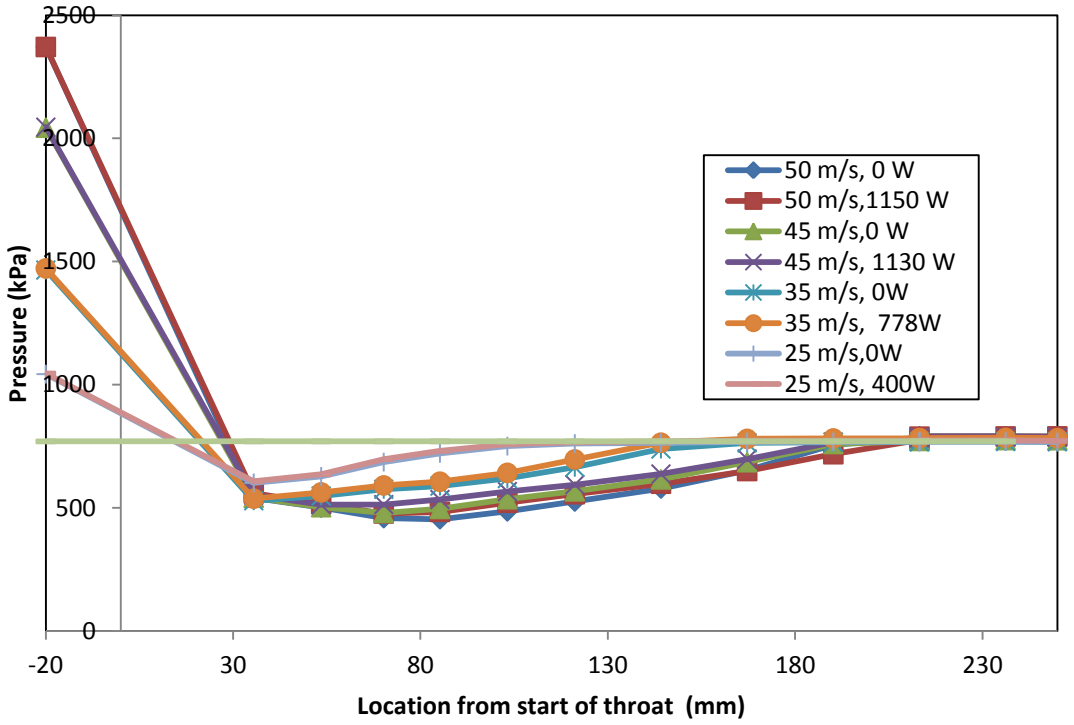

Figure 5.4 Pressure profile of Test Section-1

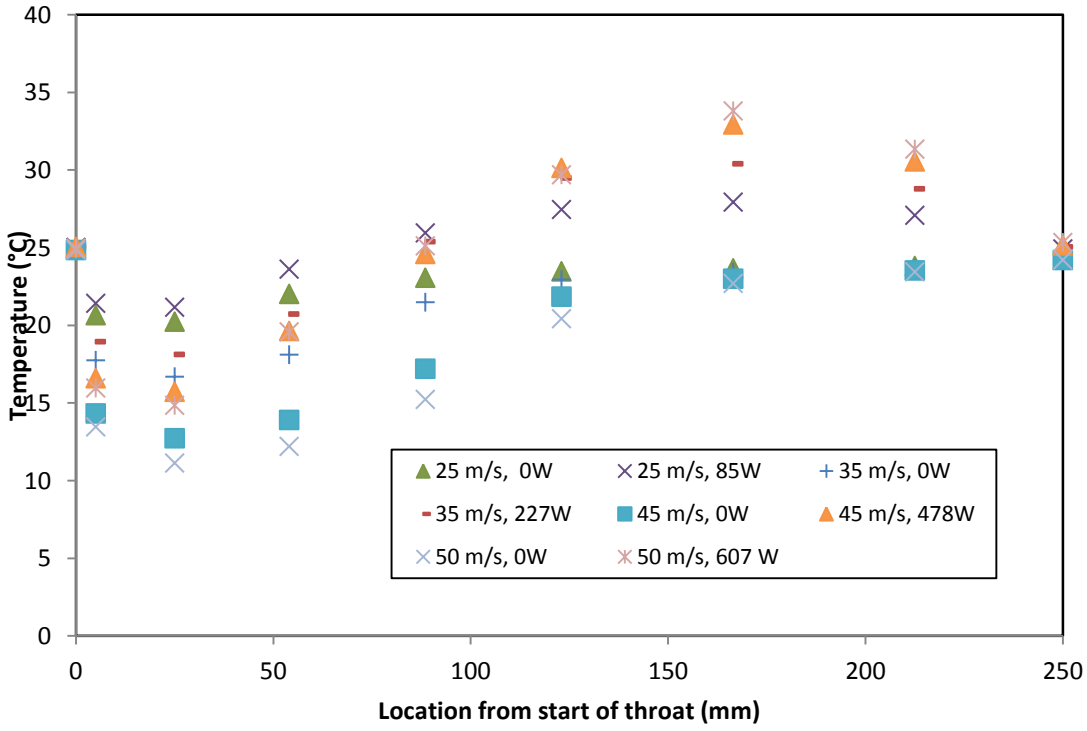

Figure 5.5 Temperature profile of Test Section-2

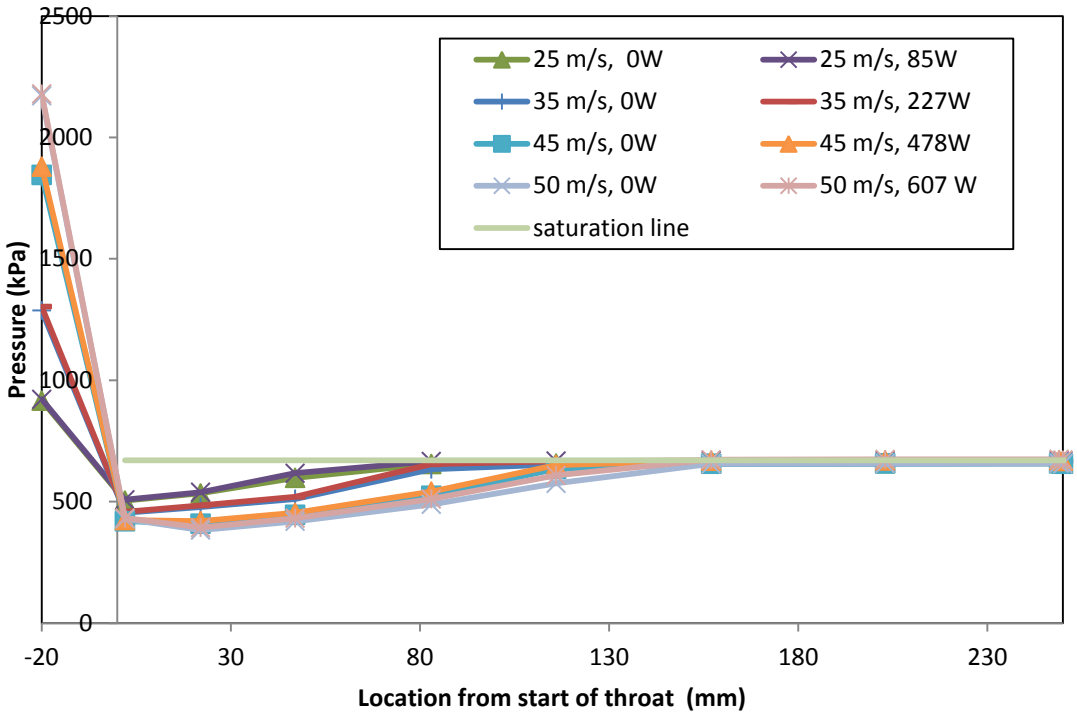

Figure 5.6 Pressure profile of Test Section-2

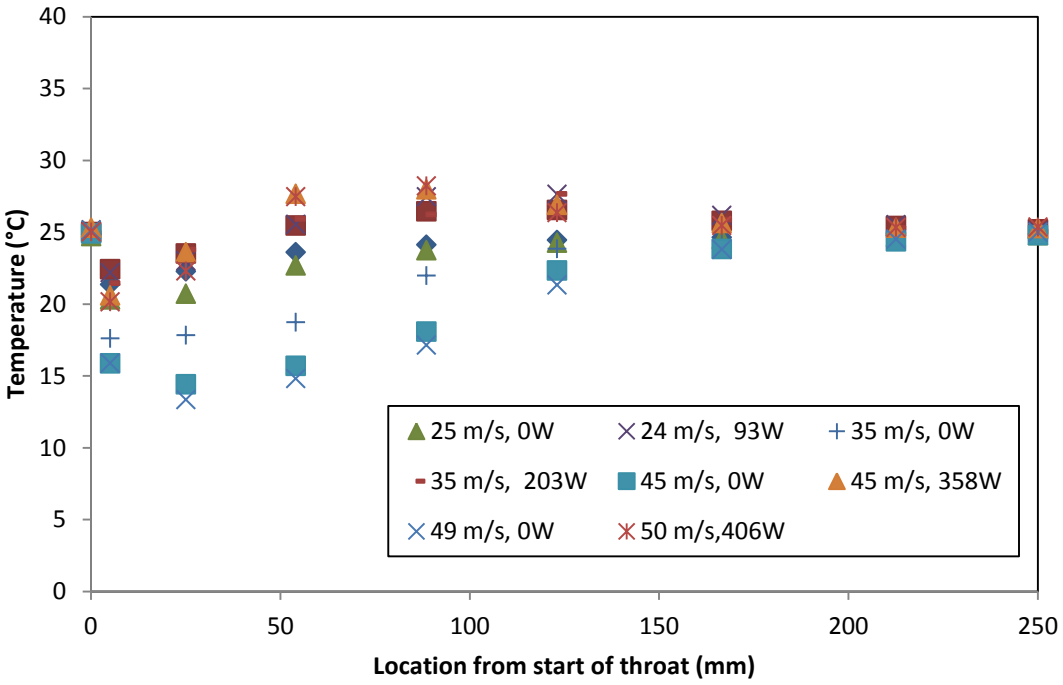

Figure 5.7 Temperature profile of Test Section-3

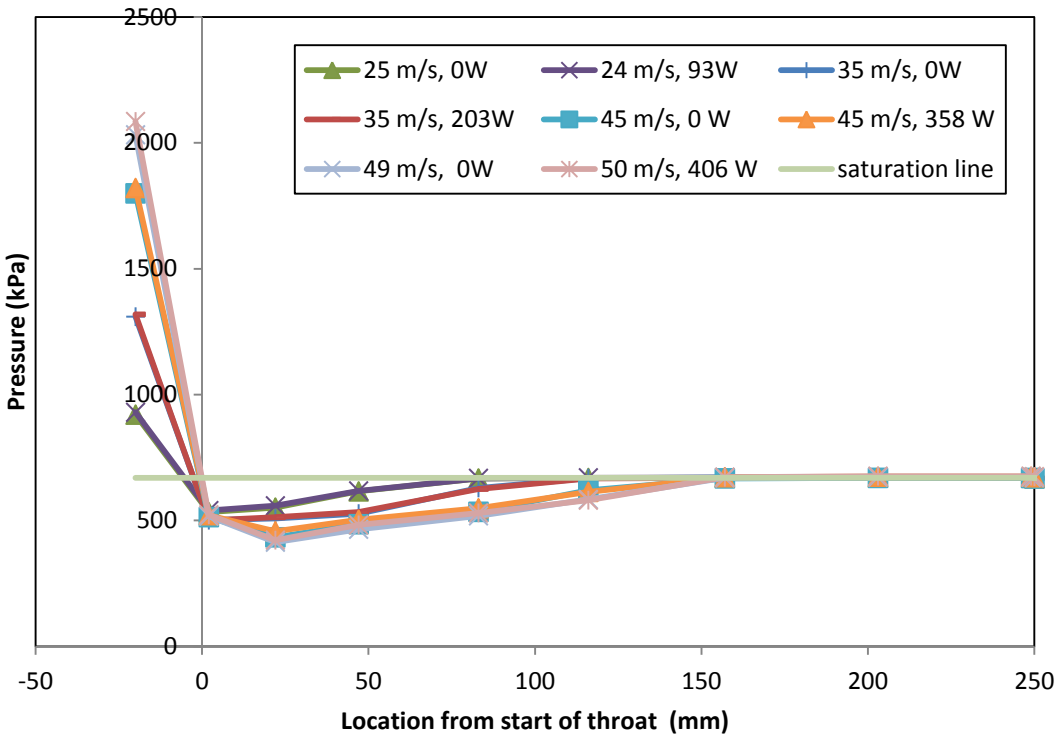

Figure 5.8 Pressure profile of Test Section-3

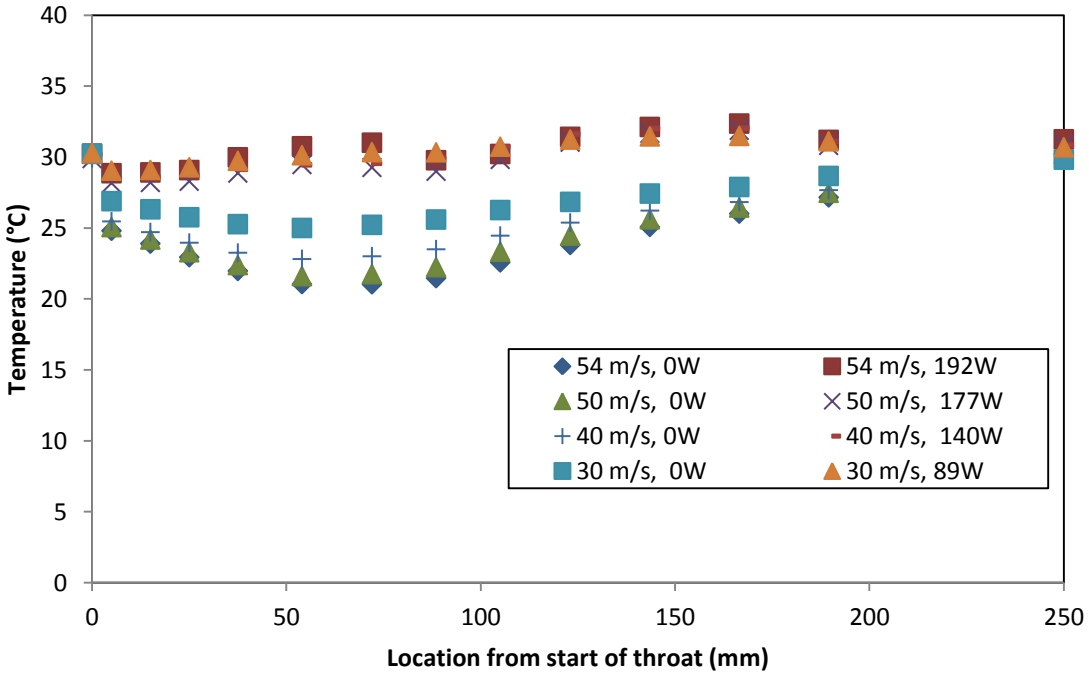

Figure 5.9 Temperature profile of Test Section-4

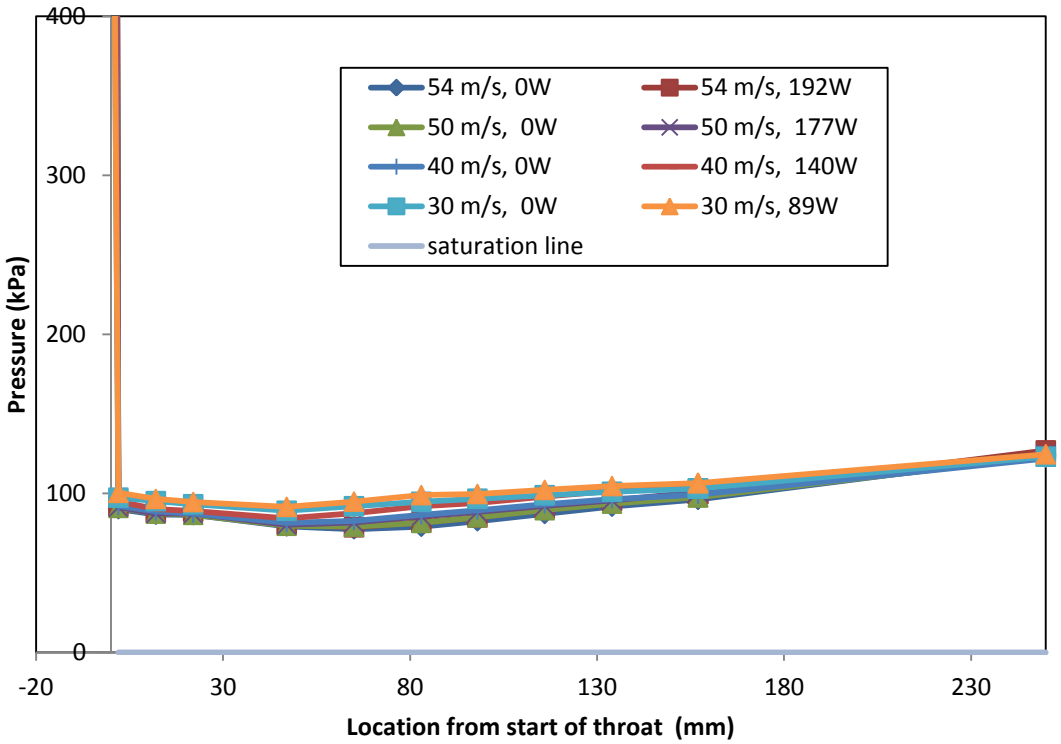

Figure 5.10 Pressure profile of Test Section-4

5.3Conclusion

This chapter presented the temperature and pressure profiles of 4 different test sections. These temperature and pressures directly measured from the instruments that are placed on the nozzle. The results showed the length of the sonic region in the nozzle and the amount of temperature and pressure drop of the nozzle.

6 Analysis of the sonic nozzles

6.1 Introduction

This chapter presents the analytical results corresponding to all the nozzles (Test Section-1 to Test Section-4). Test Section-1 has a 2.43mm throat and the other test sections have a 1.5 mm throat. The length of the nozzle varies depending on the number of diverging sections assembled together. All the test sections have a 1° growth in the diverging section with respect to the center line of the nozzle. R134a is the working fluid for Test Section-1, Test Section-2 and Test Section-3. R123 is the working fluid for Test Section-4. The heater length for Test Section-1, Test Section-2 and Test Section-4 is 200 mm. The heater length for Test Section-3 is 125 mm.

In the Test Section-1, the fluid inlet temperature is 30 °C, and the backpressure saturation temperature is set to 30 °C. For Test Section-2 and Test Section-3, the inlet temperature of R134a is 25 °C, and the back pressure saturation temperature is set to 25 °C. For Test Section-4, the inlet temperature of R123 is 30 °C, and the back pressure saturation temperature is set to 33 °C. For each test, inlet pressures vary from 730 kPa to 2500 kPa which results in throat velocities from 20 m/s to 55 m/s.

The pressures and temperatures of the fluid as it flows though the converging-diverging nozzle were presented in the previous chapter. The two phase heat transfer coefficients, Mach number, quality and Nusselt number ratio in the nozzle are presented in subsequent sections of the present chapter.

6.2 Comparison between the insulated and solid model heat transfer coefficients

Figure 6.1 to Figure **6.4** show the heat transfer coefficients for the solid model as a function of position along the nozzle axis for Test Section-1 to Test Section-4. These heat transfer coefficients correspond to the heated case of the experiments. The data represents the average heat transfer coefficient over each section of the nozzle and is plotted at the mean distance of that section.

The average heat transfer coefficients decreased along the length of the nozzle. There are no heat transfer coefficients from 0 mm to 35 mm of the Test Section-1 because no measured saturation temperatures were available in this region. In the case of Test Section-1, the initial region (from 35 mm to 150 mm) has the highest heat transfer coefficients due to two phase boiling while the single phase region that occurs further down the tube are much lower. The single-phase heat transfer coefficients are as low as 5000-10000 W/m^2 K. Similarly other test sections have high heat transfer coefficients in the two-phase region. The length of this two-phase region varied in all the test sections.

The heat transfer coefficients of R134a are higher than R123 in the two-phase region (after the throat) of the nozzle. For example, some heat transfer coefficients in Test Section-2 are higher than 80,000 W/m^2 K, but the heat transfer coefficients in Test Section-4 are below 50,000 W/m^2 K.

The heat transfer coefficients are very high in the first 50 mm after the throat of the nozzles, and the values near the throat had large variations. It is very difficult to determine the cause for the variations in two-phase heat transfer coefficients immediately after the throat. One possible reason for the variation in heat transfer coefficients might be the large uncertainty (40

%) in the lower temperature drop data points. The high heat transfer coefficients are due to the combined effect of nucleate boiling and convective boiling which combine to form the overall two-phase heat transfer coefficient.

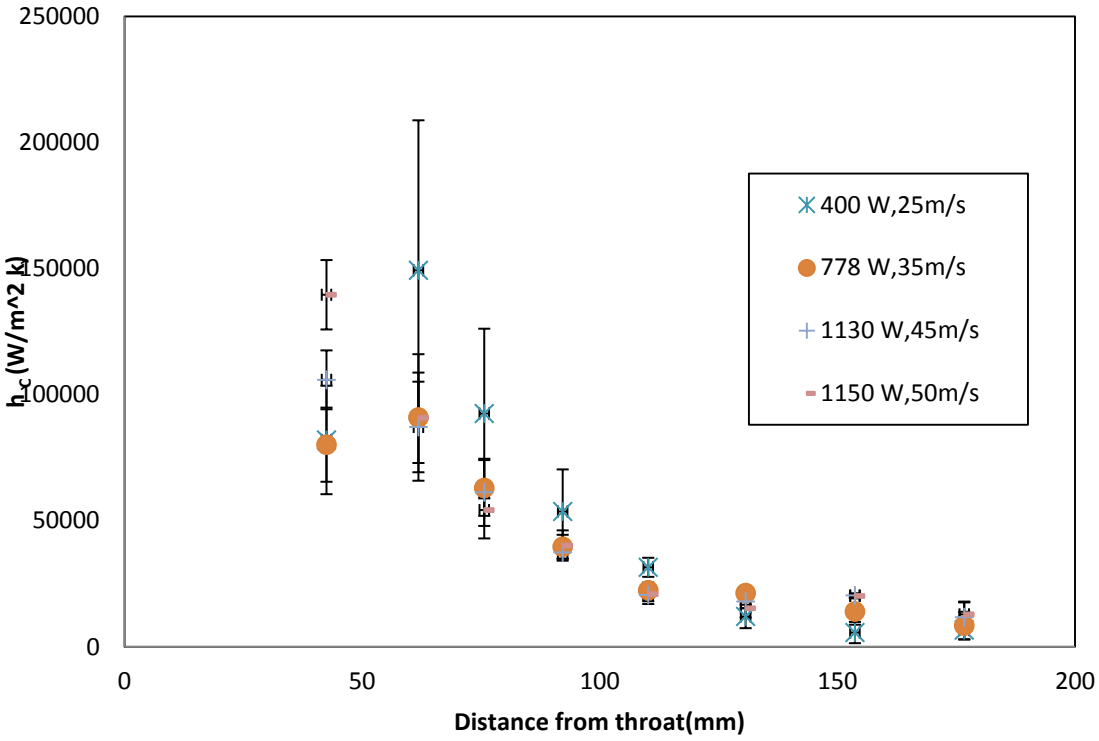

Figure 6.1 Two-phase heat transfer coefficients of Test Section-1

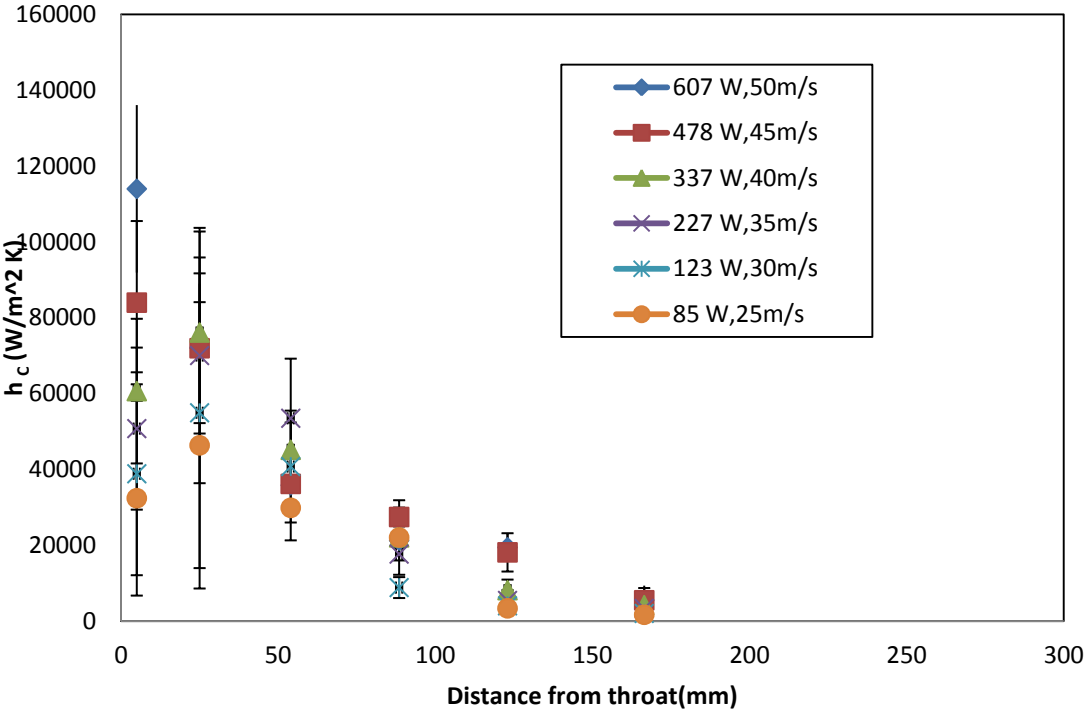

Figure 6.2 Two-phase heat transfer coefficients of Test Section-2

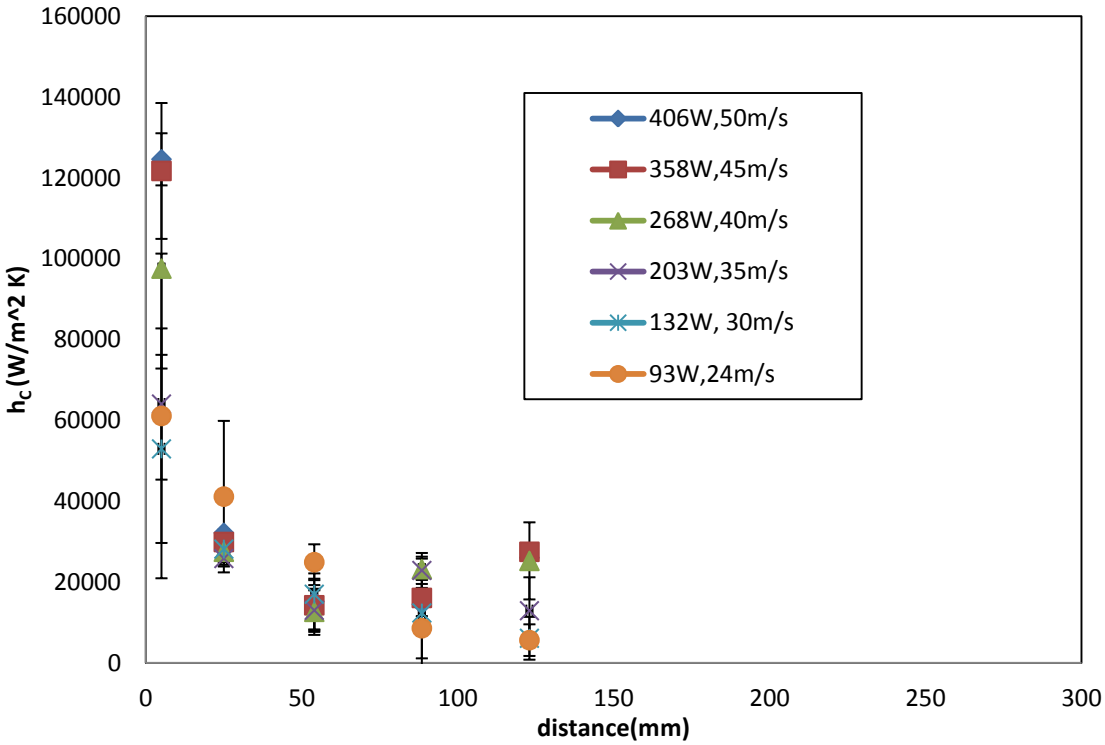

Figure 6.3 Two-phase heat transfer coefficients of Test Section-3

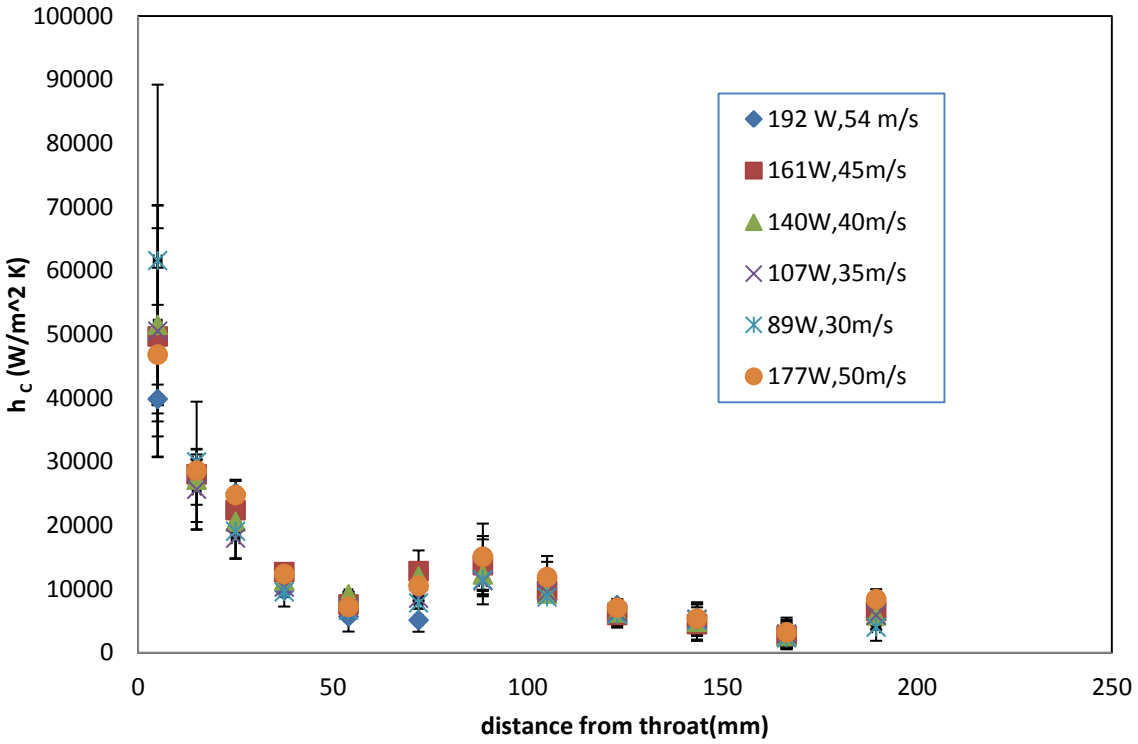

Figure 6.4 Two-phase heat transfer coefficients of Test Section-4

Figure 6.5 to Figure 6.8 present the comparison heat transfer coefficients calculated from the insulated and solid model. The heat transfer coefficients from the two models are nearly identical except at higher heat transfer coefficients. These higher heat transfer coefficient values occur in the first 50 mm of the nozzle. The uncertainty bars shown on the figure encompasses calculations form both methods.

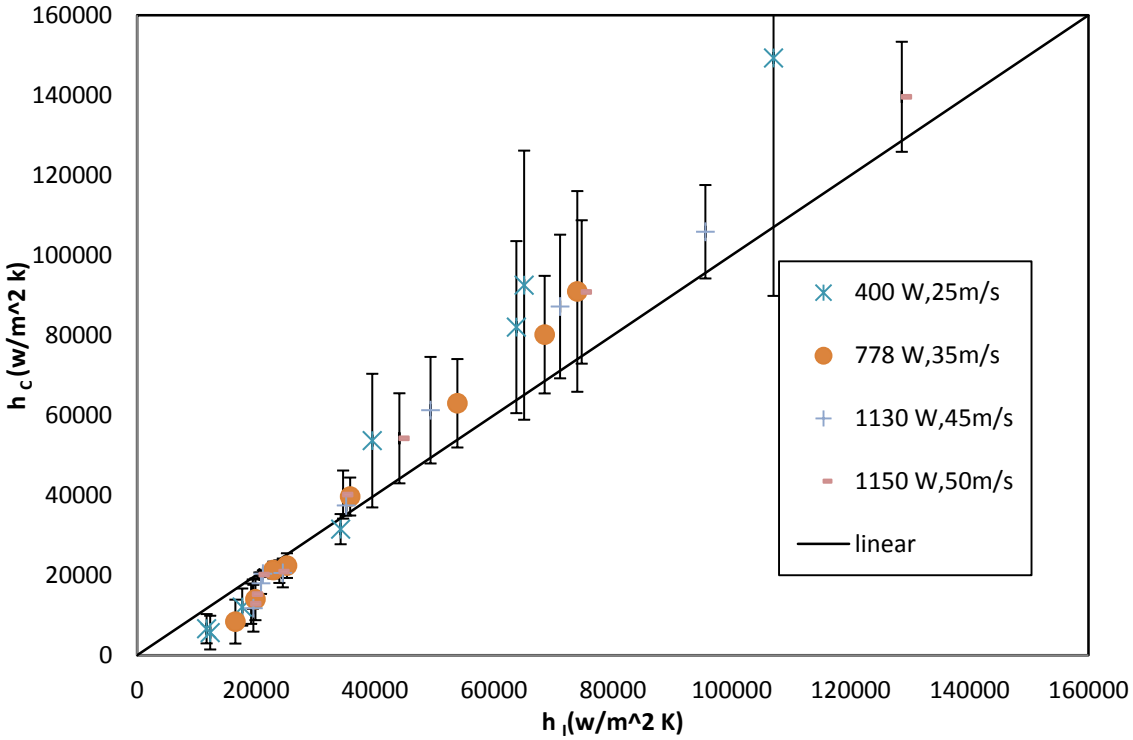

Figure 6.5 Comparison between the insulated and solid model (Test Section-1)

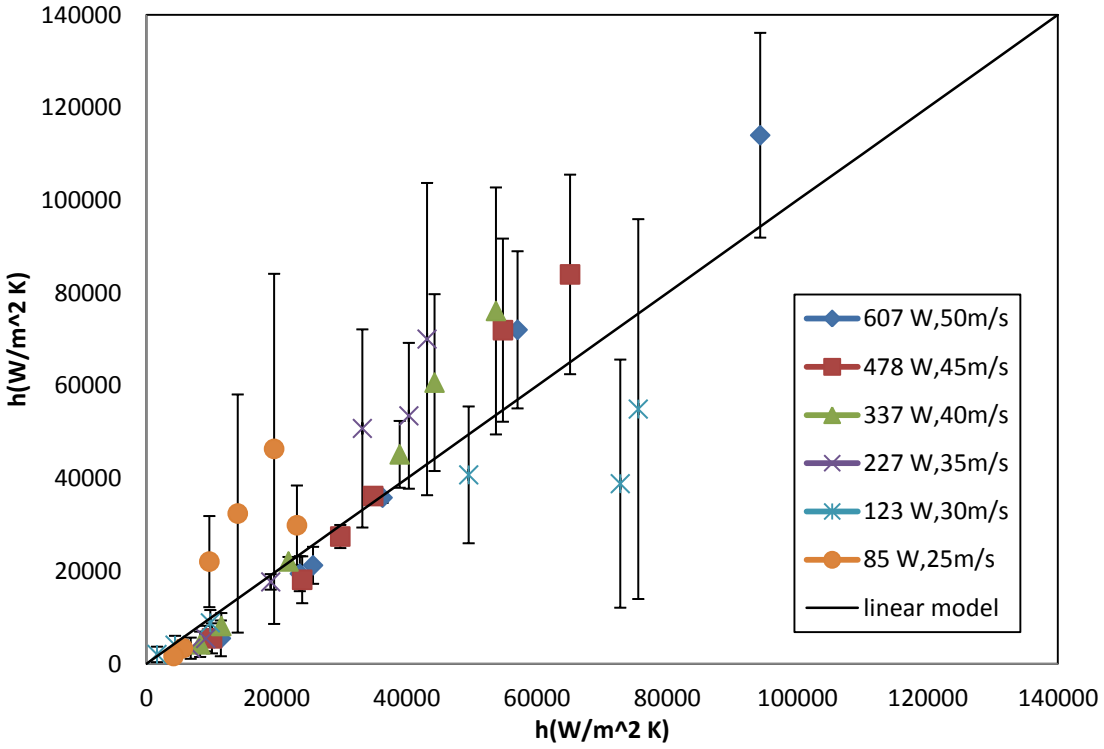

Figure 6.6 Comparison between the insulated and solid model (Test Section-2)

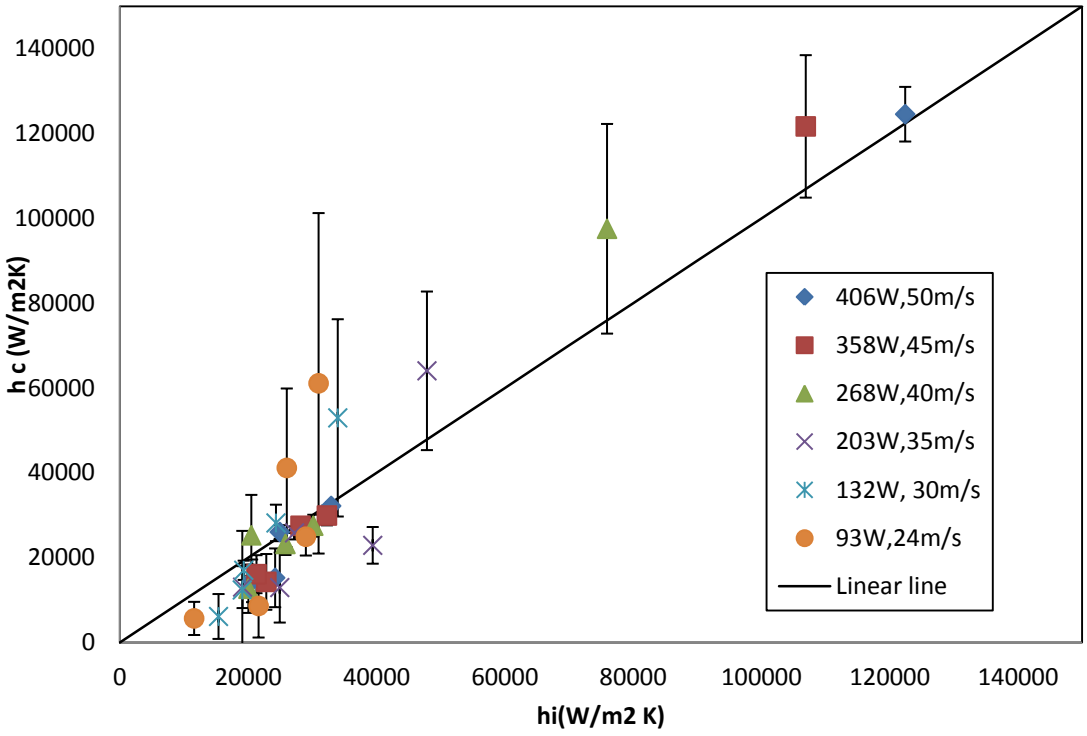

Figure 6.7 comparison between the insulated and solid model (Test Section-3)

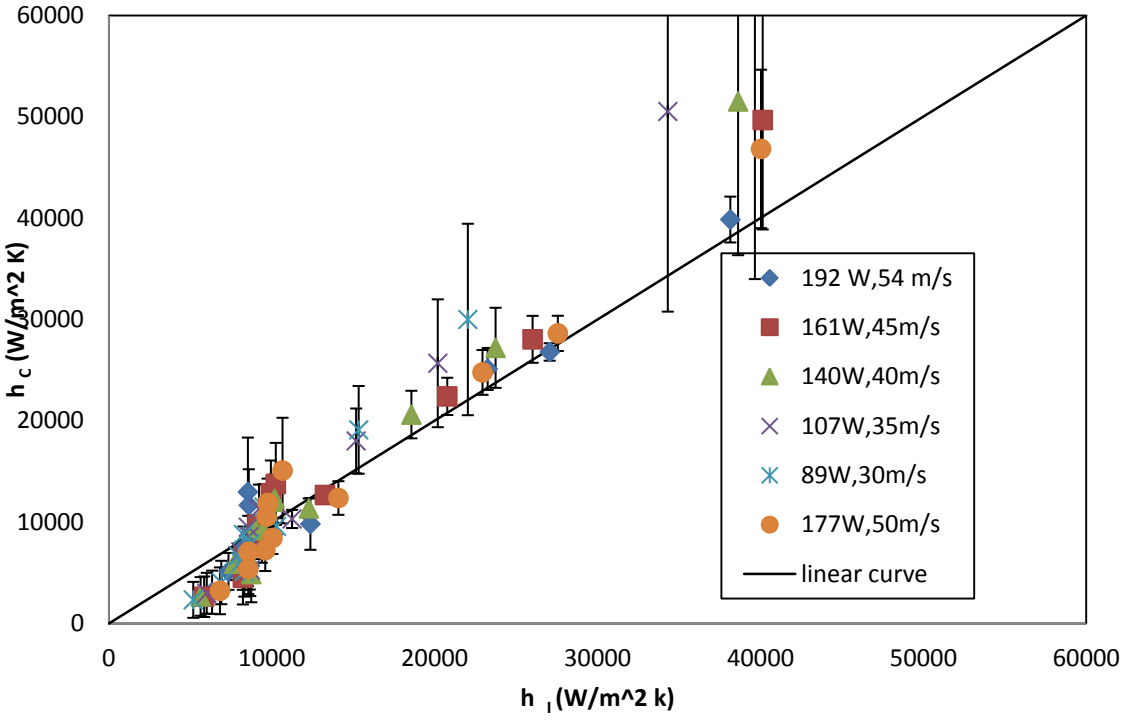

Figure 6.8 Comparison between insulated and solid model (Test Section-4)

6.3Effect of heat flux

Figure **6.9** to Figure **6.12** show the heat transfer coefficients for the solid model as a function of heat flux along the nozzle for Test Section-1 to Test Section-4. The data represents the average heat transfer coefficient over each section of the nozzle and is plotted at the average heat flux of that section.

The average heat transfer coefficients are strongly correlated to the average heat fluxes along the nozzle. The high heat fluxes at the entry portion of the nozzle are due to the small wetted surface area. In the R134a test sections, the heat transfer coefficients over 35000 W/m^2 K are in the sonic multiphase region with heat transfer coefficients rising exponentially as heat flux increases. In all the test sections, the high velocity data points (40 m/s to 54 m/s) are consistent due to small (<20 %) measurement uncertainty.

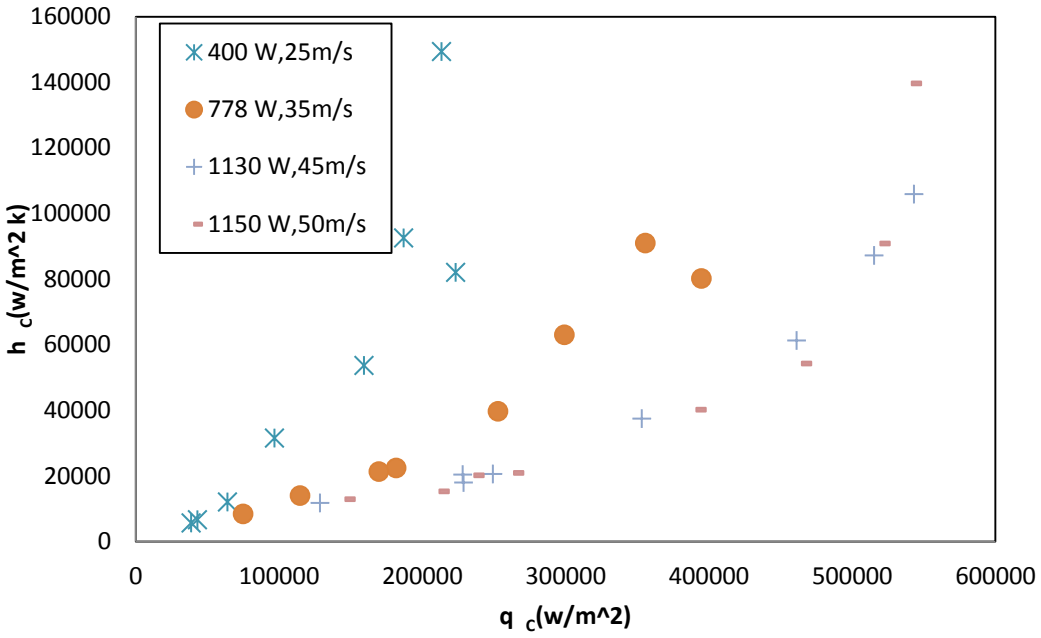

Figure 6.9 Heat flux vs. Heat transfer coefficients of Test Section-1

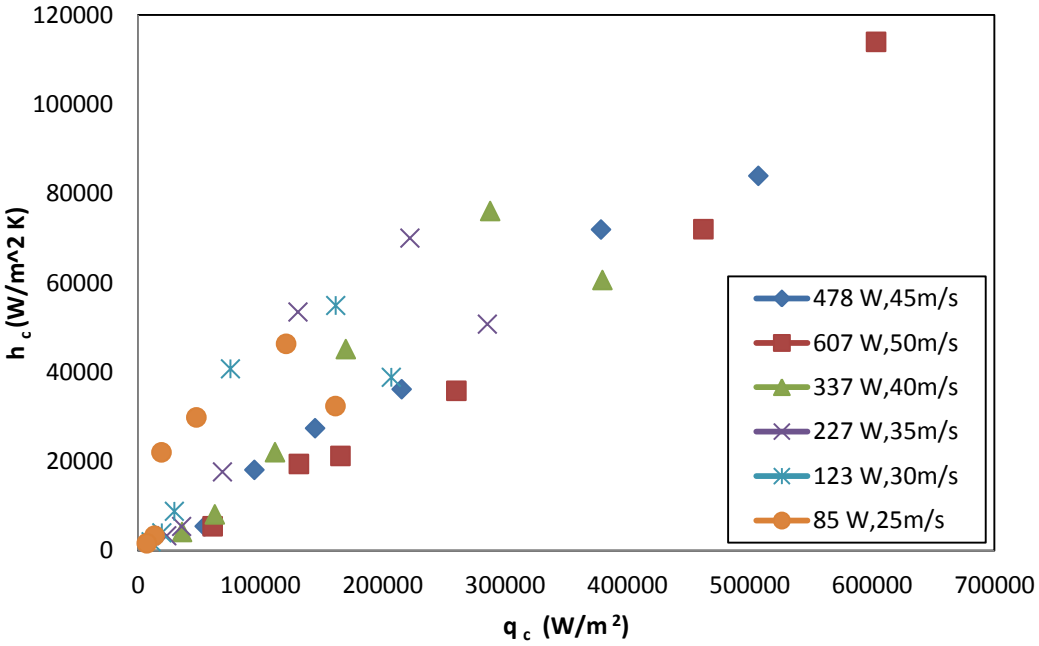

Figure 6.10 Heat flux vs. Heat transfer coefficients of Test Section-2

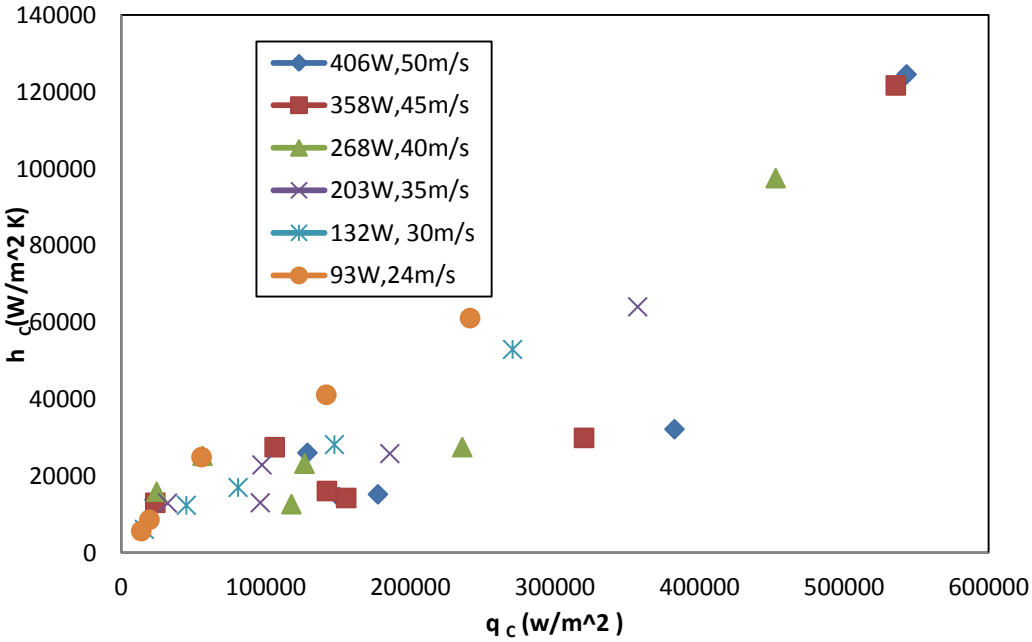

Figure 6.11 Heat flux vs. Heat transfer coefficients of Test Section-3

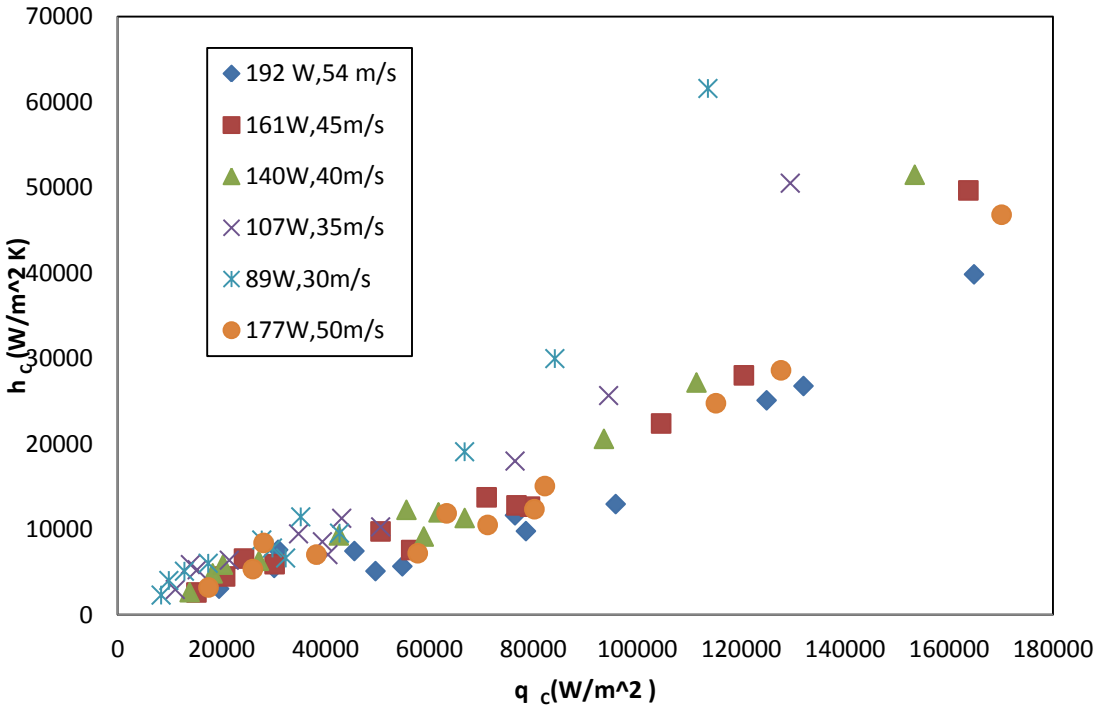

Figure 6.12 Heat flux vs. Heat transfer coefficients of Test Section-4

6.4 Mass fluxes in sonic nozzle

The following plots from Figure **6.13** to Figure **6.16** show the relationship between mass flux and the solid model heat transfer coefficients in all the test sections. The mass fluxes are very high due to the geometry of the nozzle. The plot reads from right to left since the high mass fluxes correspond to the throat, and the mass fluxes decrease along the nozzle. In all the test sections, the heat transfer coefficient increases with increasing mass flux. The high heat transfer coefficients in all the test sections at the lower mass flux and lower velocity data points are hard to interpret due to high uncertainty

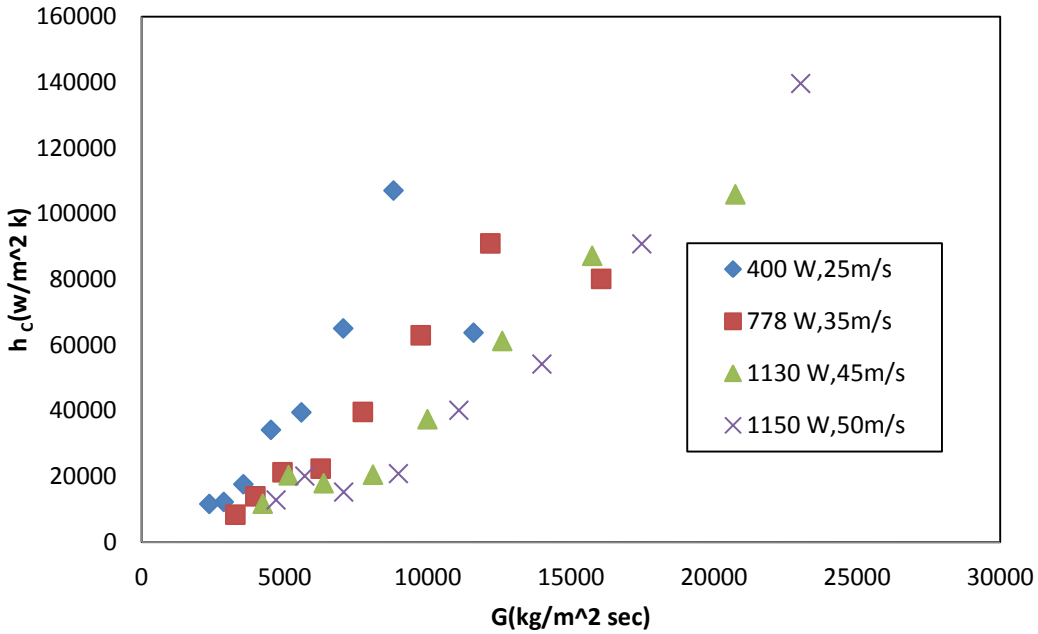

Figure 6.13 Mass flux vs. Heat transfer coefficients of Test Section-1

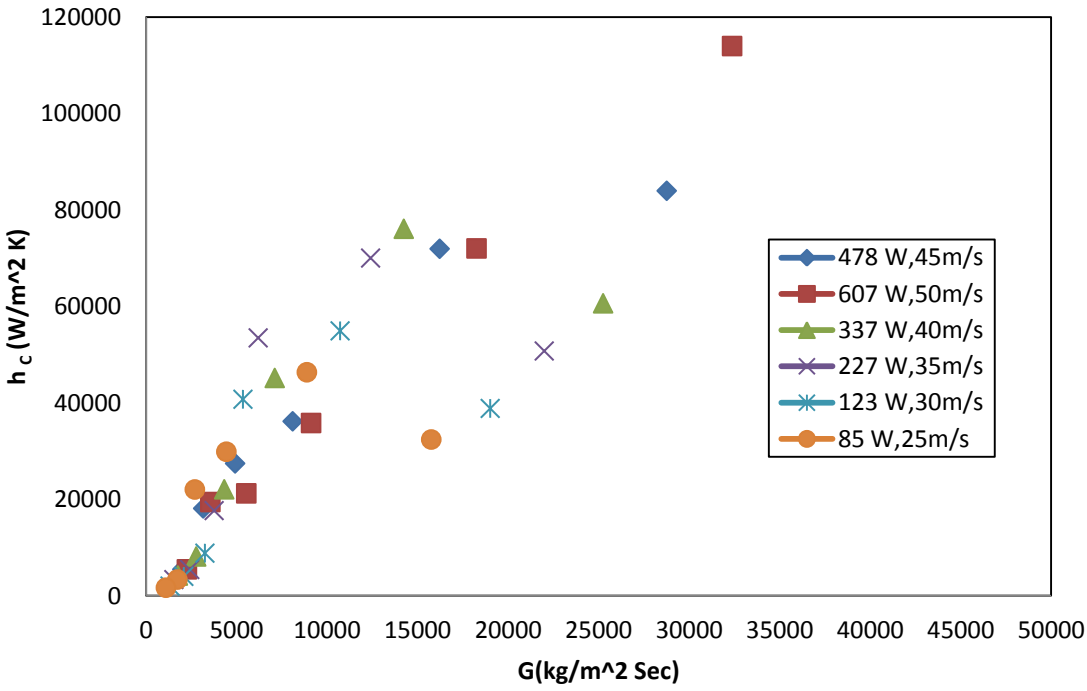

Figure 6.14 Mass flux vs. Heat transfer coefficients of Test Section-2

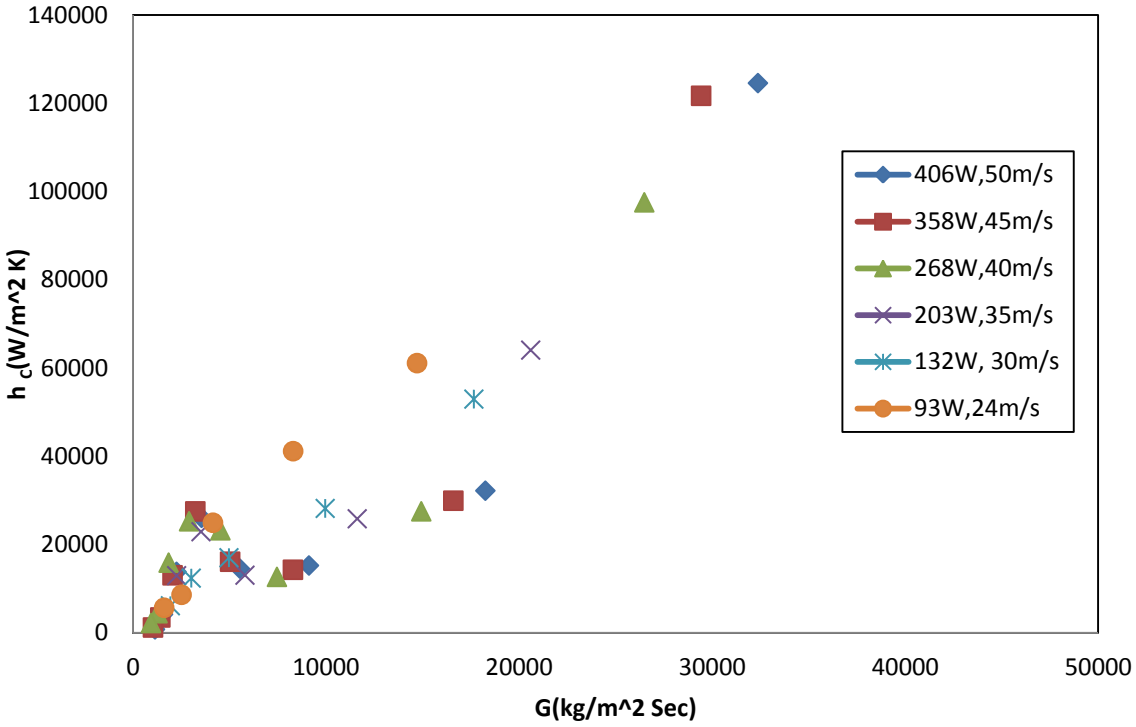

Figure 6.15 Mass flux vs. Heat transfer coefficients of Test Section-3

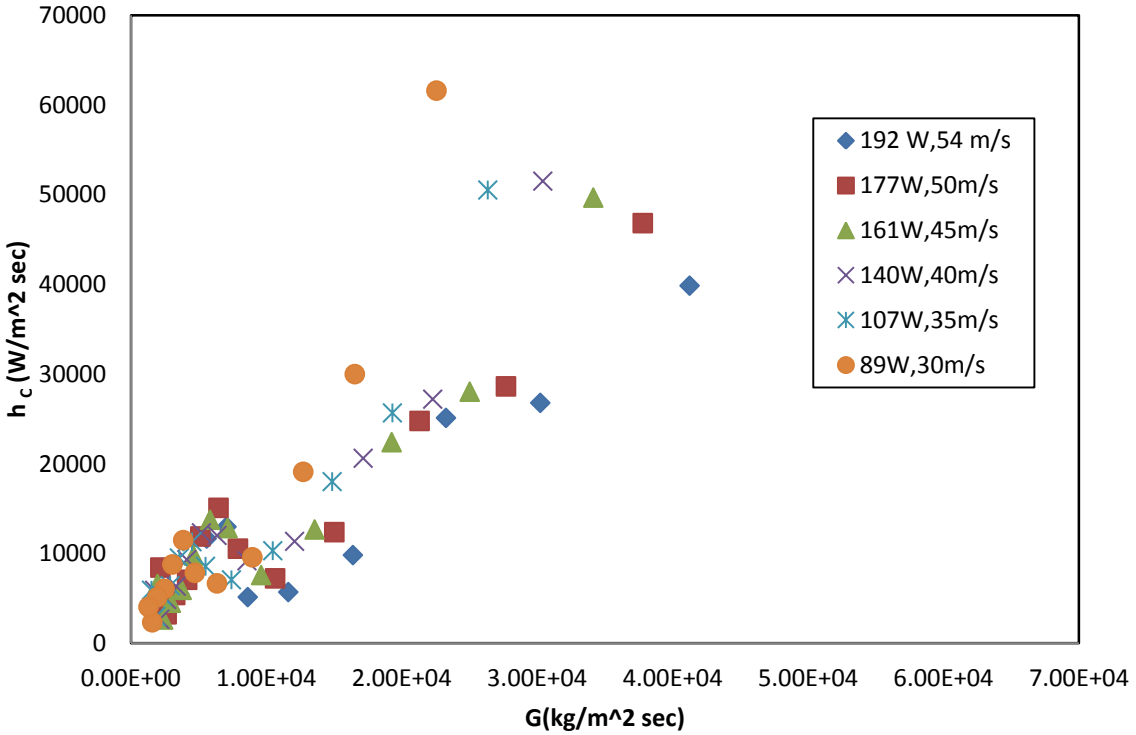

Figure 6.16 Mass flux vs. Heat transfer coefficients of Test Section-4

6.5 Nusselt ratios (Φ) along the nozzle

Figure 6.17 to Figure **6.20** present the Nusselt number ratios (Φ) along the nozzle. The ratio of the Nusselt number represents the ratio of experimental two-phase Nusselt number to the single phase liquid Nusselt number.

Nusselt ratios are greater than one due to the presence of two-phase flow in the nozzle. It is interesting to note that the maximum ratio is achieved at the lowest temperature point in all of the nozzles. For example, for Test Section-2, the Nusselt number ratios gradually increased up to 50 mm from the throat where the temperature dropped to a lowest point and then decreased towards the end of the nozzle. The higher velocity data points (35 m/s to 50 m/s) show a consistent trend likely because of lower experimental uncertainty (8 % to 20 %), but at the lower velocities (20 m/s to 30 m/s) the ratios are inconsistent and tend to have uncertainties that range as high as 40 %. The single phase region at the end of the nozzles has ratios close to one indicating single-phase liquid.

The trend of the Nusselt number ratios of R123 is completely different from the R134a nozzle. Initially the Nusselt ratios in the R123 nozzle decreases till 50 mm from the throat. It then increases from 50 mm to 100 mm of the nozzle, and finally decreases towards the end of the nozzle. The trend in the Nusselt number ratio of R123 is exactly similar to the heat transfer coefficient curve along the nozzle.

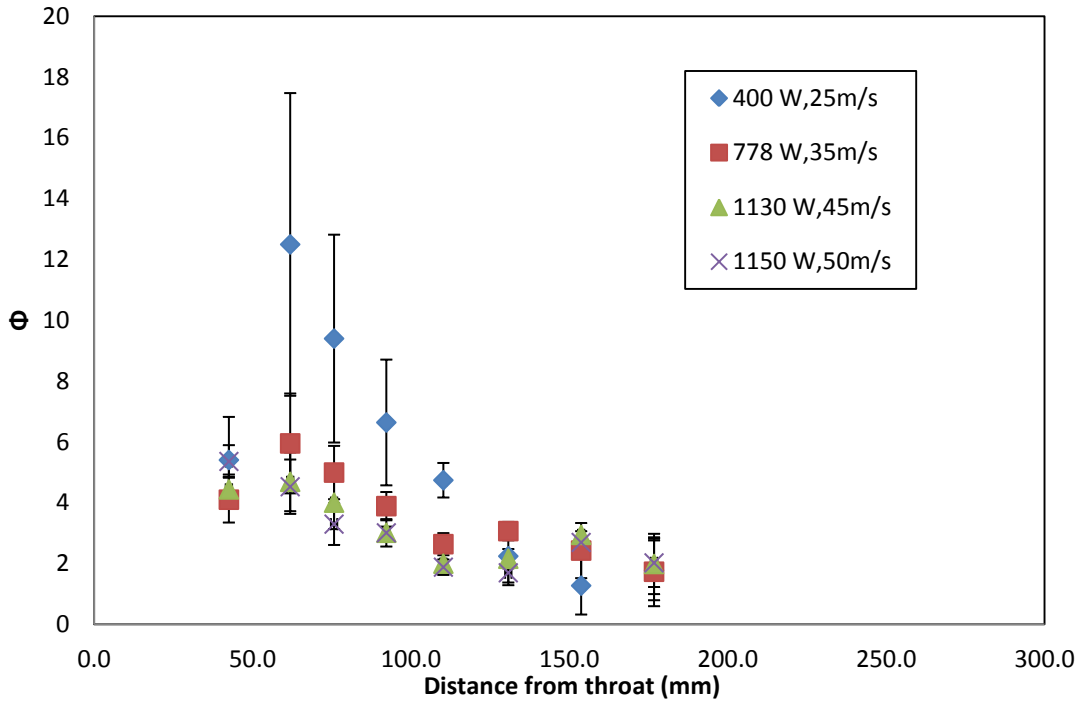

Figure 6.17 Nusselt number ratio (Φ) of the Test Section-1

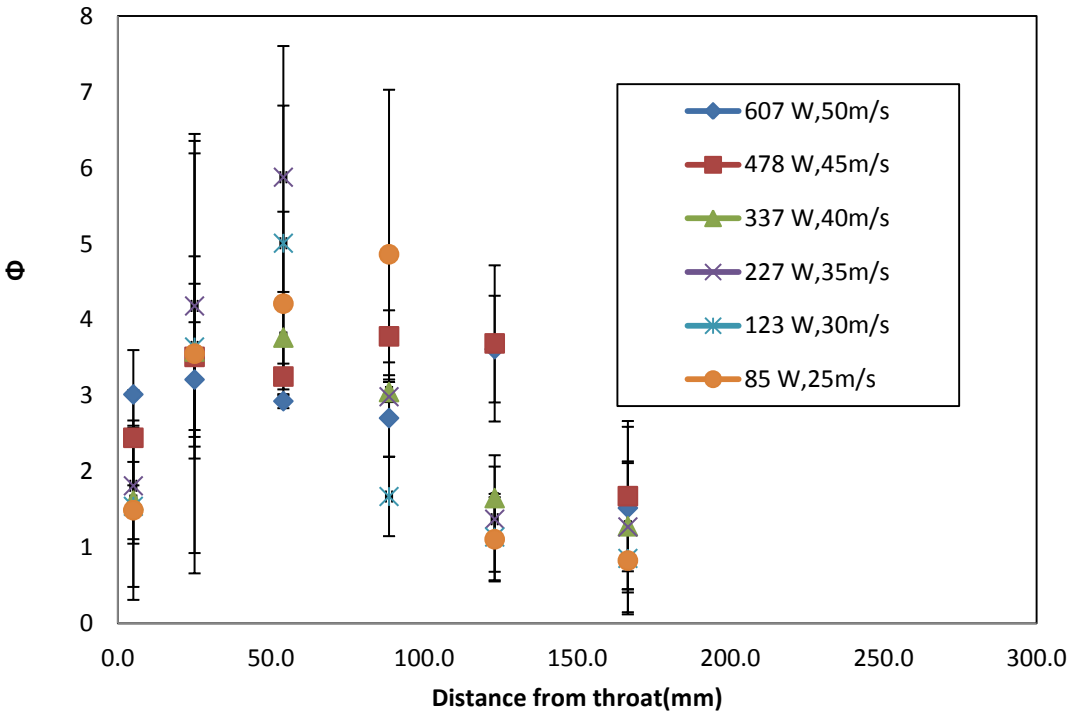

Figure 6.18 Nusselt number ratio (Φ) of the Test Section-2

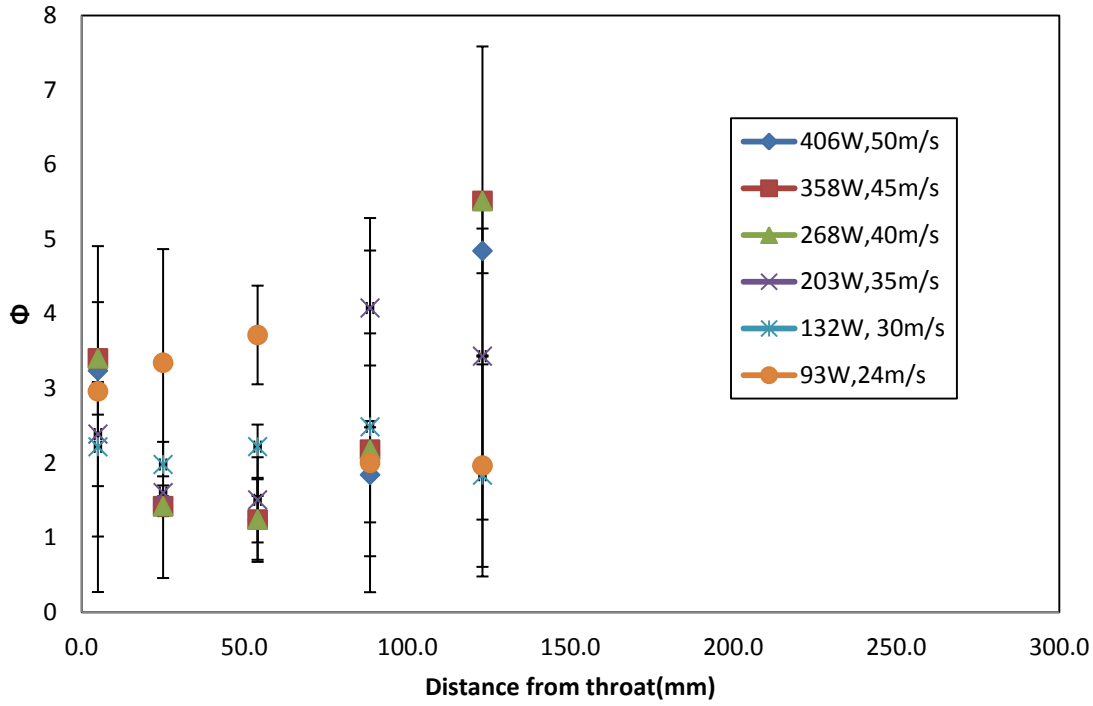

Figure 6.19 Nusselt number ratios (Φ) of the Test Section-3

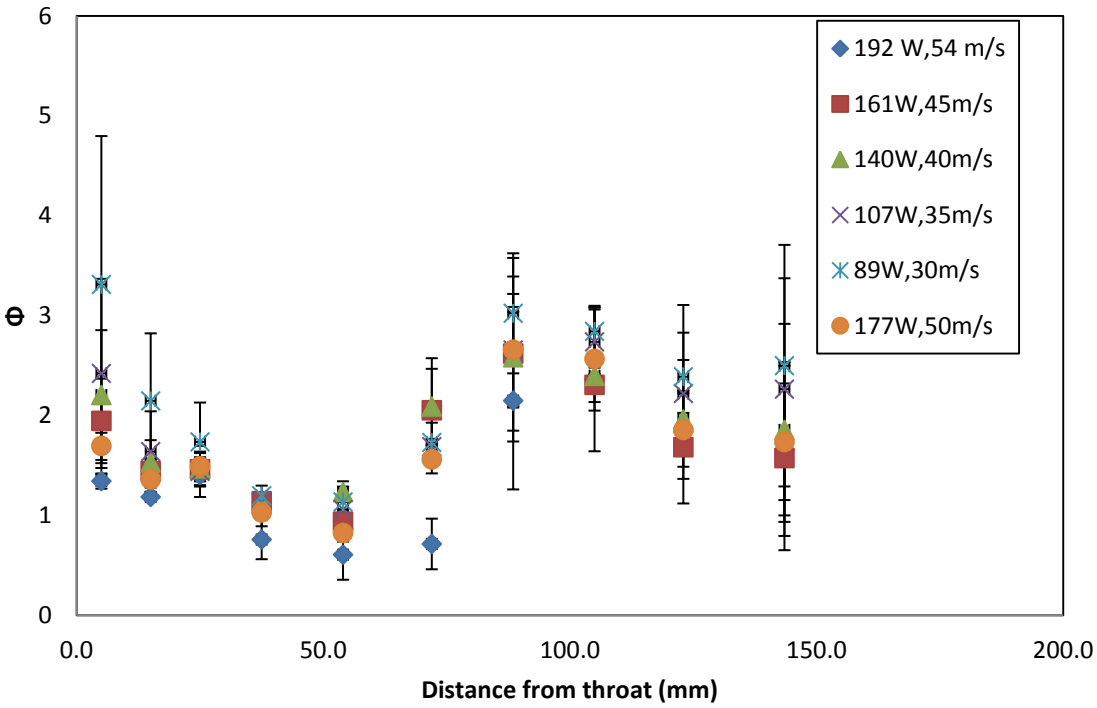

Figure 6.20 Nusselt number ratio (Φ) of the Test Section-4

6.6 Quality and Mach number along the nozzle

The plots from Figure **6.21** to Figure **6.28** present the Mach numbers (M) and qualities (x) along the length of the nozzle for all test sections. Initially the Mach numbers are greater than one, indicating the flow is sonic. Mach numbers gradually decrease to very small numbers along the length of the nozzle. The length of the sonic region increases as the throat velocity increases in the nozzle. For example, in the case of 45 m/s and 50 m/s of the Test Section-1, sonic flow occurs in the first 100 mm of the nozzle. It is interesting to note that this is also where the temperature drops to the lowest point. For the same Test Section-1, there is no sonic flow for the 25 m/s data point.

The Mach number profile can be compared with the temperature profile. For example, the 50 m/s case (Test Section-2), the wall temperature profile showed that the temperatures in the nozzle dropped till 37 mm from the throat of the nozzle, later they increased down the tube. Similarly the Mach numbers are greater than one (sonic) for the first 37 mm from throat, later they dropped below one. It follows that the wall temperatures continue to drop when there is sonic multiphase flow in the nozzle. Once the nozzle is no longer in sonic flow, the wall temperatures in the nozzle start to increase.

The quality also increases with the temperature drop in the nozzle. The maximum quality (x) occurs at the lowest temperature position in the nozzle. In the case of Test Section-1, the maximum quality is around 12 % at 75 mm for the 50 m/s data run, while at 25 m/s the quality only reaches 7 %. Similarly the maximum quality (11%) occurs at 37 mm from the throat of the Test Section-2 (at 50 m/s), while at 25 m/s the quality reaches 6 %.

Test Section-4 has higher Mach numbers than other test sections, and most of the data points are in the sonic region even with the lower velocity data points. The flow qualities achieved in Test Section-4 were less than other nozzles.

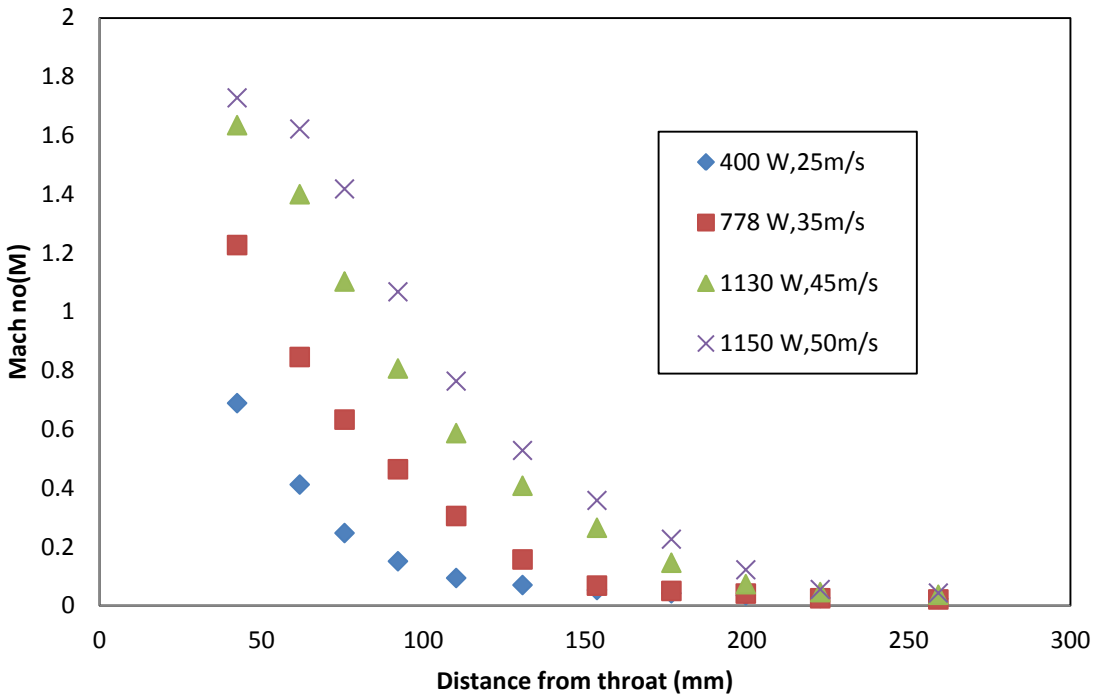

Figure 6.21 Mach number (M) values of the Test Section-1

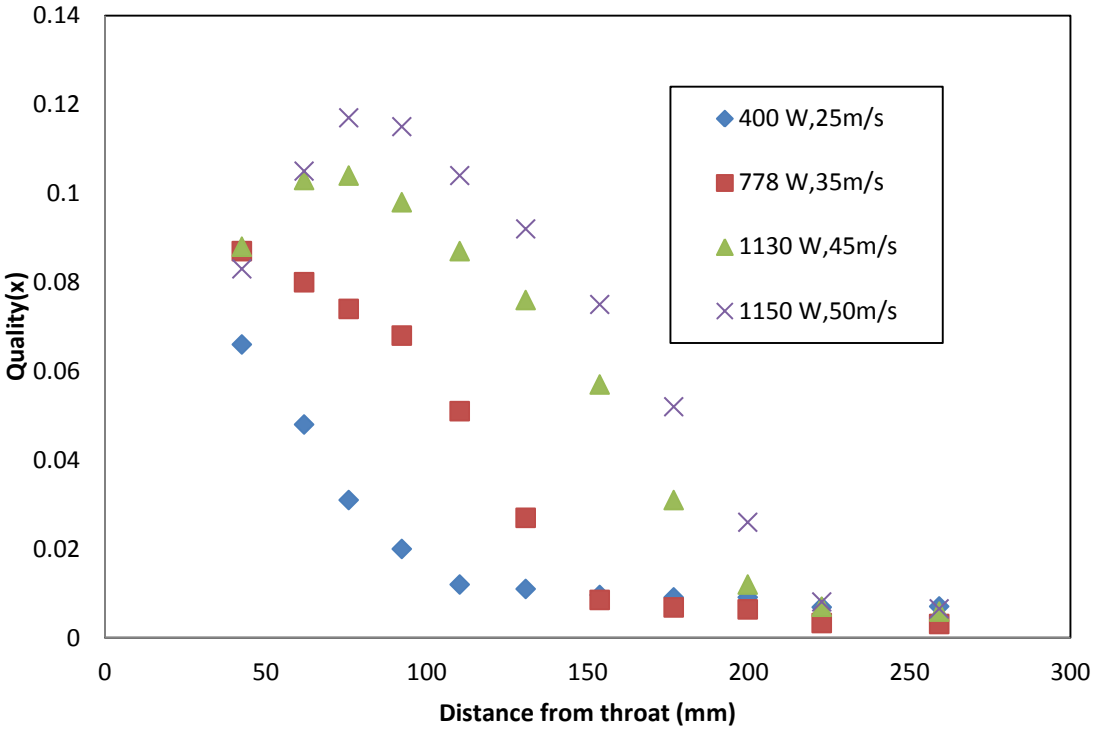

Figure 6.22 Flow qualities (x) of the Test Section-1

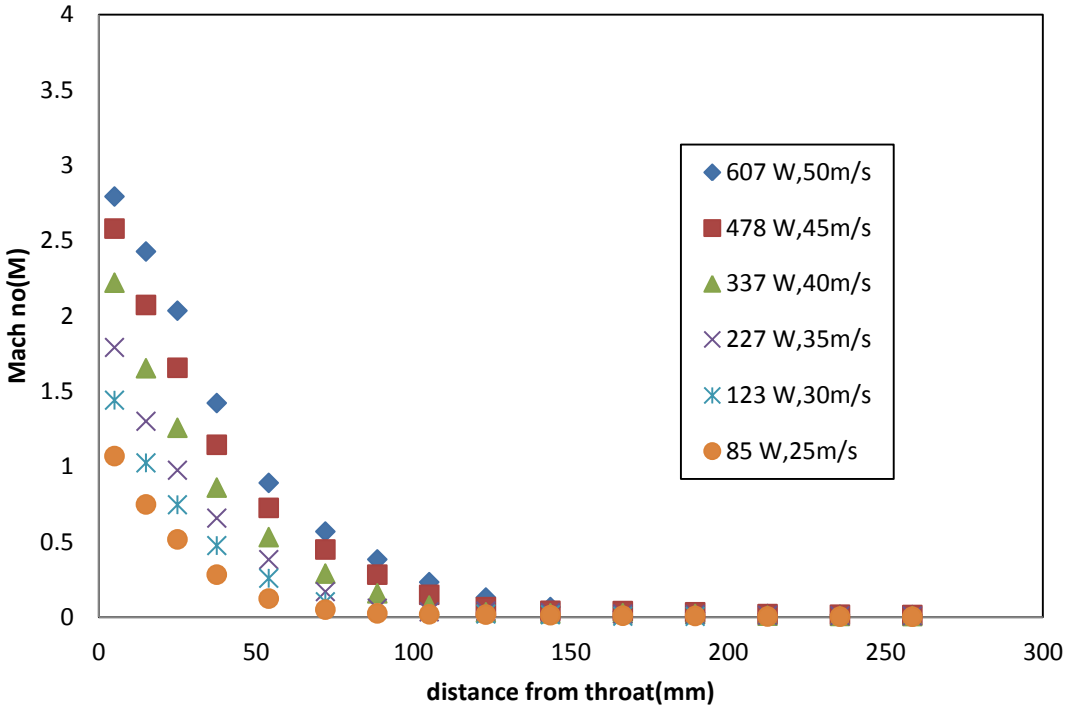

Figure 6.23 Mach number (M) of the Test Section-2

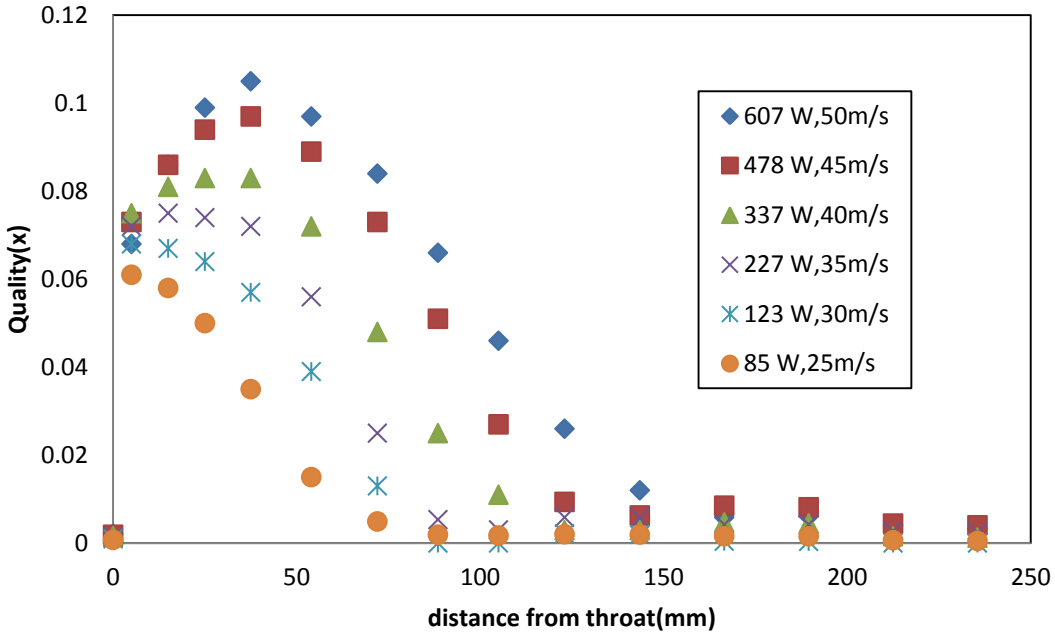

Figure 6.24 Flow qualities (x) of the Test Section-2

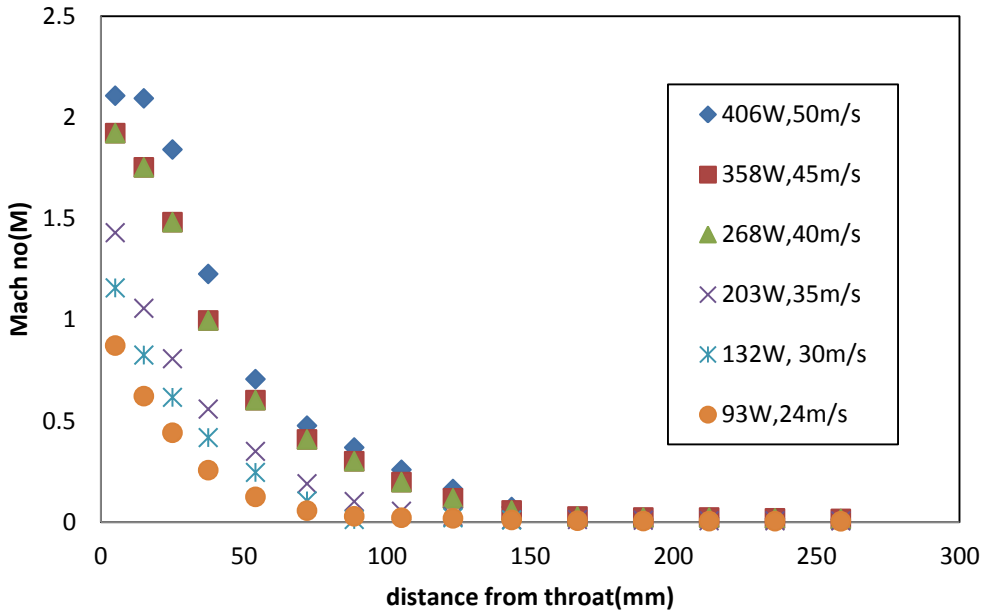

Figure 6.25 Mach number (M) values of the Test Section-3

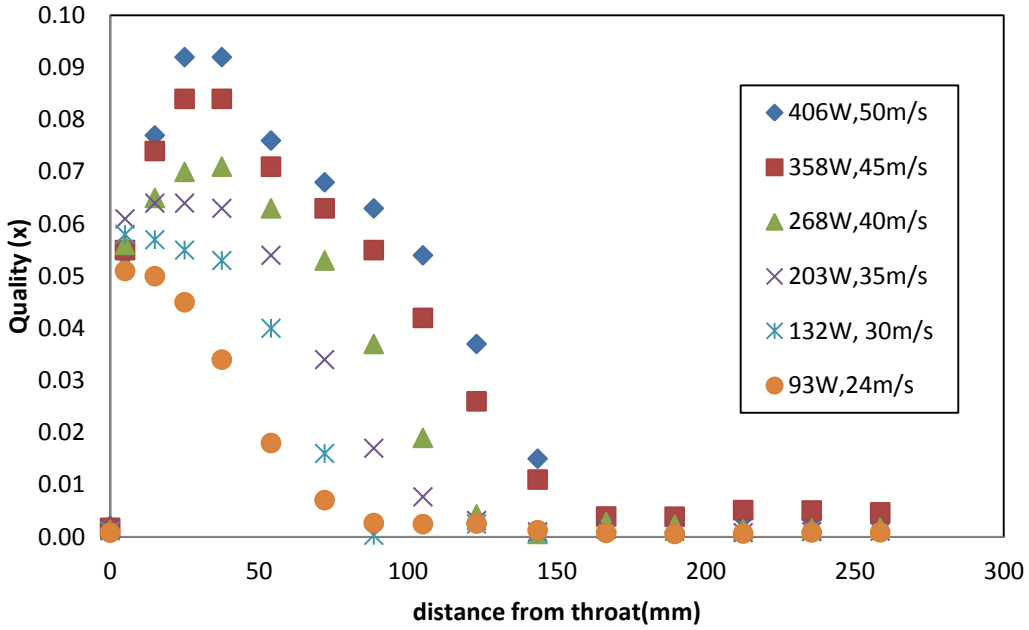

Figure 6.26 Flow qualities (x) of the Test Section-3

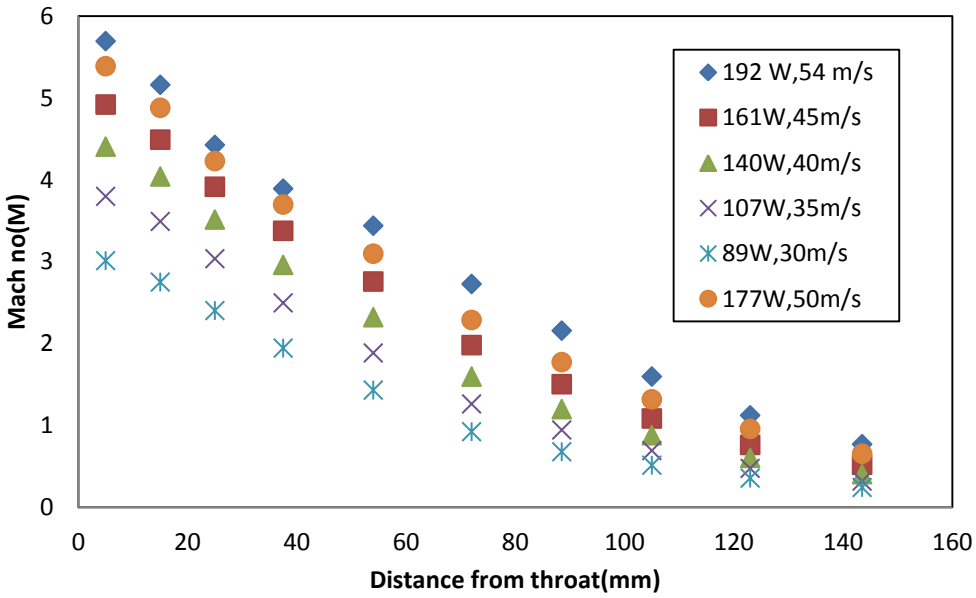

Figure 6.27 Mach number (M) values of the Test Section-4

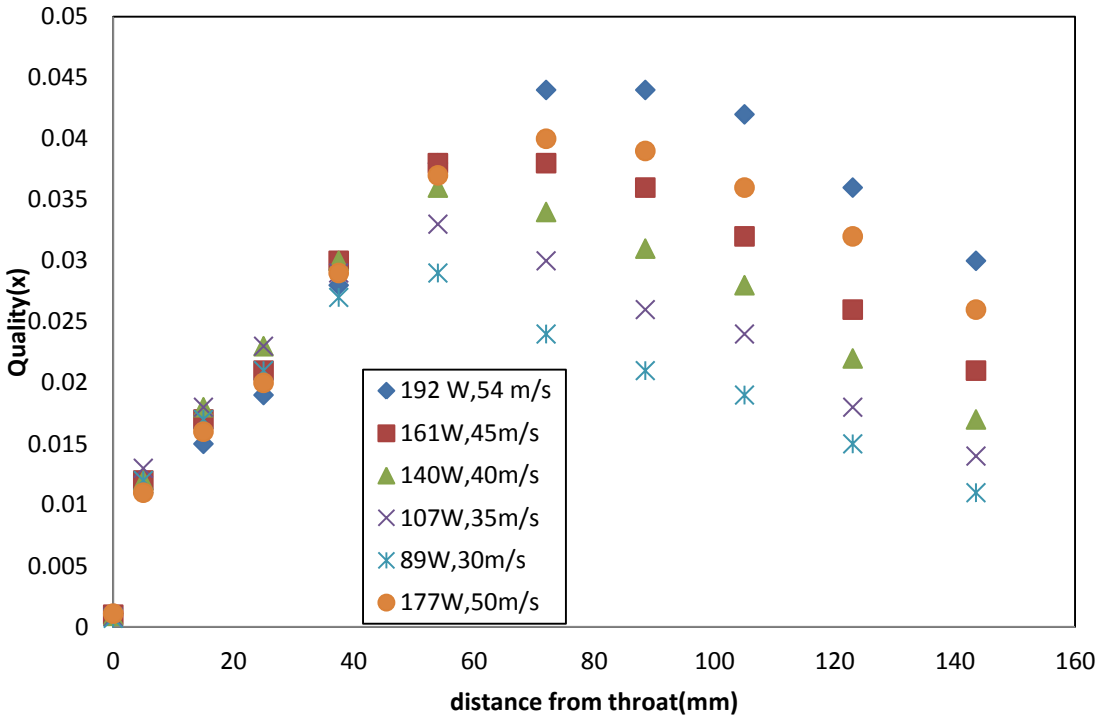

Figure 6.28 Flow quality (x) values of the Test Section-4

6.7 Effect of Quality and Nu ratio on Mach number

Figure **6.29** through Figure **6.32** show the relationship between the quality and Mach numbers in all test sections. These plots should read from right to left, since high Mach numbers correspond to the throat and Mach numbers decrease along the nozzle. The flow qualities decreased as the Mach numbers were decreasing in the nozzle with R134a as a working fluid, but this is only in the subsonic region of the nozzle. The test sections which had R134a as a working fluid have a large subsonic region compared with the sonic region, and in the subsonic region, the qualities are smaller than those in the sonic region. For the lower velocity run 25 m/s of Test Section-1, Test Section-2 and Test Section-3, all data points in the nozzles are in the subsonic two-phase region.

Test Section-4 has higher Mach numbers than other Test Sections for low qualities. The Test Section-4 has a long sonic region, and all the data points are in the sonic region. This is because R123 has different properties than R134a.

Figure **6.33** through Figure **6.36** show the relationship between the Nusselt number ratio (Φ) and the Mach number (M). Nusselt ratios were above one due to the presence of a two-phase flow in the nozzle. Nusselt number ratios for R134a were high in the sonic region as compared to the subsonic region. For example, for the Test Section-1, Nusselt number ratio values ranged from three to six in the sonic region. For the Test Section-2, Nusselt ratio values were between two and six. The most important conclusion of this paper is that sonic multiphase flows increase heat transfer coefficients as expected, but this enhancement is limited to six times the single-phase heat transfer coefficients and Subsonic two-phase region has higher uncertainty than sonic region. Traditional subsonic multiphase flows have enhancements that match or exceed this value. Nonetheless, the heat transfer coefficients were still very high for the pipe diameter due to the high Reynolds number.

The Nusselt ratios of R123 (Test Section-4) are low compared to the R134a cases and the trend in the Nusselt ratios are different as well. Nusselt ratios dropped below one at higher mach numbers (3 to 4), but this did not occur in the R134a test sections. However most of the data points in the sonic region had ratios ranging from 1 to 3 similar to the Nusselt ratios in the sonic region of the R134a test sections.

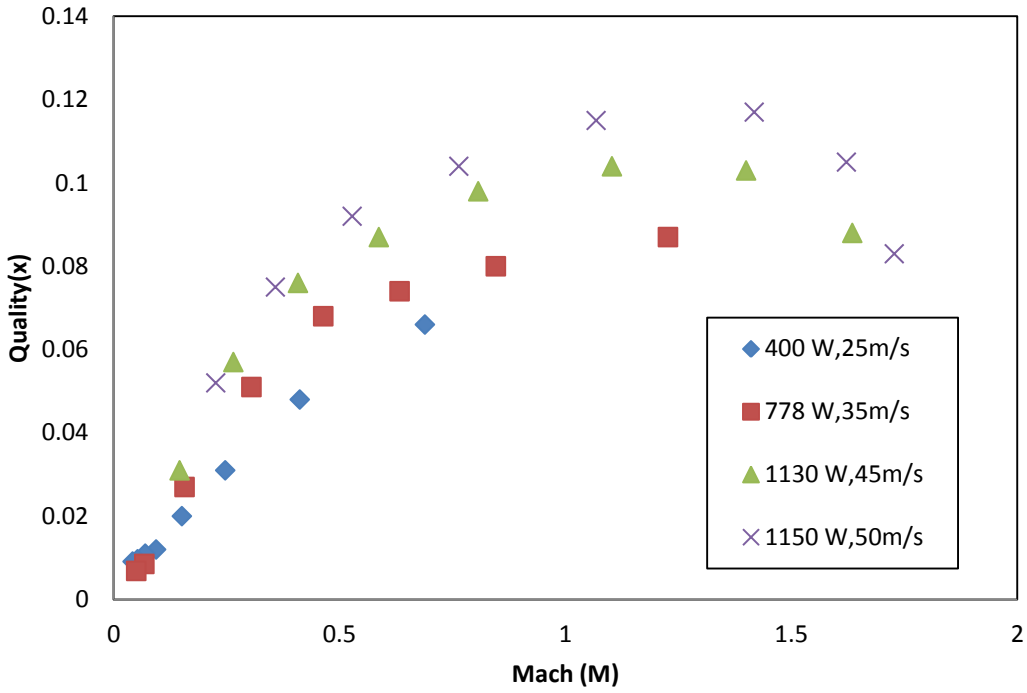

Figure 6.29 Flow quality (x) vs. Mach number (M) of Test Section-1

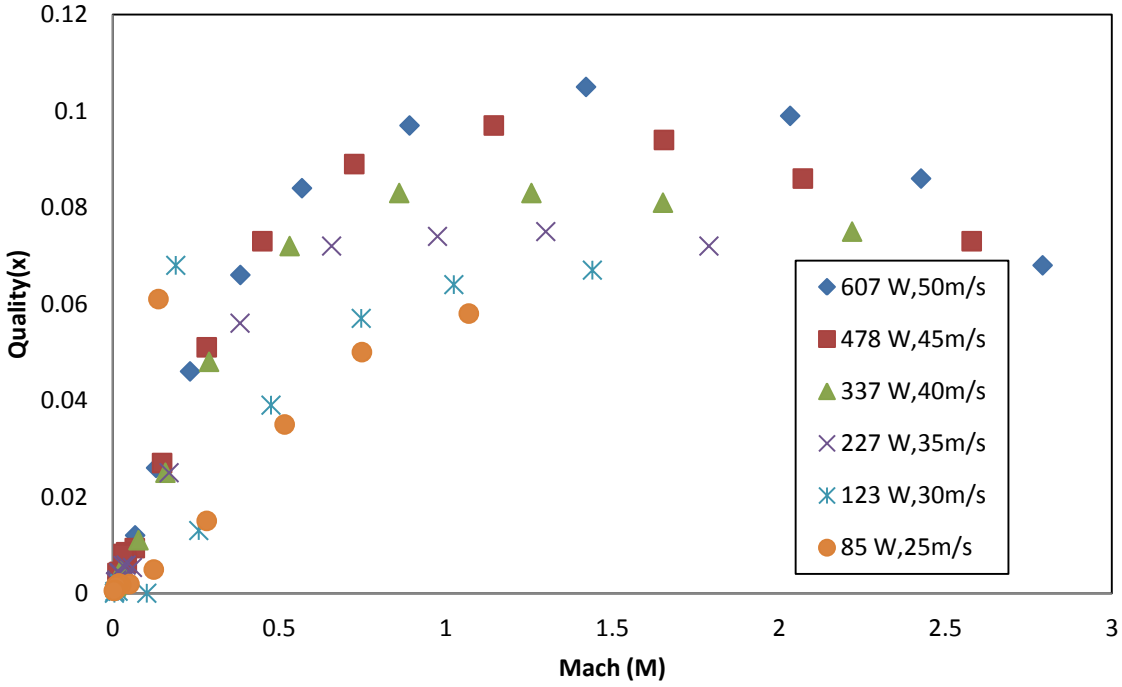

Figure 6.30 Flow qualities (x) vs. Mach number (M) of Test Section-2

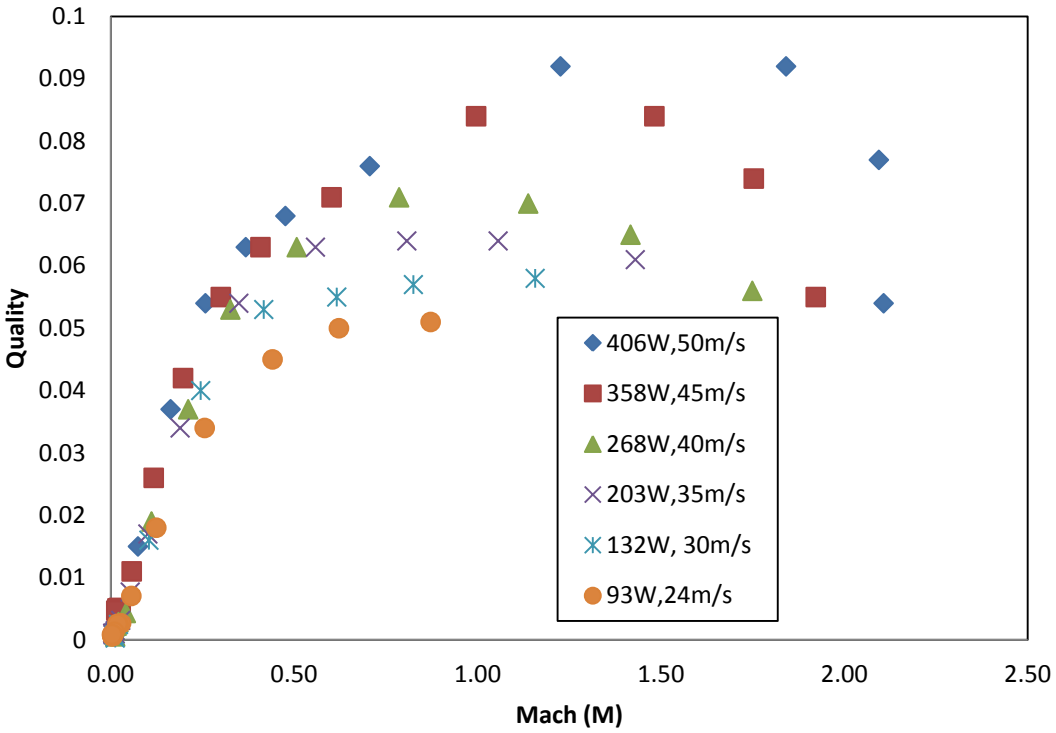

Figure 6.31 Flow quality (x) vs. Mach number (M) of Test Section-3

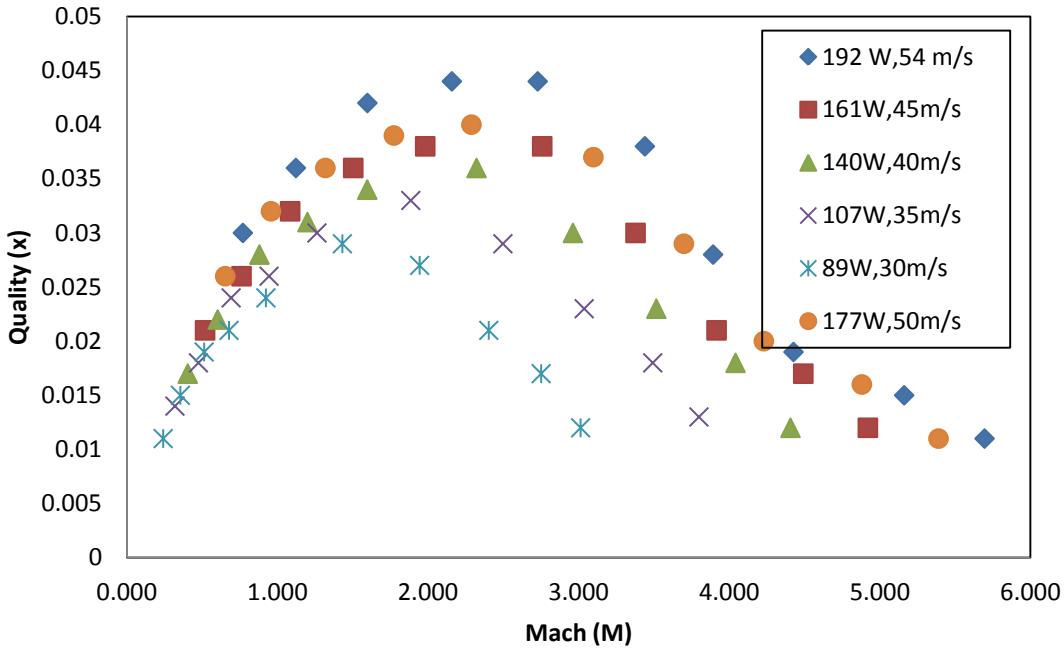

Figure 6.32 Flow quality (x) vs. Nusselt number ratios (Φ) of Test Section-4

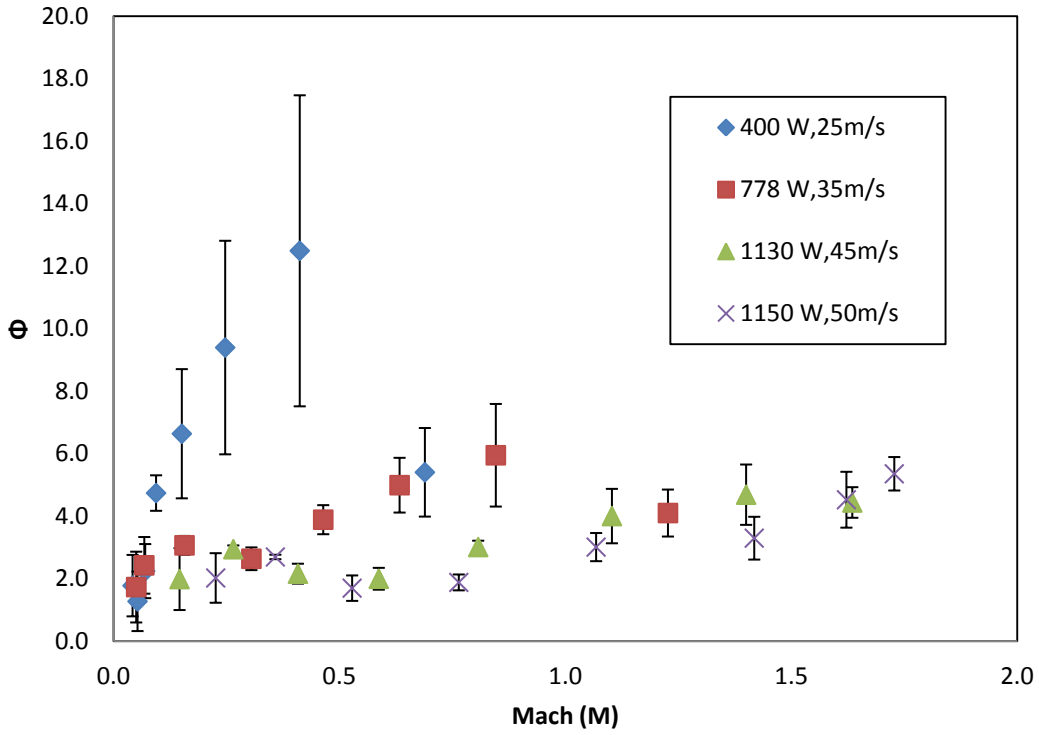

Figure 6.33 Nusselt number ratio (Φ) vs. Mach number (M) of Test Section-1

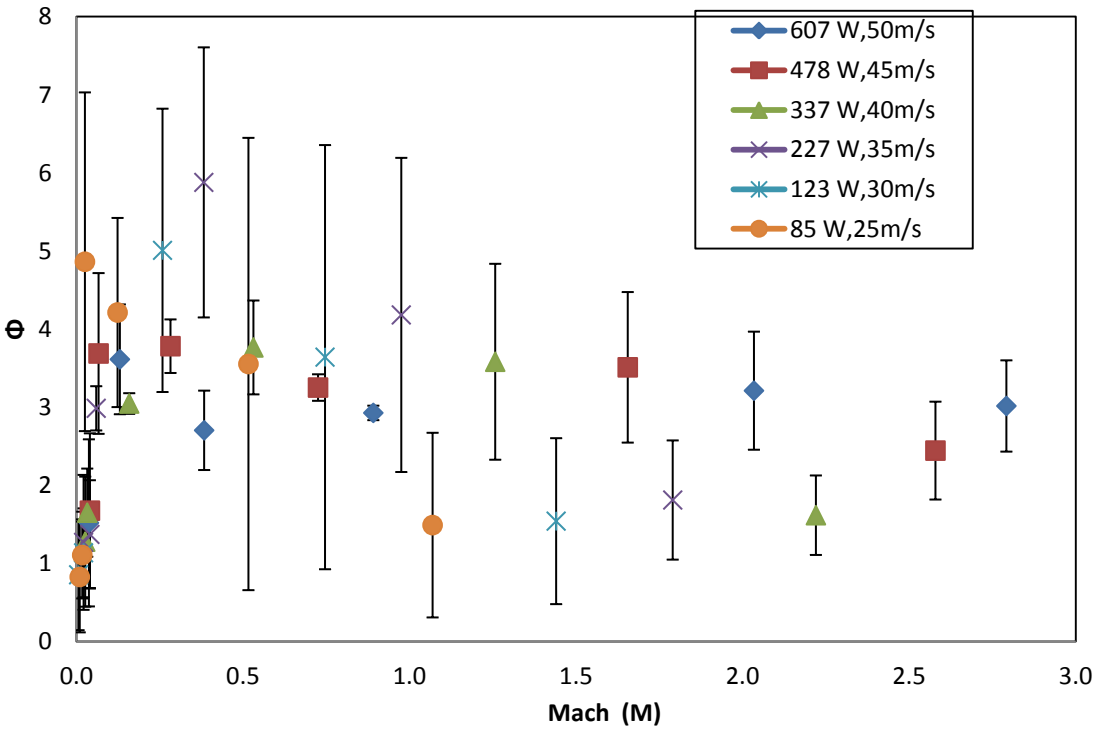

Figure 6.34 Nusselt number ratios vs. Mach number (M) of Test Section-2

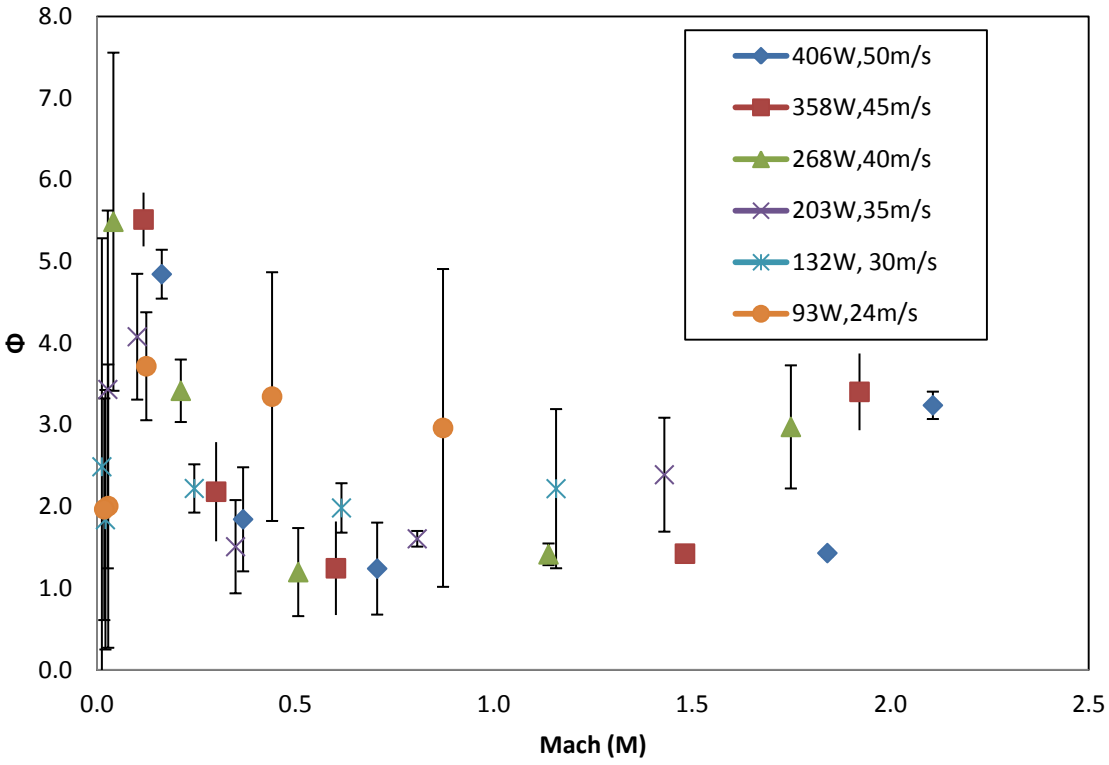

Figure 6.35 Nusselt number ratio (Φ) vs. Mach number (M) of Test Section-3

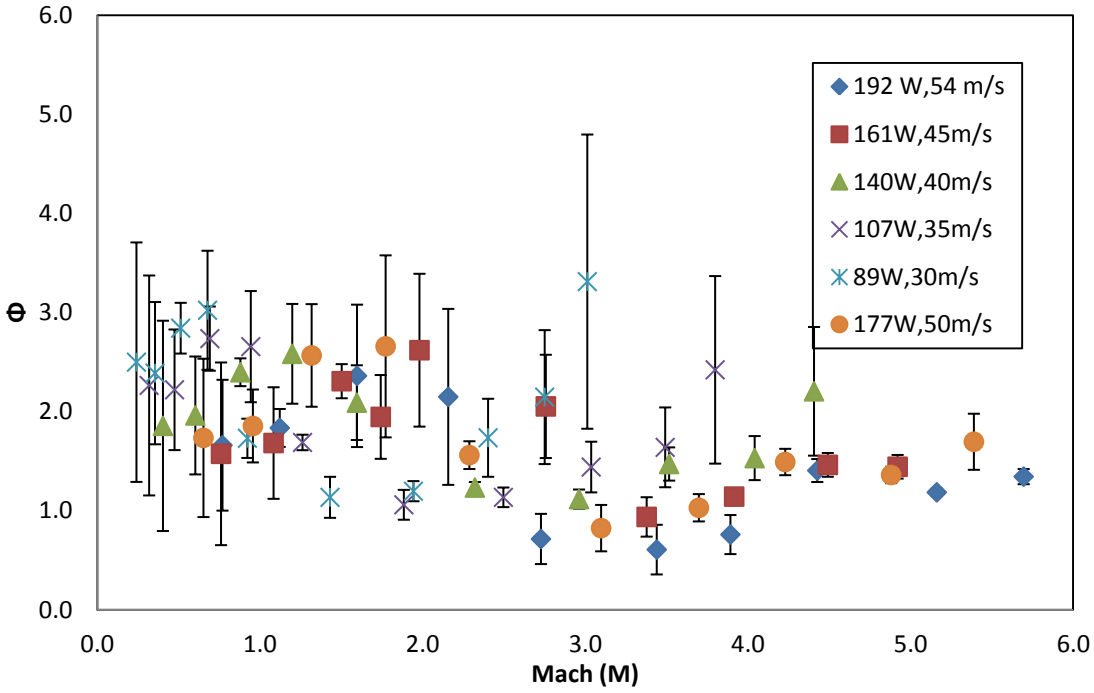

Figure 6.36 Nusselt number ratio vs. Mach number (M) of Test Section-4

6.8 Conclusion

This chapter presented the analytical results from testing four different nozzles: one with a 2.43mm throat and three 1.5 mm throat nozzles. Two different working fluids are presented: R134a and R123. The results of the each nozzle showed that the dominant parameter in the nozzle performance is the heat flux. Specifically heat transfer coefficients increase with increasing heat flux in the sonic multiphase region. In all the nozzles, sonic region (approx. 50 mm from throat) has very high heat transfer coefficients (>60000 W/m^2 K)) and low heat transfer coefficients (10000-20000 W/m^2 K) at the end of the nozzle.

This chapter also presented the results of Mach numbers and flow quality and Nusselt number values along the nozzle. Mach numbers above one in the nozzle are in sonic region and Mach numbers decreased along the nozzle, similarly quality also decreased along the nozzle. Maximum quality occurred at the lowest temperature position of the nozzle. Finally Nusselt number ratios were plotted against the Mach numbers showed that the Nusselt number ratios increased in the sonic region of the nozzle.

7 Conclusion

The current research addresses the experimental investigation of sonic multiphase flow in converging-diverging nozzles, which has potential applications in cooling devices, flow measuring devices. This study first address the sonic multiphase heat transfer coefficients and flow characteristics for different throat diameter nozzles, focused on two different throat diameters (2.43mm and 1.5 mm), two refrigerants (R123 and R134a) and all nozzles have 1 degree growth angle in the diverging portion with the center line of the nozzle. The test section, which is assembled from different length of diverging sections and length of the fluid passage depends on the number of sections attached together.

Refrigerant passage in the test section was instrumented with temperature sensors and pressure transducers for measuring the wall temperature and pressure of the each nozzle section. Each test section has fixtures for heater; the heaters are embedded in nozzle and do not have any contact with fluid. The voltage given to the heater was varied until the average temperature of the heater portion of the nozzle equals to the inlet temperature.

For four nozzle assemblies were tested, data was collected according to a test matrix based on the controlling variable: Inlet temperature and throat velocity. The range of the each variable was fixed for all the four nozzles to produce the data helpful for comparison among the four nozzle assemblies.

The data for R-134a showed that as the fluid flows through the diverging portion of the nozzle, the pressure of the liquid drops below inlet saturation pressure of the liquid due to sonic expansion in the nozzle. The temperature of the fluid dropped around 10 ^{o}C in heated cases and

15 °C in unheated cases at higher velocities. For R123 results, the temperature and saturation pressure drop in the nozzle was less than that for R134a.

Two phase heat transfer coefficients are strong functions of the heat fluxes and mass fluxes in the sonic nozzle. For R134a results, two-phase heat transfer coefficients are high around 10000 W/m^2 K in the first 50 mm of the nozzle and heat transfer coefficients decreased along the nozzle. For R123, two-phase heat transfer coefficients are less than R134a and around 60000 W/m^2 K in the first 50 mm of the nozzle. Comparison of the insulated and solid model heat fluxes and heat transfer coefficients showed that they are within approximately 20 % of each other at higher velocity (40 m/s to 50m/s) data points. The results showed that the two-phase heat transfer coefficients were not depending on the dimensions of the fluid passage.

Mach number and flow quality decreased along the length of the nozzle for both fluids. The Mach number profile appears similar to the temperature profile, and the fluid is in the sonic region as long as temperature of the fluid dropped in the nozzle. Mach numbers drop below one (subsonic) when the temperature starts rising in the nozzle. The length of the sonic region is larger for R123 than R134a and the Mach numbers are higher for R123.

For R134a results, the maximum Nusselt number ratio was achieved at the lowest temperature position in the nozzle. Nusselt number ratios were compared with the Mach numbers and showed that the Nusselt number ratio were increased in the sonic region. The Nusselt ratios of R123 were low compared to the R134a cases and the trend in the Nusselt ratios was different as well.

References or Bibliography

1) Ali, R., Palm, B., Maqbool, M.H., Flow Boiling Heat Transfer Characteristics of a Minichannel up to Dry out Condition, Journal of Heat Transfer, v 133, n 8, p 081501 (10 pp.), Aug. 2011.

2) Boivin, J.Y., Two-phase critical flow in long nozzles, Nuclear Technology, v 46, n 3, 540-5, Dec. 1979; ISSN: 0029-5450; Country of publication: USA.

3) Blythe, P.A., and Shih, C.J., condensation shocks J. Fluid Mech. 76, 593 (1976).

4) Brennen, C.E., Cavitation and bubble dynamics. Applied Mechanics Reviews, v 48, n 10, p B146, Oct 1995; ISSN: 00036900; Publisher: ASME.

5) Campbell I.J., Pitcher, A.S., Shock waves in a liquid Containing Gas bubbles. Proceedings of the Royal Society of London. Series A, Mathematical and Physical Sciences, Vol-243, No.1235, 1958, pp.534-545.

6) Carstensen, E.L., Foldy, L.L., Propagation of Sound through a liquid Containing Bubbles. The journal of the Acoustical Society of America, Vol-19, NO-3, pp 481-501, May, 1947.

7) Copetti, J.B., Macagnan, M.H., Zinani, F., Kunsler, N.L.F., Flow boiling heat transfer and pressure drop of R-134a in a mini tube: an experimental investigation. Experimental Thermal and Fluid Science vol. 35 issue 4 May, 2011. p. 636-644.

8) Cavallini, A., Bortolin, S., Del Col, D., Matkovic, M., Rossetti, L., Flow boiling inside a single circular mini channel: Measurement of local heat transfer coefficient, 2007 Proceedings of the ASME/JSME Thermal Engineering Summer Heat Transfer Conference - HT 2007, v 1, p 901-909, 2007.

9) Dean, E.A., Atmospheric Effects on the Speed of Sound, Technical report of Defense Technical Information Center, 1979.

10) Dittus , E.J., Boelter, L.M.K., Heat transfer in automobile radiators of tubular type, Univ. California Berkley, Publications on Engineering 2 (1930) 443- 461.

11) Delale, Can F., Okita, Kohei., Matsumoto, Yoichiro., Steady-state cavitating nozzle flows with nucleation, Journal of Fluids Engineering, Transactions of the ASME, v 127, n 4, p 770-777, July 2005.

12) Evans, G.R., Gouse, G.W., and Bergles, A.E., The pressure wave propagation in adiabatic Slug-annular-mist Two-phase gas-liquid flow. Journal of Chemical Engineering Science, Vol-25, Issue-4, pp 569-582.

13) Gouse, S.W., George, JR., Brown. A., A survey of the Velocity of sound in Two-phase Mixtures. ASME Paper 64-WA/FE-35, 1964.

14) Huo, X., Chen, L., Tian, Y.S., Karayiannis, T.G., Flow boiling and flow regimes in small diameter tubes, Applied Thermal Engineering, v 24, n 8-9, p 1225-1239, June 2004.

15) Henry, R. E., Pressure wave propagation in Two-phase mixtures. Journal of chemical Engineering progress symposium series,Vol-66,Issue-102,PP 1-10, 1970.

16) John C. DeVine III, Per F. Peterson, Transient Phenomena in Nuclear Reactor Systems. ASME, Heat Transfer Division, v 245, p 29-38, 1993.

17) Karplus, H.P. The velocity of sound in a liquid containing gas Bubbles.COO-248, Armor Research Foundation, 1958.

18) Kandlikar, Satish G., Heat transfer mechanisms during flow boiling in micro channels, Department of Mechanical Engineering, Rochester Institute of Technology, Rochester, NY Source: Journal of Heat Transfer, v 126, n 1, p 8-16, February 2004.

19) Mallock, A., The damping of Sound by Frothy Liquids. Proc. Roy. Soc. Series A, 84,PP 391-395,1910.

20) Michaelides, E. E., Velocity of Sound in Two-phase Mixtures. International Journal of Heat & Fluid Flow, Vol-4, No-2, pp 79-84, 1983.

21) Martindale, W.R., Smith, R.V., Separated Two-Phase Flow In A Nozzle, International Journal of Multiphase Flow, v 8, n 3, p 217-226, Jun 1982.

22) Murray, J.D., Note on the propagation of disturbances in a liquid Containing Gas bubbles. Appl. Sci. Res Section A, Vol-13,PP 281-290,1964.

23) NIST National Institute of Standard and Technology, REFPROP Version 7.0, Boulder Colorado, 2002.

24) Nusselt, W., Die Abhangigkeit der Wärmeubergangszhal von der Rohrlange, Zeiterschr. VDI, 54, 1154-1158, 1910.

25) Nguyen, D.L., Sonic velocity in Two-phase systems. International Journal of multiphase flow, Volume-7, Issue 3, PP 311-320, 1981.

26) Ozdemir, M.R., Kosar, A., Boiling heat transfer in micro tubes at high flow rates, 14th International Heat Transfer Conference, v 1, p 691-696, 2010.

27) Owhaib, W., Martín-Callizo, C., Palm, B., Evaporative heat transfer in vertical circular micro channels, Applied Thermal Engineering, v 24, n 8-9, p 1241-1253, June 2004.

28) Romstedt, P.; Werner, W., Numerical analysis of critical two-phase flow in a convergent-divergent nozzle, Nuclear Science and Engineering, v 92, n 1, 71-83, Jan. 1986; ISSN: 0029-5639; Country of publication: USA.

29) Rood, E.P., Review. Mechanisms of cavitation inception, Journal of Fluids Engineering, Transactions of the ASME, v 113, n 2, p 163-175, Jun 1991.

30) Saunders, P., Propagation of uncertainty for non-linear calibration equations with an application in radiation thermometry. Metrologia. Vol.40, pp.93-101,2003.

31) Schrock, V.E., Starkman, E.S., Brown, R.A., Flashing Flow Of Initially Subcooled Water In Convergent-Divergent Nozzles, American Society of Mechanical Engineers ,1976.

32) Tangren, R.F., Dodge, C.H., and Seifert, H.S., Compressibility effects in Two-phase flow. Journal of Applied Physics, Vol-20, No.7, pp 637-645, July, 1949.

33) Wood, A.B., A Text Book of Sound, G. Bill and Sons Ltd, London, 1941.

34) Yonechi, Hiroo., Suzuki, Maki., Ishii, Ryuji., Morioka, Shigeki., Bubbly flows through a convergent-divergent nozzle , Memoirs of the Faculty of Engineering, Kyoto University, v 54, n pt 2, p 83-104, Apr 1992.

35) Yu, W., France, D.M., Wambsganss, M.W., Hull, J.R., Two-phase pressure drop, boiling heat transfer, and critical heat flux to water in a small-diameter horizontal tube. International Journal of Multiphase Flow, v 28, n 6, p 927-941, June 2002.

Appendix A - Data tables

Test Section-1

	Nozzle section	T_{sat} (°C)	G ($kg/m^2 s$)	q_c (W/m^2)	h_l ($W/m^2 K$)	q_l (W/m^2)	h_c ($W/m^2 K$)	ϕ	M	x	α
400 W,25m/s	Throat	30.8	30262.1						0.03	0.00	0.00
	Div-1		23164.6	143867.7		240915.2					
	Div-2		16368.6	258423.2		206288.4					
	Div-3	22.0	11600.2	223208.9	63778.2	173546.1	82029.3	5.41	0.69	0.07	0.74
	Div-4	23.6	8802.6	213340.6	107040.5	148812.3	149325.0	12.50	0.41	0.05	0.65
	Div-5	26.6	7045.3	186904.2	65082.1	131478.8	92517.7	9.40	0.25	0.03	0.52
	Div-6	28.2	5583.9	159228.2	39534.4	117322.4	53655.5	6.64	0.15	0.02	0.40
	Div-7	29.5	4519.8	96748.8	34214.6	105029.1	31517.2	4.74	0.09	0.01	0.28
	Div-8	29.8	3556.1	63933.3	17656.7	93787.4	12036.2	2.24	0.07	0.01	0.26
	Div-9	30.0	2870.7	38574.0	12268.6	83756.6	5650.3	1.27	0.05	0.01	0.24
	Div-10	30.1	2365.9	42968.2	11668.7	75664.2	6626.4	1.78	0.04	0.01	0.23
	Div-11	30.1	1983.5						0.04	0.01	0.23
	Div-12	30.1	1686.8						0.03	0.01	0.18
	Div-13	30.2	1452.0						0.02	0.01	0.18

	Nozzle section	T_{sat} (°C)	G ($kg/m^2 s$)	q_c (W/m^2)	h_l ($W/m^2 K$)	q_l (W/m^2)	h_c ($W/m^2 K$)	ϕ	M	x	α
778 W,35m/s	Throat	30.6	41894.9			0.0			0.05	0.00	0.00
	Div-1		32069.2	214457.6		468580.1					
	Div-2		22660.7	364479.6		401231.0					
	Div-3	18.0	16059.4	394745.2	68538.6	337547.1	80152.7	4.10	1.23	0.09	0.82
	Div-4	19.5	12186.4	355601.5	74030.2	289439.9	90952.4	5.95	0.85	0.08	0.79
	Div-5	21.1	9753.6	299106.7	53855.1	255726.3	62990.9	4.99	0.63	0.07	0.77
	Div-6	21.9	7730.4	252769.3	35813.3	228192.0	39670.6	3.89	0.46	0.07	0.75
	Div-7	23.8	6257.2	181685.7	25188.5	204281.5	22402.4	2.64	0.31	0.05	0.67
	Div-8	26.6	4923.0	169615.4	22906.1	182416.4	21298.6	3.07	0.16	0.03	0.48
	Div-9	29.8	3974.2	114601.6	19879.4	162906.6	13984.8	2.43	0.07	0.01	0.21
	Div-10	30.5	3275.4	74864.8	16507.1	147166.9	8397.3	1.73	0.05	0.01	0.18
	Div-11	30.5	2745.9						0.04	0.01	0.17
	Div-12	30.6	2335.1			0.0			0.03	0.00	0.09
	Div-13	30.6	2010.1			0.0			0.02	0.00	0.09

	Nozzle section	T_{sat} (°C)	G ($kg/m^2 s$)	q_c (W/m^2)	h_l ($W/m^2 K$)	q_l (W/m^2)	h_c ($W/m^2 K$)	ϕ	M	x	α
1130 W,45m/s	Throat	30.8	54132.3			0.0				0.00	0.00
	Div-1		41436.5	352519.6		680585.4					
	Div-2		29279.8	513749.8		582764.8					
	Div-3	18.9	20750.3	543123.2	95572.8	490267.7	105876.5	4.44	1.64	0.09	0.82
	Div-4	16.5	15746.0	515283.1	71129.9	420394.8	87184.8	4.69	1.40	0.10	0.85
	Div-5	16.6	12602.6	461189.6	49336.8	371427.6	61259.9	4.00	1.10	0.10	0.85
	Div-6	17.8	9988.5	353127.3	35144.9	331435.6	37445.0	3.01	0.81	0.10	0.83
	Div-7	19.7	8084.9	249200.5	24489.5	296707.1	20568.4	2.00	0.59	0.09	0.81
	Div-8	21.3	6361.1	228731.4	20819.6	264949.3	17973.6	2.16	0.41	0.08	0.77
	Div-9	23.6	5135.0	228112.4	21140.0	236612.5	20380.5	2.94	0.27	0.06	0.70
	Div-10	26.6	4232.1	128510.3	19534.8	213751.3	11744.6	1.99	0.15	0.03	0.52
	Div-11	29.9	3548.0	154582.5	31453.2	194918.6			0.07	0.01	0.28
	Div-12	30.6	3017.2			0.0			0.05	0.01	0.18
	Div-13	30.8	2597.3			0.0			0.04	0.01	0.16

	Nozzle section	T_{sat} (°C)	G ($kg/m^2 s$)	q_c (W/m^2)	h_l ($W/m^2 K$)	q_l (W/m^2)	h_c ($W/m^2 K$)	ϕ	M	x	α
1150 W,50m/s	Throat	30.8	60085.4			0.0				0.00	0.00
	Div-1		45993.4	346758.1		692631.2					
	Div-2		32499.8	504700.2		593079.2					
	Div-3	19.4	23032.2	541601.8	128620.3	498945.0	139616.5	5.36	1.73	0.08	0.81
	Div-4	16.7	17477.7	519702.3	74768.7	427835.4	90823.4	4.53	1.62	0.11	0.86
	Div-5	14.3	13988.5	464891.9	44096.9	378001.6	54233.4	3.30	1.42	0.12	0.88
	Div-6	14.7	11086.9	391268.9	34626.4	337301.8	40166.6	3.01	1.07	0.12	0.87
	Div-7	17.0	8974.1	263954.3	23902.8	301958.5	20894.4	1.88	0.76	0.10	0.85
	Div-8	19.1	7060.6	211914.8	19433.4	269638.6	15273.1	1.70	0.53	0.09	0.82
	Div-9	21.5	5699.7	236252.2	20552.8	240800.3	20164.6	2.70	0.36	0.08	0.77
	Div-10	24.2	4697.5	146277.0	19154.5	217534.6	12880.1	2.02	0.23	0.05	0.67
	Div-11	27.6	3938.1	133647.2	29050.1	198368.5			0.12	0.03	0.47
	Div-12	30.3	3349.1		0.0	0.0			0.06	0.01	0.20
	Div-13	30.9	2882.9		0.0	0.0			0.04	0.01	0.17

Test Section-2

	Nozzle section	T_{sat} (°C)	G ($kg/m^2 s$)	q_c (W/m^2)	h_l ($W/m^2 K$)	q_l (W/m^2)	h_c ($W/m^2 K$)	Φ	M	x	α
607 W,50m/s	Throat	25.0	46796.2						0.47	0.00	0.07
	Div-1	10.7	32372.5	603240.0	94277.1	498800.0	114017.1	3.02	2.79	0.07	0.82
	Div-2	9.0	23718.7			421601.4			2.43	0.09	0.86
	Div-3	8.4	18253.4	462080.0	57010.5	365661.3	72043.2	3.21	2.03	0.10	0.88
	Div-4	9.7	12861.0			313248.3			1.42	0.11	0.88
	Div-5	12.3	9114.5	260162.0	36273.7	263356.2	35833.8	2.93	0.89	0.10	0.86
	Div-6	14.8	6765.2			224489.1			0.57	0.08	0.83
	Div-7	17.3	5535.6	165412.9	25591.8	199311.1	21239.2	2.70	0.38	0.07	0.77
	Div-8	20.2	4387.4			178036.7			0.23	0.05	0.68
	Div-9	22.9	3551.3	131463.6	23569.2	159381.6	19440.7	3.61	0.13	0.03	0.51
	Div-10	24.8	2794.1			142322.3			0.07	0.01	0.32
	Div-11	25.6	2255.5	60957.9	11438.9	127100.7	5486.1	1.52	0.04	0.01	0.18
	Div-12	25.5	1858.9			114820.4			0.03	0.01	0.18
	Div-13	25.4	1557.5		1266.9	10013.5			0.02	0.00	0.13
	Div-14	25.4	1323.8						0.02	0.00	0.11
	Div-15	25.5	1139.0						0.01	0.00	0.10

	Nozzle section	T_{sat} (°C)	G ($kg/m^2 s$)	q_c (W/m^2)	h_l ($W/m^2 K$)	q_l (W/m^2)	h_c ($W/m^2 K$)	ϕ	M	x	α
478 W,45m/s	Throat	25.1	41574.4						0.39	0.00	0.07
	Div-1	10.6	28760.2	507000.0	65074.9	392794.8	83995.5	2.45	2.58	0.07	0.83
	Div-2	10.3	21072.0			332002.4			2.07	0.09	0.85
	Div-3	10.5	16216.5	378400.0	54765.9	287950.8	71968.7	3.51	1.66	0.09	0.86
	Div-4	11.6	11425.9			246676.5			1.14	0.10	0.86
	Div-5	13.7	8097.4	215463.7	34829.2	207387.6	36185.6	3.25	0.73	0.09	0.84
	Div-6	16.3	6010.3			176780.5			0.45	0.07	0.80
	Div-7	19.3	4917.9	144694.4	29780.1	156953.4	27454.1	3.78	0.28	0.05	0.71
	Div-8	22.6	3897.8			140200.2			0.15	0.03	0.53
	Div-9	24.9	3155.0	95065.2	23924.8	125509.7	18121.4	3.69	0.07	0.01	0.26
	Div-10	25.4	2482.3			112075.9			0.04	0.01	0.19
	Div-11	25.1	2003.9	54462.8	10073.6	100089.2	5481.5	1.68	0.04	0.01	0.24
	Div-12	25.1	1651.5			90418.7			0.03	0.01	0.23
	Div-13	25.3	1383.7		1123.2	7885.5			0.02	0.00	0.14
	Div-14	25.3	1176.1						0.02	0.00	0.13
	Div-15	25.2	1011.9						0.01	0.00	0.14

	Nozzle section	T_{sat} (°C)	G ($kg/m^2 s$)	q_c (W/m^2)	h_l ($W/m^2 K$)	q_l (W/m^2)	h_c ($W/m^2 K$)	Φ	M	x	α
337 W,40m/s	Throat	25.0	36494.5						0.32	0.00	0.06
	Div-1	11.5	25246.0	379560.0	44256.0	276928.5	60657.6	1.62	2.22	0.08	0.83
	Div-2	12.3	18497.3			234068.7			1.65	0.08	0.84
	Div-3	13.1	14235.1	287800.0	53691.3	203011.3	76115.7	3.58	1.26	0.08	0.84
	Div-4	14.0	10029.8			173912.1			0.86	0.08	0.83
	Div-5	16.1	7108.0	169793.1	38904.0	146212.6	45178.2	3.77	0.53	0.07	0.80
	Div-6	19.6	5275.9			124634.0			0.29	0.05	0.69
	Div-7	22.5	4317.0	111934.5	21828.5	110655.4	22080.9	3.05	0.16	0.03	0.51
	Div-8	24.5	3421.6			98844.1			0.08	0.01	0.29
	Div-9	25.4	2769.5	62719.3	11506.5	88487.0	8155.7	1.65	0.03	0.00	0.10
	Div-10	25.5	2179.0			79015.8			0.03	0.00	0.10
	Div-11	25.3	1759.0	35936.9	8249.8	70565.0	4201.4	1.28	0.03	0.00	0.15
	Div-12	25.3	1449.7			63747.1			0.02	0.00	0.14
	Div-13	25.4	1214.6		902.0	5559.4			0.01	0.00	0.06
	Div-14	25.4	1032.4						0.01	0.00	0.04
	Div-15	25.4	888.3						0.01	0.00	0.05

	Nozzle section	T_{sat} (°C)	G ($kg/m^2 s$)	q_c (W/m^2)	h_l ($W/m^2 K$)	q_l (W/m^2)	h_c ($W/m^2 K$)	Φ	M	x	α
227 W,35m/s	Throat	25.1	31795.9			0.0			0.25	0.00	0.05
	Div-1	13.3	21995.6	285500.0	33170.0	186536.4	50767.7	1.81	1.79	0.07	0.81
	Div-2	14.2	16115.7			157666.4			1.30	0.08	0.81
	Div-3	15.0	12402.3	222200.0	43106.8	136746.5	70044.5	4.18	0.98	0.07	0.81
	Div-4	15.8	8738.5			117145.6			0.66	0.07	0.80
	Div-5	18.3	6192.9	130682.1	40313.1	98487.4	53491.2	5.88	0.38	0.06	0.74
	Div-6	22.4	4596.6			83952.3			0.17	0.03	0.51
	Div-7	25.0	3761.2	68958.4	19094.3	74536.4	17665.3	2.99	0.06	0.01	0.17
	Div-8	25.3	2981.0			66580.4			0.04	0.00	0.10
	Div-9	25.0	2412.9	35607.7	9112.1	59604.0	5443.6	1.37	0.04	0.01	0.18
	Div-10	25.0	1898.4			53224.3			0.03	0.01	0.18
	Div-11	25.2	1532.5	23431.5	6807.3	47531.9	3355.8	1.27	0.02	0.00	0.14
	Div-12	25.2	1263.1			42939.4			0.02	0.00	0.14
	Div-13	25.2	1058.2		732.6	3744.8			0.01	0.00	0.09
	Div-14	25.2	899.5						0.01	0.00	0.08
	Div-15	25.2	773.9						0.01	0.00	0.08

	Nozzle section	T_{sat} (°C)	G ($kg/m^2 s$)	q_c (W/m^2)	h_l ($W/m^2 K$)	q_l (W/m^2)	h_c ($W/m^2 K$)	Φ	M	x	α
123 W,30m/s	Throat	25.0	27478.7						0.19	0.00	0.04
	Div-1	14.7	19009.1	207000.0	72784.6	387740.0	38857.0	1.54	1.44	0.07	0.79
	Div-2	15.6	13927.6						1.02	0.07	0.79
	Div-3	16.5	10718.4	161530.0	75548.8	222100.0	54945.5	3.64	0.75	0.06	0.77
	Div-4	17.8	7552.0						0.48	0.06	0.74
	Div-5	20.4	5352.0	75495.2	49500.7	91693.6	40756.0	5.01	0.26	0.04	0.64
	Div-6	23.7	3972.5						0.10	0.01	0.35
	Div-7	25.5	3250.5	29670.6	9820.7	32983.8	8834.2	1.67		0.00	0.30
	Div-8	25.6	2576.3							0.00	0.10
	Div-9	25.1	2085.3	19411.1	4397.5	21244.0	4018.1	1.14	0.02	0.00	0.07
	Div-10	25.2	1640.7						0.02	0.00	0.07
	Div-11	25.4	1324.5	10671.6	1630.0	8636.0	2014.2	0.86	0.01	0.00	0.02
	Div-12	25.4	1091.6						0.00	0.00	0.01
	Div-13	25.4	914.5		4062.2	16546.3				0.00	-0.02
	Div-14	25.4	777.3							0.00	-0.03
	Div-15	25.4	668.8							0.00	-0.03

	Nozzle section	T_{sat} (°C)	G ($kg/m^2 s$)	q_c (W/m^2)	h_l ($W/m^2 K$)	q_l (W/m^2)	h_c ($W/m^2 K$)	ϕ	M	x	α
85 W,25m/s	Throat	25.0	22773.3			0.0			0.14	0.00	0.03
	Div-1	16.5	15754.0	161340.0	14031.2	69848.4	32410.1	1.49	1.07	0.06	0.76
	Div-2	17.3	11542.7			59038.1			0.75	0.06	0.75
	Div-3	18.6	8883.0	121000.0	19618.2	51204.6	46359.0	3.55	0.52	0.05	0.71
	Div-4	20.8	6258.8			43865.1			0.28	0.04	0.61
	Div-5	23.4	4435.5	47644.5	23122.8	36878.5	29873.1	4.21	0.12	0.02	0.38
	Div-6	24.7	3292.3			31435.9			0.05	0.00	0.16
	Div-7	25.1	2693.9	19137.4	9667.9	27910.1	22044.9	4.86	0.03	0.00	0.07
	Div-8	25.1	2135.1			24931.0			0.02	0.00	0.06
	Div-9	25.1	1728.2	13412.1	5604.3	22318.7	3367.8	1.11	0.02	0.00	0.07
	Div-10	25.1	1359.7			19929.8			0.01	0.00	0.07
	Div-11	25.2	1097.7	7131.5	4175.8	17798.3	1673.2	0.83	0.01	0.00	0.06
	Div-12	25.2	904.6			16078.6			0.01	0.00	0.06
	Div-13	25.2	757.9		429.7	1402.2			0.00	0.00	0.02
	Div-14	25.2	644.2						0.00	0.00	0.02
	Div-15	25.2	554.3						0.00	0.00	0.02

Test Section-3

	Nozzle section	T_{sat} (°C)	G ($kg/m^2 s$)	q_c (W/m^2)	h_l ($W/m^2 K$)	q_l (W/m^2)	h_c ($W/m^2 K$)	Φ	M	x	α
406W,50m/s	Throat	25.0	46796.2			0.0			0.47	0.00	0.07
	Div-1	15.8	32372.5	543250.0	122429.9	533806.4	124595.9	3.24	2.11	0.05	0.74
	Div-2	11.9	23718.7			451189.9			2.09	0.08	0.83
	Div-3	10.4	18253.4	382700.0	32928.3	391323.9	32202.6	1.43	1.84	0.09	0.86
	Div-4	12.3	12861.0			335232.4			1.23	0.09	0.85
	Div-5	15.8	9114.5	177555.5	24198.6	281838.8	15244.8	1.24	0.71	0.08	0.81
	Div-6	17.2	6765.2			240244.0			0.48	0.07	0.78
	Div-7	17.9	5535.6	150525.0	20600.0	213299.0	14537.4	1.84	0.37	0.06	0.76
	Div-8	19.3	4387.4			190531.5			0.26	0.05	0.72
	Div-9	21.4	3551.3	128785.5	24923.5	123187.4	26056.1	4.84	0.16	0.04	0.62
	Div-10	24.1	2794.1						0.07	0.02	0.36
	Div-11	25.8	2255.5	22942.6			13815.0	3.82	0.02	0.00	0.03
	Div-12	25.8	1858.9						0.01	0.00	0.04
	Div-13	25.5	1557.5	3402.4			4183.0	1.62	0.02	0.00	0.12
	Div-14	25.5	1323.8						0.02	0.00	0.11
	Div-15	25.6	1139.0	380.8			776.6	0.40	0.01	0.00	0.09

	Nozzle section	T_{sat} (°C)	G ($kg/m^2 s$)	q_c (W/m^2)	h_l ($W/m^2 K$)	q_l (W/m^2)	h_c ($W/m^2 K$)	Φ	M	x	α
358W,45m/s	Throat	25.3	42542.0			0.0			0.38	0.00	0.06
	Div-1	16.2	29429.5	535800.0	106927.4	470696.3	121717.0	3.40	1.92	0.06	0.75
	Div-2	13.8	21562.4			397847.3			1.75	0.07	0.81
	Div-3	12.9	16594.0	320140.0	32267.4	345059.0	29937.1	1.42	1.48	0.08	0.84
	Div-4	14.3	11691.8			295599.0			1.00	0.08	0.83
	Div-5	16.8	8285.9	155578.5	22816.1	248518.0	14283.4	1.24	0.60	0.07	0.79
	Div-6	18.0	6150.2			211840.8			0.41	0.06	0.76
	Div-7	19.2	5032.4	142280.7	21287.5	188081.4	16103.7	2.18	0.30	0.06	0.73
	Div-8	21.0	3988.5			168005.6			0.20	0.04	0.65
	Div-9	23.1	3228.4	106128.0	28160.0	108623.4	27513.1	5.51	0.12	0.03	0.51
	Div-10	24.7	2540.1						0.06	0.01	0.29
	Div-11	25.5	2050.5	23545.4			13032.3	3.90	0.03	0.00	0.13
	Div-12	25.6	1689.9						0.02	0.00	0.13
	Div-13	25.4	1415.9	3282.1			3474.6	1.45	0.02	0.01	0.16
	Div-14	25.4	1203.5						0.02	0.01	0.16
	Div-15	25.4	1035.5	756.0			1195.8	0.66	0.02	0.00	0.15

	Nozzle section	T_{sat} (°C)	G ($kg/m^2 s$)	q_c (W/m^2)	h_l ($W/m^2 K$)	q_l (W/m^2)	h_c ($W/m^2 K$)	Φ	M	x	α
268W,40m/s	Throat	24.8	38287.8			0.0			0.31	0.00	0.05
	Div-1	15.9	26486.6	452700.0	75941.9	352364.8	97566.2	2.97	1.75	0.06	0.75
	Div-2	15.3	19406.2			297829.8			1.42	0.07	0.78
	Div-3	15.2	14934.6	235910.0	30145.6	258312.3	27531.2	1.41	1.14	0.07	0.80
	Div-4	15.8	10522.6			221286.4			0.79	0.07	0.79
	Div-5	17.2	7457.3	117708.6	20028.6	186041.4	12672.1	1.20	0.51	0.06	0.77
	Div-6	18.8	5535.2			158584.7			0.33	0.05	0.72
	Div-7	20.8	4529.1	126756.4	25804.7	140798.4	23231.2	3.42	0.21	0.04	0.62
	Div-8	23.3	3589.7			125769.6			0.11	0.02	0.43
	Div-9	25.1	2905.6	56214.8	20486.0	81315.8	25270.5	5.49	0.04	0.00	0.14
	Div-10	25.3	2286.1						0.01	0.00	0.02
	Div-11	25.0	1845.4	24499.6			15897.5	5.19	0.02	0.00	0.10
	Div-12	25.1	1520.9						0.02	0.00	0.08
	Div-13	25.2	1274.3	3037.2			4432.7	2.02	0.01	0.00	0.05
	Div-14	25.2	1083.1						0.01	0.00	0.06
	Div-15	25.2	931.9	865.5			2208.2	1.33	0.01	0.00	0.06

	Nozzle section	T_{sat} (°C)	G ($kg/m^2 s$)	q_c (W/m^2)	h_l ($W/m^2 K$)	q_l (W/m^2)	h_c ($W/m^2 K$)	Φ	M	x	α
203W,35m/s	Throat	25.0	29779.4			0.0			0.26	0.00	0.05
	Div-1	15.9	20600.7	357230.0	47867.6	266903.2	64067.3	2.39	1.43	0.06	0.77
	Div-2	16.3	15093.7			225595.0			1.06	0.06	0.77
	Div-3	16.6	11615.8	185770.0	27219.3	195661.9	25843.2	1.60	0.81	0.06	0.77
	Div-4	17.1	8184.3			167616.2			0.56	0.06	0.77
	Div-5	18.6	5800.1	96161.6	19121.1	140919.4	13048.0	1.51	0.35	0.05	0.73
	Div-6	21.3	4305.1			120122.0			0.19	0.03	0.60
	Div-7	23.5	3522.7	97352.0	39410.2	106649.5	22903.7	4.08	0.10	0.02	0.40
	Div-8	24.7	2792.0			95265.7			0.05	0.01	0.23
	Div-9	25.2	2259.9	32007.3	24917.5	61593.7	12948.5	3.43	0.03	0.00	0.11
	Div-10	25.3	1778.0						0.01	0.00	0.04
	Div-11	25.2	1435.3	23515.6					0.01	0.00	0.05
	Div-12	25.2	1183.0						0.01	0.00	0.04
	Div-13	25.3	991.1	2930.2					0.01	0.00	0.03
	Div-14	25.3	842.4						0.01	0.00	0.04
	Div-15	25.2	724.8	1275.6					0.01	0.00	0.04

	Nozzle section	T_{sat} (°C)	G (kg/m^2 s)	q_c (W/m^2)	h_l (W/m^2 K)	q_l (W/m^2)	h_c (W/m^2 K)	Φ	M	x	α
132W, 30m/s	Throat	25.0	25525.2			0.0			0.19	0.00	0.04
	Div-1	16.8	17657.7	270680.0	33961.4	173552.8	52967.6	2.22	1.16	0.06	0.75
	Div-2	17.4	12937.5			146692.3			0.83	0.06	0.74
	Div-3	17.9	9956.4	147440.0	24325.4	127228.5	28189.7	1.98	0.62	0.06	0.73
	Div-4	18.5	7015.1			108991.8			0.42	0.05	0.72
	Div-5	20.3	4971.5	80818.5	19297.6	91632.3	17020.2	2.22	0.25	0.04	0.65
	Div-6	23.5	3690.1			78108.9			0.10	0.02	0.39
	Div-7	25.4	3019.4	45009.9	19078.0	69348.4	12382.4	2.49	0.01	0.00	0.01
	Div-8	25.5	2393.1			61946.2					0.04
	Div-9	25.1	1937.1	15953.9	15372.4	40051.1	6123.4	1.84	0.02	0.00	0.09
	Div-10	25.2	1524.0						0.01	0.00	0.03
	Div-11	25.4	1230.3								0.01
	Div-12	25.4	1014.0								0.01
	Div-13	25.3	849.5								0.01
	Div-14	25.3	722.1								0.01
	Div-15	25.3	621.3								0.01

	Nozzle section	T_{sat}	G	q_c	h_l	q_l	h_c	ϕ	M	x	α
93W,24m/s	Throat	25.2	21271.0			0.0			0.14	0.00	0.03
	Div-1	18.2	14714.8	241300.0	30971.6	122275.9	61119.7	2.96	0.87	0.05	0.72
	Div-2	18.7	10781.2			103351.4			0.62	0.05	0.71
	Div-3	19.6	8297.0	141830.0	26015.6	89638.2	41163.2	3.35	0.44	0.05	0.68
	Div-4	21.2	5845.9			76789.7			0.26	0.03	0.60
	Div-5	23.3	4142.9	55540.7	28987.3	64559.1	24938.0	3.72	0.12	0.02	0.42
	Div-6	24.7	3075.1			55031.3			0.06	0.01	0.21
	Div-7	25.2	2516.2	19471.0	21613.2	48859.1	8613.2	2.00	0.03	0.00	0.09
	Div-8	25.3	1994.3			43643.9			0.02	0.00	0.08
	Div-9	25.2	1614.2	13827.2	11564.2	28217.8	5666.6	1.97	0.02	0.00	0.09
	Div-10	25.2	1270.0						0.01	0.00	0.05
	Div-11	25.3	1025.2						0.01	0.00	0.03
	Div-12	25.3	845.0						0.00	0.00	0.02
	Div-13	25.3	707.9						0.00	0.00	0.02
	Div-14	25.3	601.7						0.00	0.00	0.03
	Div-15	25.3	517.7						0.00	0.00	0.03

Test Section-4

	Nozzle section	T_{sat}	G	q_c	h_l	q_l	h_c	ϕ	M	x	α
192 W,54 m/s	Throat	30.2	59623.4						2.19	0.00	0.19
	Div-1	24.7	41246.1	164820.0	38150.0	157775.3	39853.4	1.34	5.70	0.01	0.73
	Div-2	24.0	30220.1	132000.0	27060.3	133356.6	26785.0	1.18	5.16	0.02	0.80
	Div-3	24.1	23256.8	124900.0	23252.6	115662.2	25109.7	1.40	4.43	0.02	0.84
	Div-4	22.8	16386.3	78571.6	12370.9	99083.5	9809.9	0.76	3.89	0.03	0.88
	Div-5	21.1	11612.8	54785.3	8650.5	83302.1	5689.2	0.61	3.44	0.04	0.92
	Div-6	21.3	8619.6	49616.1	7340.2	71008.1	5128.9	0.71	2.73	0.04	0.93
	Div-7	22.4	7053.0	95849.7	8532.8	63044.0	12973.0	2.15	2.16	0.04	0.93
	Div-8	23.7	5590.0	76467.0	8587.2	56314.7	11660.2	2.36	1.60	0.04	0.92
	Div-9	25.3	4524.7	45555.3	8275.0	50413.9	7477.5	1.83	1.12	0.04	0.90
	Div-10	26.7	3559.9	30118.4	8220.1	45017.9	5499.5	1.66	0.77	0.03	0.88
	Div-11			19504.2	6333.6	40203.2	3072.7				
	Div-12			30880.5	8962.3	36318.8	7620.3				

	Nozzle section	T_{sat} (°C)	G ($kg/m^2 s$)	q_c (W/m^2)	h_l ($W/m^2 K$)	q_l (W/m^2)	h_c ($W/m^2 K$)	ϕ	M	x	α
177W,50m/s	Throat	29.9	54625.6						2.02	0.00	0.19
	Div-1	24.5	37788.7	170130.0	40032.7	145449.1	46825.8	1.70	5.39	0.01	0.74
	Div-2	23.7	27687.0	127670.0	27560.7	122938.1	28621.5	1.36	4.88	0.02	0.81
	Div-3	23.6	21307.3	115140.0	22937.0	106626.1	24768.4	1.49	4.23	0.02	0.85
	Div-4	22.4	15012.8	80201.7	14089.8	91342.6	12371.3	1.03	3.70	0.03	0.89
	Div-5	21.5	10639.4	57747.6	9598.6	76794.1	7217.9	0.82	3.10	0.04	0.92
	Div-6	22.5	7897.1	71208.2	9680.5	65460.6	10530.5	1.56	2.29	0.04	0.92
	Div-7	23.5	6461.8	82216.2	10660.2	58118.7	15080.1	2.66	1.77	0.04	0.91
	Div-8	24.5	5121.4	63312.0	9746.8	51915.1	11886.5	2.57	1.32	0.04	0.91
	Div-9	25.6	4145.4	38240.2	8580.1	46475.4	7059.7	1.85	0.96	0.03	0.89
	Div-10	26.8	3261.5	26015.5	8554.4	41500.9	5362.4	1.73	0.65	0.03	0.86
	Div-11	26.5	2632.9	17475.3	6816.7	37062.3	3214.1				
	Div-12	27.5	2169.9	28082.2	10043.0	33481.4	8423.5				

	Nozzle section	T_{sat} (°C)	G ($kg/m^2 s$)	q_c (W/m^2)	h_l ($W/m^2 K$)	q_l (W/m^2)	h_c ($W/m^2 K$)	ϕ	M	x	α
161W,45m/s	Throat	29.9	49343.2						1.74	0.00	0.17
	Div-1	24.9	34134.4	163730.0	40137.5	132301.2	49672.4	1.95	4.92	0.01	0.75
	Div-2	24.0	25009.6	120520.0	26010.5	111825.1	28032.9	1.44	4.49	0.02	0.82
	Div-3	23.7	19246.9	104600.0	20771.2	96987.6	22401.5	1.46	3.92	0.02	0.85
	Div-4	22.6	13561.0	79347.9	13265.0	83085.6	12668.3	1.14	3.38	0.03	0.89
	Div-5	21.9	9610.5	56498.6	9385.5	69852.3	7591.2	0.94	2.76	0.04	0.92
	Div-6	23.1	7133.4	76761.7	9944.1	59543.2	12819.7	2.05	1.98	0.04	0.91
	Div-7	24.2	5836.9	71009.5	10244.6	52865.1	13760.7	2.62	1.50	0.04	0.91
	Div-8	25.3	4626.2	50588.0	9120.5	47222.2	9770.5	2.31	1.08	0.03	0.89
	Div-9	26.5	3744.6	30198.4	8313.3	42274.2	5938.6	1.68	0.76	0.03	0.86
	Div-10	27.5	2946.1	20671.3	8227.4	37749.4	4505.3	1.57	0.52	0.02	0.83
	Div-11	26.4	2378.3	15153.5	5847.8	33712.0	2628.6				
	Div-12	27.3	1960.1	24314.0	8258.9	30454.8	6593.6				

	Nozzle section	T_{sat} (°C)	G ($kg/m^2 s$)	q_c (W/m^2)	h_l ($W/m^2 K$)	q_l (W/m^2)	h_c ($W/m^2 K$)	ϕ	M	x	α
140W,40m/s	Throat	30.2	43950.5						1.47	0.00	0.16
	Div-1	25.5	30403.9	153410.0	38627.0	115044.5	51508.4	2.20	4.41	0.01	0.76
	Div-2	24.5	22276.3	111400.0	23738.9	97239.2	27196.0	1.53	4.04	0.02	0.82
	Div-3	24.2	17143.4	93586.0	18569.3	84337.0	20605.8	1.47	3.52	0.02	0.86
	Div-4	23.3	12078.9	66788.8	12272.1	72248.4	11344.8	1.12	2.96	0.03	0.89
	Div-5	23.0	8560.2	58910.9	9463.3	60741.1	9178.1	1.23	2.32	0.04	0.91
	Div-6	24.4	6353.8	61748.2	10066.2	51776.7	12004.8	2.09	1.60	0.03	0.90
	Div-7	25.4	5199.0	55577.2	10174.7	45969.6	12301.2	2.58	1.20	0.03	0.89
	Div-8	26.2	4120.6	42558.0	8980.1	41062.8	9307.1	2.40	0.88	0.03	0.87
	Div-9	27.3	3335.3	27187.0	8576.7	36760.2	6343.1	1.96	0.60	0.02	0.84
	Div-10	28.3	2624.2	18279.9	8739.5	32825.6	4866.8	1.86	0.40	0.02	0.79
	Div-11	26.8	2118.4	13848.1	5628.0	29314.8	2658.6				
	Div-12	27.7	1745.9	20255.8	7694.6	26482.5	5885.4				

	Nozzle section	T_{sat} (°C)	G ($kg/m^2 s$)	q_c (W/m^2)	h_l ($W/m^2 K$)	q_l (W/m^2)	h_c ($W/m^2 K$)	ϕ	M	x	α
107W,35m/s	Throat	29.8	38081.0						1.23	0.00	0.15
	Div-1	25.8	26343.5	129460.0	34311.4	87926.9	50518.7	2.42	3.80	0.01	0.75
	Div-2	24.7	19301.4	94486.0	20189.9	74318.5	25668.7	1.64	3.49	0.02	0.82
	Div-3	24.3	14853.9	76475.0	15175.9	64457.6	18005.2	1.44	3.04	0.02	0.86
	Div-4	23.6	10465.8	50606.4	11243.1	55218.4	10304.1	1.13	2.50	0.03	0.89
	Div-5	23.7	7417.0	40454.8	8098.6	46423.6	7057.4	1.06	1.89	0.03	0.90
	Div-6	25.0	5505.3	39392.1	8603.8	39572.2	8564.7	1.69	1.26	0.03	0.89
	Div-7	25.8	4504.7	43108.4	9214.3	35133.9	11305.7	2.66	0.94	0.03	0.87
	Div-8	26.4	3570.3	34806.0	8556.6	31383.7	9489.6	2.74	0.69	0.02	0.85
	Div-9	27.4	2889.9	21480.7	8377.7	28095.3	6405.3	2.22	0.48	0.02	0.81
	Div-10	28.2	2273.7	15296.3	8675.2	25088.1	5289.3	2.26	0.32	0.01	0.76
	Div-11	27.4	1835.5	11082.3	6006.2	22404.9	2970.9				
	Div-12	28.2	1512.7	13984.9	8530.4	20240.2	5894.1				

	Nozzle section	T_{sat} (°C)	G ($kg/m^2 s$)	q_c (W/m^2)	h_l ($W/m^2 K$)	q_l (W/m^2)	h_c ($W/m^2 K$)	ϕ	M	x	α
89W,30m/s	Throat	30.3	32602.3						0.95	0.00	0.13
	Div-1	27.2	22553.5	113600.0	39657.7	73135.4	61599.7	3.31	3.01	0.01	0.73
	Div-2	26.3	16524.5	84133.0	22036.2	61816.4	29991.6	2.15	2.75	0.02	0.81
	Div-3	25.8	12716.9	66772.0	15333.7	53614.3	19096.8	1.74	2.40	0.02	0.84
	Div-4	25.2	8960.1	42692.5	10293.9	45929.3	9568.4	1.20	1.94	0.03	0.87
	Div-5	25.3	6349.9	32326.9	7953.8	38614.0	6658.8	1.13	1.43	0.03	0.88
	Div-6	26.6	4713.2	29783.8	8654.1	32915.2	7830.8	1.73	0.92	0.02	0.86
	Div-7	27.3	3856.6	35228.8	9520.0	29223.5	11476.2	3.02	0.68	0.02	0.83
	Div-8	27.6	3056.6	27725.0	8256.9	26104.2	8769.5	2.84	0.51	0.02	0.82
	Div-9	28.4	2474.1	17422.7	8104.6	23369.0	6042.4	2.39	0.36	0.02	0.77
	Div-10	29.0	1946.6	12839.5	8314.0	20867.7	5115.4	2.50	0.24	0.01	0.72
	Div-11	27.9	1571.4	8355.6	5178.9	18635.8	2322.0				
	Div-12	28.7	1295.1	9837.3	6899.4	16835.3	4031.5				